



INVITED FEATURE ARTICLE

Antiferroelectrics: History, fundamentals, crystal chemistry, crystal structures, size effects, and applications

Clive A. Randall¹  | Zhongming Fan¹ | Ian Reaney² | Long-Qing Chen¹ | Susan Trolier-McKinstry¹ 

¹Materials Research Institute and Material Science and Engineering, The Pennsylvania State University, University Park, PA, USA

²University of Sheffield, Sheffield, UK

Correspondence

Clive A. Randall, Materials Research Institute and Material Science and Engineering, The Pennsylvania State University, University Park, PA, USA.
Email: car4@psu.edu

Funding information

National Science Foundation, Grant/Award Number: IIP-1841453 and 1841466

Abstract

Antiferroelectric (AFE) materials are of great interest owing to their scientific richness and their utility in high-energy density capacitors. Here, the history of AFEs is reviewed, and the characteristics of antiferroelectricity and the phase transition of an AFE material are described. AFEs are energetically close to ferroelectric (FE) phases, and thus both the electric field strength and applied stress (pressure) influence the nature of the transition. With the comparable energetics between the AFE and FE phases, there can be a competition and frustration of these phases, and either incommensurate and/or a glassy (relaxor) structures may be observed. The phase transition in AFEs can also be influenced by the crystal/grain size, particularly at nanometric dimensions, and may be tuned through the formation of solid solutions. There have been extensive studies on the perovskite family of AFE materials, but many other crystal structures host AFE behavior, such as $\text{CuBiP}_2\text{Se}_6$. AFE applications include DC-link capacitors for power electronics, defibrillator capacitors, pulse power devices, and electromechanical actuators. The paper concludes with a perspective on the future needs and opportunities with respect to discovery, science, and applications of AFE.

KEYWORDS

applications, dielectric materials/properties, ferroelectricity/ferroelectric materials, phase transition

1 | INTRODUCTION OF THE AFE

Antiferroelectric (AFE) materials have identifiable spontaneously ordered dipole moments that are arranged antiparallel so as to cancel out on a unit-cell basis at zero field, but for which an electric field of sufficient magnitude can induce a phase transition to a ferroelectric (FE) phase with parallel dipole ordering, as illustrated in Figure 1A. The AFE phase is typically a consequence of a structural phase transition from a higher temperature phase known as the prototype and/or paraelectric (PE) phase.^{1–23} It takes place through either a displacive soft-mode transition or an order–disorder

process that involves the ordering of pre-existing dipoles that were disordered in the high-temperature PE phase. The phase transition between PE-AFE occurs at a critical temperature, T_c . On the application of an electric field of sufficient strength, the material can switch from the low-temperature AFE phase to a FE phase with a polar space group (Figure 1A).^{4,5}

In a phenomenological description, a phase transition is typically described by an order parameter or a set of order parameters.⁶ In the case of the AFE, there are two sublattices with the same magnitude of spontaneous polarization but in opposite directions, leaving a net-zero macroscopic

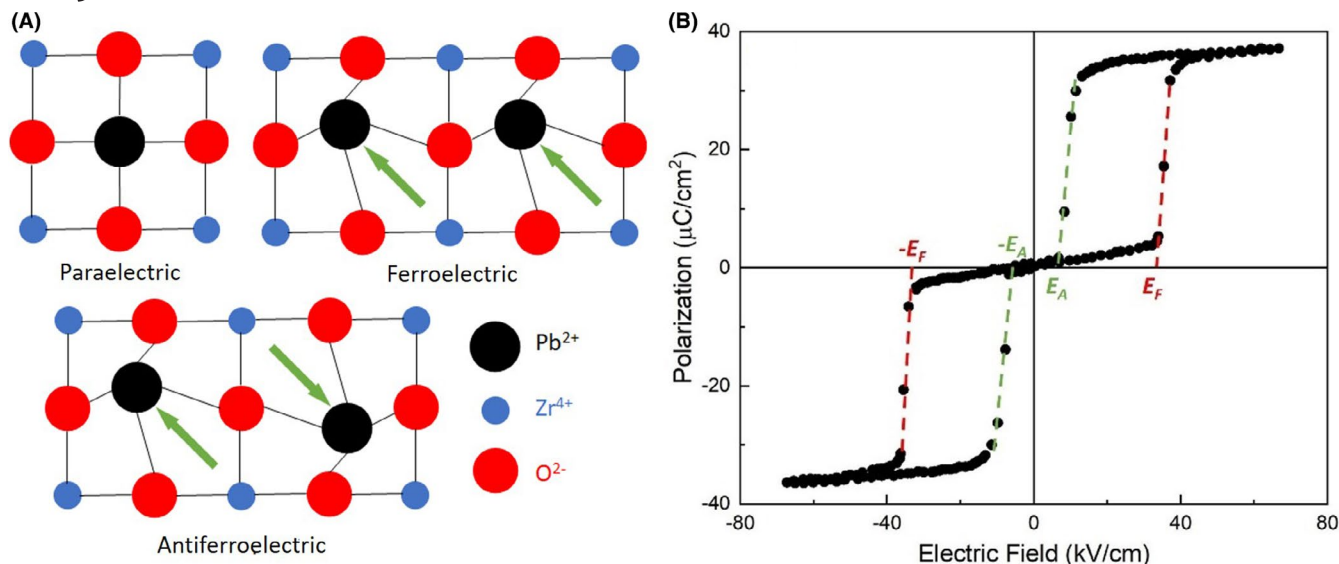


FIGURE 1 (A) Schematic representation of paraelectric, antiferroelectric, and ferroelectric states in PbZrO_3 (oxygen octahedral tilting not shown). (B) Typical double hysteresis loop measured in $\text{Pb}_{0.98}\text{La}_{0.02}(\text{Zr}_{0.66}\text{Ti}_{0.10}\text{Sn}_{0.24})_{0.995}\text{O}_3$ (replot from Ref. [7]) [Color figure can be viewed at wileyonlinelibrary.com]

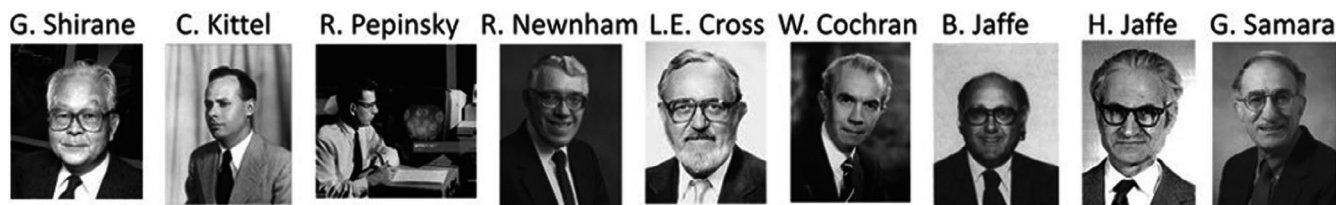


FIGURE 2 Key pioneers in the first 20 years of antiferroelectric discovery and development (1951–1970)

polarization within the crystal structure at zero field. Figure 1B shows a typical double hysteresis curve measured in $\text{Pb}_{0.98}\text{La}_{0.02}(\text{Zr}_{0.66}\text{Ti}_{0.10}\text{Sn}_{0.24})_{0.995}\text{O}_3$.⁷ Associated with AFE-FE switching, there is a critical forward coercive field, E_F , that is the field-induced AFE-to-FE phase transition. Then, on reducing the forward field, there is a switch back to the AFE phase at a different coercive field, E_A . On reversing the field direction, similar transitions are observed at $-E_F$. After saturation of the FE polarization at high fields, on reducing electric field strength to $-E_A$, the FE reverts to the AFE phase. As will be discussed below, observation of double hysteresis alone does not provide conclusive proof of a phase being AFE, as double hysteresis can also arise from randomly oriented defect dipoles in an aged FE and/or switching of a FE with a first-order phase transition temperature above the Curie temperature (T_C). Below, the experimental characteristics of AFE phases are described which collectively aid in identifying a material as AFE. Before considering these characteristics, the history of the first 20 years of AFE materials is discussed.

2 | EARLY AFE PIONEERS AND KEY DISCOVERIES FROM THE FIRST 20 YEARS

2020 was the 100-year anniversary of the discovery of ferroelectricity by Valasek (1920) in Rochelle salt. In that work, the polarization–electric field (P-E) hysteresis invited analogies to ferromagnetic materials, and hence the use of the word “ferro” as a prefix to the dielectric analog.⁸ Antiferromagnetism has been known as a phenomenon since the work of Louis Néel, in the 1930s.⁹ Following the discovery of ferroelectricity in the perovskite BaTiO_3 —in various locations, including United States, Russia, and Japan (and possibly Germany), during WWII, as scientists looked for alternative dielectric materials to replace mica for capacitor applications—antiferroelectricity was discovered.^{10–14} Figure 2 shows photos of some of the critical pioneers in AFE materials from 1951 to 1970.

The first reports on AFEs were from the Tokyo Institute of Technology (Tokyo Tech), on the perovskite AFE PbZrO_3 , in two publications from Shirane, Sawaguchi,

Takeda, (1950) and Sawaguchi, Maniwa, and Hoshino (1951).^{15–17} Kittel, at Bell Labs in 1951, provided the first theoretical justification, suggesting that antiferroelectricity should exist.¹⁸ Shirane came to Penn State and joined the X-ray structural group of Pepinsky, who at that time had a very advanced structural refinement laboratory and used diffuse scattering to aid structural determinations of polar symmetries and calculate the electron density maps around atoms. He used structural analytics to discover FE and related materials across many different crystal structures. By 1953, the second AFE phase was published and refined; this was the perovskite, PbHfO_3 .¹⁹ At that time, Newnham was a student at Penn State working in the Pepinsky group, and he published with Shirane and Pepinsky (1954) the crystal structure of the AFE NaNbO_3 .^{20,21}

Meanwhile, in the United Kingdom at the University of Leeds, Cross and Nicholson were also working on NaNbO_3 crystals and were able to show double hysteresis.²² Simultaneous to the experimental work, and inspired by the recent power of the Devonshire phenomenological modeling of the BaTiO_3 FE materials, Cross utilized the postulates in the Kittel publication and introduced a model to account for the double hysteresis observations in NaNbO_3 .²³

Outside of the perovskites, Keeling and Pepinsky (1955) studied the low-temperature (148 K) behavior of Ammonia Di-Hydrogen Phosphate ($\text{NH}_4\text{H}_2\text{PO}_4$ (ADP) and determined the order–disorder H-displacement with AFE sublattice symmetry breaking.²⁴

Another important step came with Cochran (following work of Raman, Frohlich, Ginzburg, Landau, Anderson, and Landauer and colleagues) with the elucidation of the soft mode theory for displacive phase transitions (1959).²⁵ Although it was initially introduced for ferroelastics, it was generally applicable to many displacive phase transitions, including ferrodistorptive and antiferrodistorptive ones. This theory drove many important fundamental studies coupling phonon dispersions and structural transitions.²⁶

In parallel to the fundamental work, there were important advances in the development of the PbZrO_3 - PbTiO_3 (PZT) solid solution phase diagram. While many groups contributed, the most extensive and comprehensive work came from the Clevite Corporation in Cleveland USA, and the work of Jaffe, Cook, Jaffe, Cmolik, and Berlincourt in the early 1960s.²⁷ This produced interest in the AFE-FE boundary of the PZT phase diagram for critical defense applications. Fundamental work at the defense national laboratories was also conducted to probe the physical parameters controlling the AFE phase transition behavior. Excellent work by Samara (1970) at Sandia National Laboratories reported on the hydrostatic pressure effects on the AFE transitions.^{28,29} The results correlated the empirical observations within the soft mode theory of Cochran. So, 70 years after the discovery of AFE in PbZrO_3 , there have been many other important contributions

beyond the first 20 years. Nonetheless, those first 20 years underpinned many of the important characteristics that guide current understanding.

3 | EMPIRICAL PROPERTY CHARACTERISTICS ASSOCIATED WITH AN AFE PHASE

There are several empirical observations that aid the determination and verification of an AFE phase. Below, a number of these properties, ranging from the double hysteresis, crystallographic structure, unit cell volume, stress dependence of the transition temperature, field dependence of the permittivity, low thermal conductivity, and negative electrocaloric coefficient, are considered.

3.1 | Polarization–electric field switching in the form of double hysteresis loops

Antiferroelectricity is characterized by the ability to induce a phase transition between a non-polar AFE phase and a polar FE phase, producing remarkable changes in properties. To observe the switching, the dielectric material must have the appropriate crystallographic structure with antiparallel spontaneous polarizations; the coercive fields for the transformation must be sufficiently low as to minimize conductivity and/or dielectric breakdown. So, in order to permit the field forcing the switching and thereby observe the dielectric double hysteresis response, it is imperative to minimize the extrinsic dielectric loss associated with conductivity of ionic or electronic space charge contributions that can screen and limit the energy necessary to drive AFE-FE transitions. Other than composition, external conditions can affect the AFE performance. Figure 3A is the double hysteresis in the AFE material $\text{Pb}(\text{Lu}_{0.5}\text{Nb}_{0.5})\text{O}_3$, and Figure 3B shows the linear proportionality between the E_F and temperature.³⁰ As already implied from the historically important work of Samara, the mechanical boundary conditions can also influence the properties. So, in the double hysteresis experiments, the applied stresses, and/or the ability for the material to undergo the shape changes in the AFE-FE switching, and even the electrode configuration can partially clamp the transition and should be considered.³¹ The multi-polymorphic AFE phases can also influence the nature of the hysteresis loops; this is very nicely demonstrated in single crystals of PbZrO_3 , by Fesenko et al., Figure 3C.³² Generally speaking, for a particular composition, $E_F > E_A$, whereas the sign of E_A depends on the phase. If the testing condition is away from the phase boundary, E_A has the same sign as E_F (classic double loop). However, AFE and FE phases often coexist when close to the phase boundary. Under such circumstances, the P-E loop

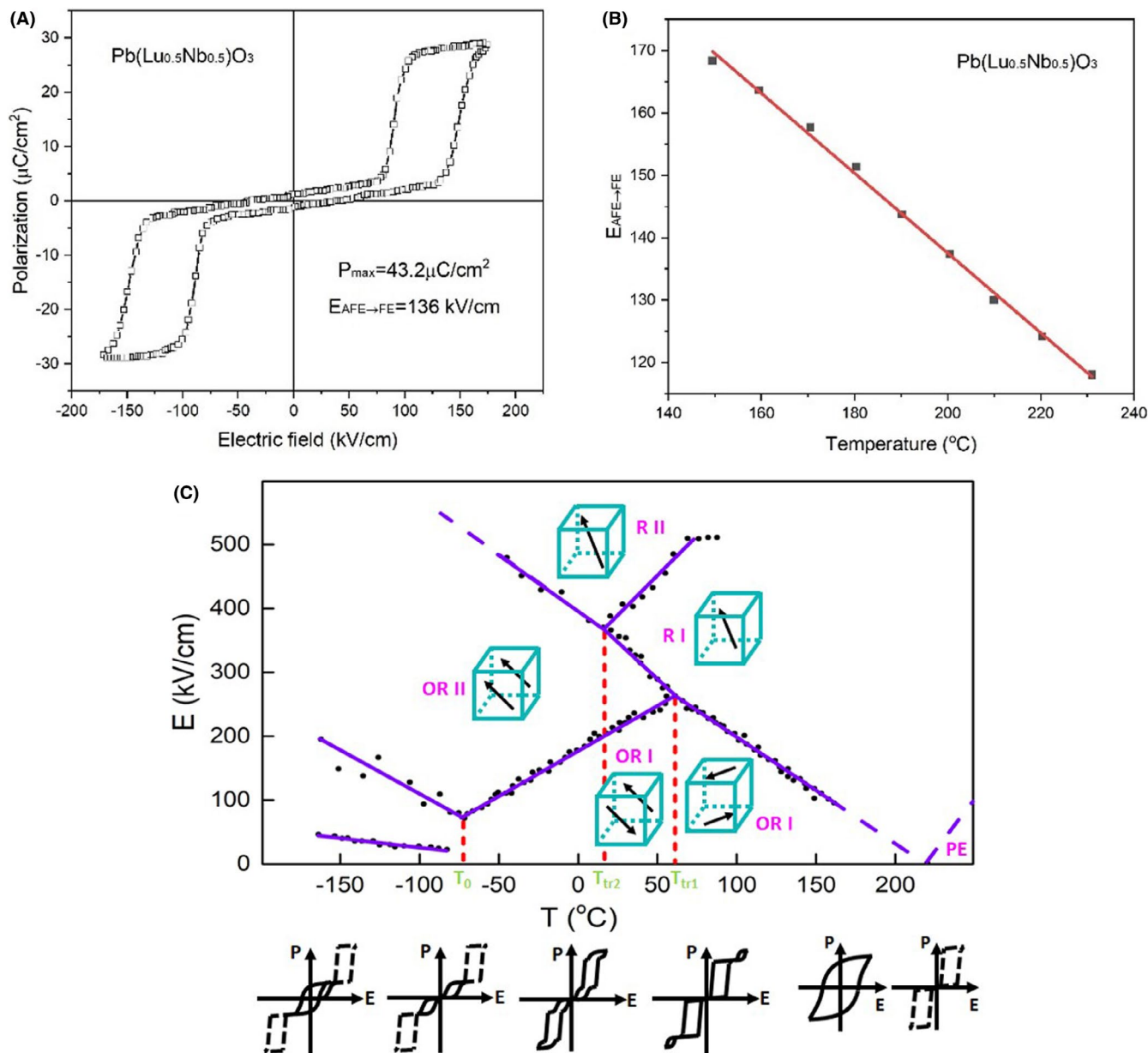


FIGURE 3 Antiferroelectric double hysteresis loops in (A) $\text{Pb}(\text{Lu}_{0.5}\text{Nb}_{0.5})\text{O}_3$ and (B) the temperature-dependent critical field in it (replotted from Ref. [30]). (C) shows the phase diagram of PbZrO_3 as a function of temperature and electrical field (replotted from Ref. [32]) [Color figure can be viewed at wileyonlinelibrary.com]

can possess a pinched shape owing to the negative E_A (assuming positive E_F). In those materials, the electric field can not only induce FE out of an AFE, but also trigger the opposite transition.^{33–35} Double hysteresis is an important observation but is not a sufficient condition for experimental verification of an AFE. Double hysteresis can also be seen in the case of FE that have randomly oriented defect dipoles, or strong aging that induces pinning of the spontaneous polarization.^{36–38} In this case, when a large enough electric field is applied, the driving force overcomes the local fields associated with the defect dipoles or aged domain state, and the polarization can be switched. However, if the timescale of the hysteresis loop is too short to allow the local fields

to be reoriented, they will act to provide a strong restoring force when the field is removed that will reduce the remanent polarization. Figure 4 shows such double hysteresis in aged KNbO_3 with acceptor doping.^{39,40} Aged FE can be de-aged by heating the materials to higher temperatures to either redistribute and/or realign defect dipoles, thereby remove the pinning. For example, running the sample through multiple hysteresis loops, with heating and realignment of defects, can also de-age and remove the double hysteresis in FE. An approach that can be used to quickly discern whether aging or antiferroelectricity is responsible for observed double hysteresis is to check the loops under different frequencies. If the double loop originates from aging, it tends to “open up” at a

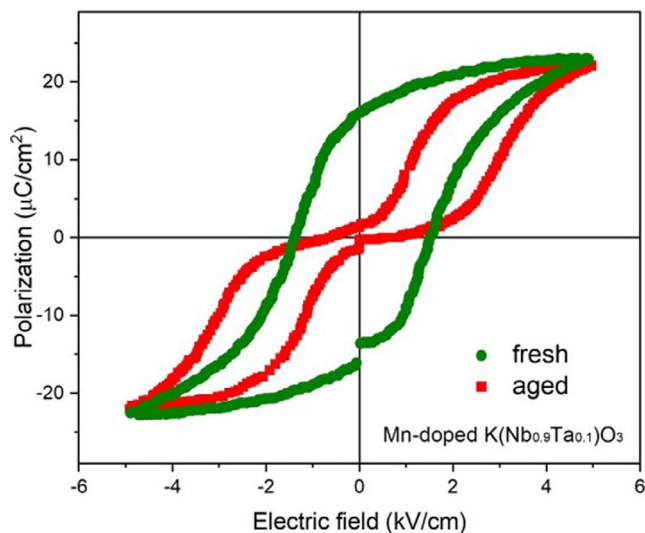


FIGURE 4 Double Hysteresis loops observed in ferroelectric Mn-KNbO₃-based materials (replotted from Ref. [39]) [Color figure can be viewed at wileyonlinelibrary.com]

sufficiently low-frequency switching and transition to a FE hysteresis loop. In contrast, real AFE exhibit much weaker frequency dependence, and presumably, the double loop remains stable under switching.

Another source of a double hysteresis is in first-order FE, at temperatures in the window between the Curie temperature and the Curie–Weiss temperature. From a free energy perspective, in such a case there are energy minima at $p = 0$, and metastable minima at finite polarizations for such a FE; an external electric field can drive a double hysteresis under these special conditions. Double hysteresis can also be observed in a narrow temperature window above the Curie temperature when the FE phase can be field-induced.

Experimentally, double hysteresis can be missed in samples with high background conductivity, or in cases where mechanical clamping obscures the behavior of a true AFE material. Therefore, the identification of an AFE phase should rely on more than the electrical analysis.

3.2 | Superlattice diffraction between the high-temperature PE and low-temperature AFE phases

As briefly described above, the structural phase transition between the nonpolar PE and an antipolar AFE involves the formation of two antiparallel polarization sublattices. This necessitates changing the translational symmetry of the structure of the AFE relative to the PE to account for the need for multiple prototype cells to reach a true repeat unit in the AFE phase. One consequence of this is that the AFE phase has additional diffraction spots/lines relative to the PE diffraction pattern. As an example, in PbZrO₃, the local dipoles

orient along $\langle 110 \rangle$ directions and form an antiparallel arrangement with two by two alternation; this will be described further below. Consequently, the net polarization is canceled to zero, whereas the lattice parameter is quadrupled along $\langle 110 \rangle$, which gives rise to the $\frac{1}{4}\{110\}$ type superlattice diffraction reflections and necessitates defining a new unit cell comprised of eight prototype cells.⁴¹ However, it is essential to be very careful when using the superlattice diffraction to determine the phase. First, $\frac{1}{4}\{110\}$ spots could be invisible if the observation direction is not perpendicular to the modulation, hence a systematic investigation is needed. Second, many other superlattice diffractions are potentially confounding, for instance, those owing to an anti-distortive phase transition, such as the antiphase octahedral tilting associated with the AFE/FE phase that typically leads to $\alpha(\frac{1}{2}\{110\})$ and $F(\frac{1}{2}\{111\})$ superlattice spots.⁴² So, a translational symmetry signature is an important and necessary property, but again, extra care is demanded for an appropriate analysis.

3.3 | Unit cell volume changes relative to PE-AFE phases

AFE–PE phase transitions can be first or second order, although many cases are first order with all of the related characteristics. That is, transitions of this type show a discontinuous onset of the order parameters at the transition temperature, a thermal hysteresis, a discontinuous change of the unit cell volume, and a latent heat anomaly associated with the volume change in accordance with the Clausius–Clapeyron relationship. The change in the unit cell volume is a noteworthy parameter that aids in the determination of the AFE relative to a FE phase. PE-AFE transitions lead in perovskites, in general, to a lower unit cell volume relative to the PE unit cell; in contrast, the opposite is true for the PE-FE transition (note that this is not generally true for other structure types). So, there is a contraction in volume for the AFE, and an expansion in volume for the FE on cooling through the transition temperature. This has important consequences on both the hydrostatic pressure effects and the electrocaloric effect (ECE). Figure 5A,B contrasts the PE-AFE lattice parameters for PbZrO₃, and the PE-FE-FE (cubic-tetragonal-orthorhombic) phase transitions in the BaTiO₃ perovskites.^{43,44}

3.4 | Hydrostatic pressure dependence of phase transition behavior

The differences in volume change between AFE and FE phases relative to the volume of the PE phase induce consequences on the stability of these phases as a function of the applied external pressure. As higher hydrostatic pressures

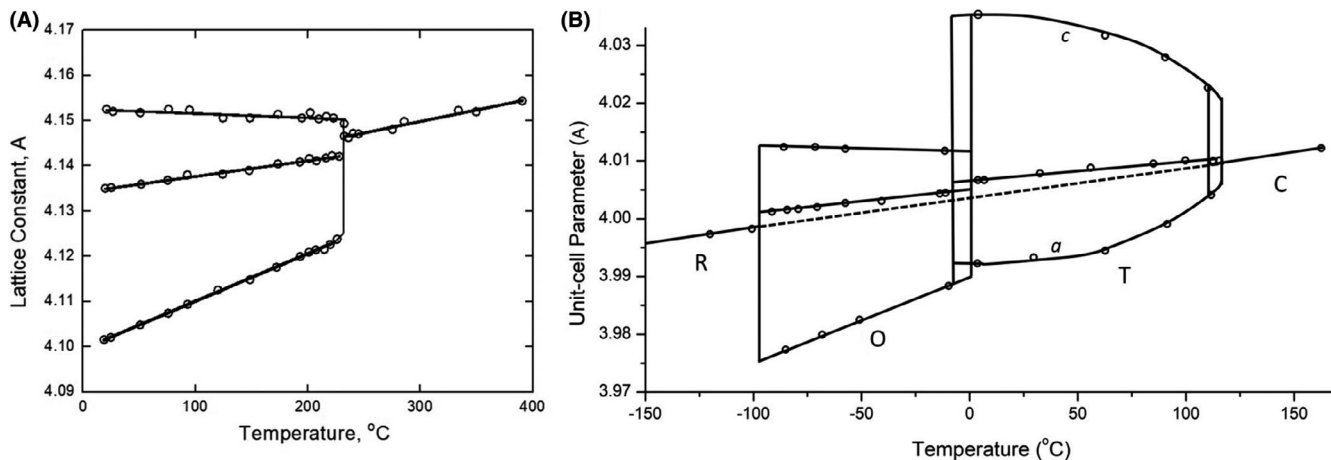


FIGURE 5 Lattice parameters as a function of temperature for (A) antiferroelectric PbZrO₃, showing the decrease in lattice volume on cooling through the phase transition temperatures (replotted from Ref. [43]), and (B) ferroelectric BaTiO₃, showing the expansion in the lattice volume on cooling into the tetragonal ferroelectric phase; C is the cubic paraelectric phase, T is tetragonal, O is orthorhombic, and R is a rhombohedral ferroelectric phase, the dashed line is the cube root of the unit volume of the cell as a function of temperature (replotted from Ref. [44])

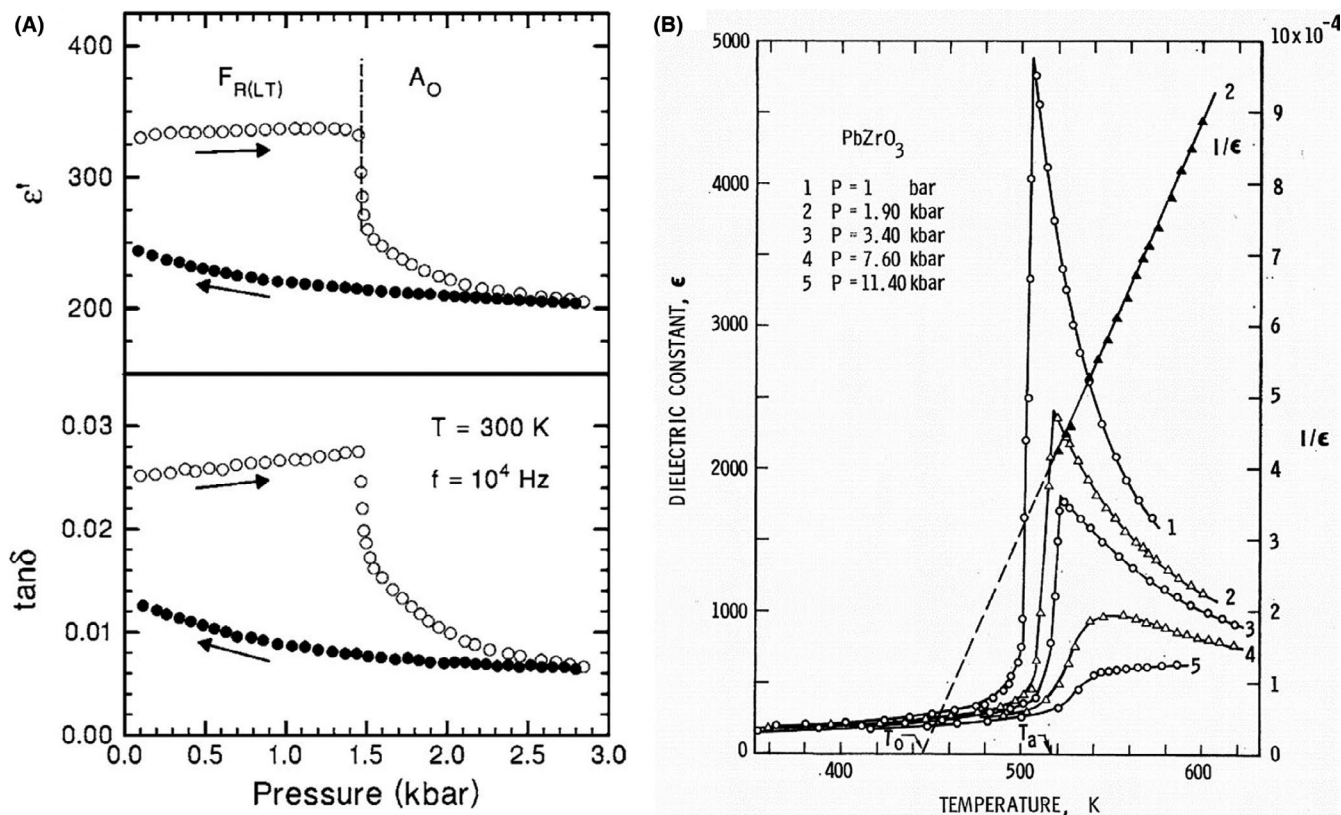


FIGURE 6 (A) Variations of ϵ' and $\tan\delta$ for increasing and subsequent decreasing pressure in PZT 95/5; (reproduced by permission from Ref. [45]). (B) Isobaric hydrostatic pressures (1 bar to 11.4 Kbar) and temperature dependence of the phase transition behavior of antiferroelectric PbZrO₃, and the Curie–Weiss plot of the dielectric permittivity in the paraelectric regime (reproduced by permission from Ref. [28])

favor higher densities (and hence smaller prototype unit cell volumes) pressure increases the stability of perovskite AFE phases to a higher temperature, whereas the FE phase stability is suppressed to lower transition temperatures. Thus, a PE-AFE has a $dT_c/dp > 0$, and the PE-FE is $dT_c/dp < 0$. If

the pressure is applied near the AFE/FE phase boundary, pressure-induced FE to AFE phase transitions can take place (Figure 6A).⁴⁵ Samara also showed the effects of pressure on the magnitude of the permittivity and the diffuseness of the phase transition; these are discussed later in context with the

soft mode theory. Figure 6B shows Samara's experimental data of the hydrostatic pressure dependence on the dielectric anomaly for PbZrO_3 ceramics.²⁸

Uniaxial stress also alters the phase transition behavior in AFEs; this becomes more complicated when an electric field is applied simultaneously. In general, isostatic stress also favors the AFE phase over FE, which leads to an increase of the critical field E_F .⁴⁶ Moreover, the polarization of the induced FE phase is suppressed via the piezoelectric effect. It was found that, when subjected to a compressive stress, the $\langle 001 \rangle_c$ axis of the AFE lattice (the dipoles are along $\langle 110 \rangle_c$) tends to align with stress, resulting in a remanent strain.⁴⁷ Moreover, an electric field can also texture the AFE domains, but in a different way. Prior to the field exposure, AFE domains are randomly oriented. After one AFE—FE—AFE cycle, however, the $\langle 001 \rangle_c$ axis rotates toward the plane perpendicular to the field direction.⁴⁸

In the cases of compressive and tensile stresses, these stresses the situation is more complex as often in the experimental setup there can be local deviatoric stress gradients that break the symmetry that in turn then favors the polarized regions and the FE phase. So, the volume change can be compromised with these gradients, hence most studies on the phase transitions are performed with hydrostatic pressure applications.

3.5 | Electric-field-dependent permittivity in AFE

The field-induced transition of the AFE phase to the FE phase changes the polarizability of the dielectric, and so increases the permittivity (ϵ) with increasing field strength, $d\epsilon/dE > 0$.² This is the opposite trend from FE, where $d\epsilon/dE < 0$. That is, high fields reduce the permittivity of FE materials; that process is often referred to as voltage saturation behavior. This field dependence of the dielectric permittivity can provide additional evidence for a phase being an AFE or FE. In addition, the phase transition temperatures vary with external fields. Normally, both AFE-FE and AFE-PE transition temperature shift towards the AFE side under a DC field (i.e., DC fields reduce the stability of the AFE phase).⁴⁹

3.6 | Thermal conductivity in AFE's

In general, FE with long-range order, such as normal FE, have relatively higher thermal conductivities due to the comparatively long phonon mean-free path. Relaxor FE, with their nanopolar domains, have a polar glassy behavior that strongly reduces the thermal conductivity (due to phonon scattering from the nanoscale heterogeneities). Likewise, under zero electric field, AFE also have very low thermal

conductivities. There is a lot of disorder in the antipolar ordering that leads to the scattering of phonons and thereby suppresses the thermal conductivity. Figure 7 shows experimental data of the temperature dependence of the thermal conductivity in FE and related materials, with AFE NaNbO_3 having phonon glass behavior. At 100 K, there is about an order of magnitude between the thermal conductivities with PE and normal FE perovskites such as KTaO_3 , BaTiO_3 , PbTiO_3 , and KNbO_3 where $\kappa \sim 10 \text{ W m}^{-1} \text{ K}^{-1}$ and in an AFE such as NaNbO_3 $\kappa \sim 1 \text{ W m}^{-1} \text{ K}^{-1}$. It is also noted that relaxor FE such as $\text{Pb}(\text{Mg}_{1/3}\text{Nb}_{2/3})\text{O}_3$ have nanoscale polar regions also show extremely low thermal conductivities, $\kappa \sim 1 \text{ W m}^{-1} \text{ K}^{-1}$.⁵⁰

3.7 | Electrocaloric coefficients in AFE's and FE's

The ECE is of interest for potential applications in solid-state cooling.^{51,52} The operating premise is that the entropy of dipole alignment can be changed under an applied electric field. This, in turn, can be used to provide a temperature change under an electric field. Both AFE and FE materials are of interest for this phenomenon. Figure 8A shows a series of temperature changes that can be induced by applied electric fields. In FEs, the applied field aligns the polarization, and hence reduces the dipole entropy associated with an

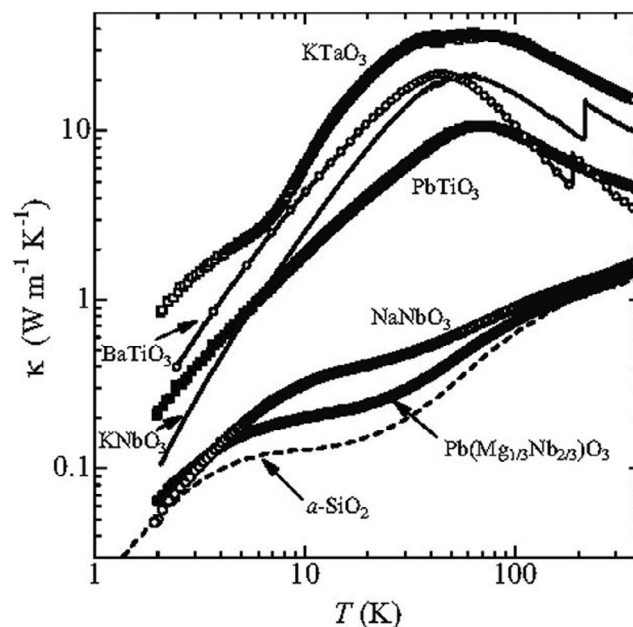


FIGURE 7 Thermal conductivity of various perovskite materials with different ferroic structures ranging from paraelectric (KTaO_3), ferroelectric (BaTiO_3 , KNbO_3 , PbTiO_3), antiferroelectric (NaNbO_3), and relaxor ferroelectricity ($\text{Pb}(\text{Mg}_{0.33}\text{Nb}_{0.67})\text{O}_3$). All of these are contrasted with amorphous silica (reproduced by permission from Ref. [50])

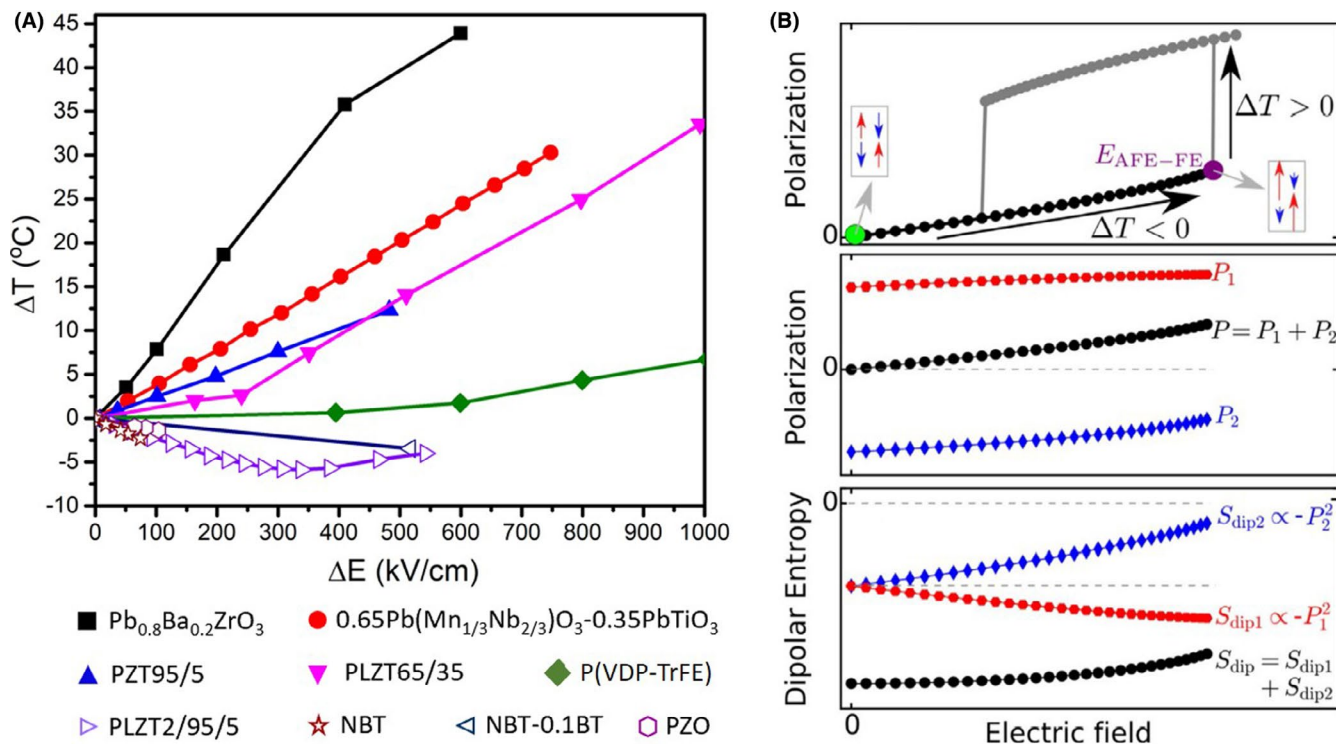


FIGURE 8 (A) Electrocaloric responses in ferroelectric (solid symbol) and antiferroelectric (AFE) (unfilled symbol) materials (replotted from Ref. [53]); (B) Schematic illustration of the inverse electrocaloric effect in AFE phases based on the different responses of the two sublattices (reproduced by permission from Ref. [54]) [Color figure can be viewed at wileyonlinelibrary.com]

originally partially random domain configuration. Under the adiabatic condition, the material is therefore heated, $dT > 0$. In contrast, AFE show a negative ECE, where the isothermal entropy change, ΔS , is positive (Figure 8B) and the adiabatic temperature change, ΔT , is negative under an increasing electric field.^{53–55} The negative ECE sign in AFEs was suggested to originate from the dipole disruption by moderate field, but may also be associated with the phase transition sequence and the presence of commensurate/incommensurate ordering.

The above experimental observations, combined with structural refinement diffraction data or high-resolution transmission electron microscope images of antiparallel atomic displacements, can be used to identify AFE unambiguously.

3.8 | Soft modes, structural phase transition, and flexoelectricity

Lattice dynamics and the associated phonon spectra control the thermal properties of a material. In addition, in the case of special lattice vibration modes that soften (i.e., the frequency drops to zero), the phonon mode signals structural phase transitions. While the theory was first developed for displacive transitions, it was later extended also to order-disorder transformations.^{56–58} The soft mode describes the atomic displacements within the unit cell and the phase

modulation of the relative displacement amplitudes from one unit cell to another with the wavevector of the lattice vibration. One common case is that of a FE phase transition driven by a soft mode. Here, there is a transverse optic phonon mode with relative displacements between the anions and cations. It has an angular frequency, ω_s , at $K = 0$, or $\lambda \rightarrow \infty$; this is the Brillouin zone center. The soft mode frequency, ω_s , varies with temperature according to $\omega_s^2 = A(T - T_c)$. Thus, as the temperature approaches T_c , the frequency approaches zero, and then the material freezes in the new structure. The optic transverse soft mode also accounts for the dielectric anomaly around T_c , the so-called Curie Law. The Curie Law can be correlated to the temperature dependence of the soft mode frequency via the so-called Lydanne–Sachs–Teller (LST) relations. The LST equation describes the low and high-frequency dielectric responses as being a function of the longitudinal and transverse frequencies of the optical phonon modes. Figure 9A illustrates the concept of the optical soft mode freezing in and driving the PE-FE phase transition.⁵⁹

The soft mode theory can also describe the case in which the optical phonon freezes at the Brillouin zone edge. Here the critical wave vector is $k = \pi/na$, and this produces a vibrational mode that has a wavelength of two-unit cells for $n = 1$. Given that the displacements are antiparallel in the adjacent unit cells, this would constitute the AFE superlattice cell. There are other positions that lead to more complex

FIGURE 9 A schematic of soft mode condensation of a transverse optical phonon for (A) ferroelectrics and (B) antiferroelectric phase transitions (reproduced by permission from Ref. [59]) [Color figure can be viewed at wileyonlinelibrary.com]

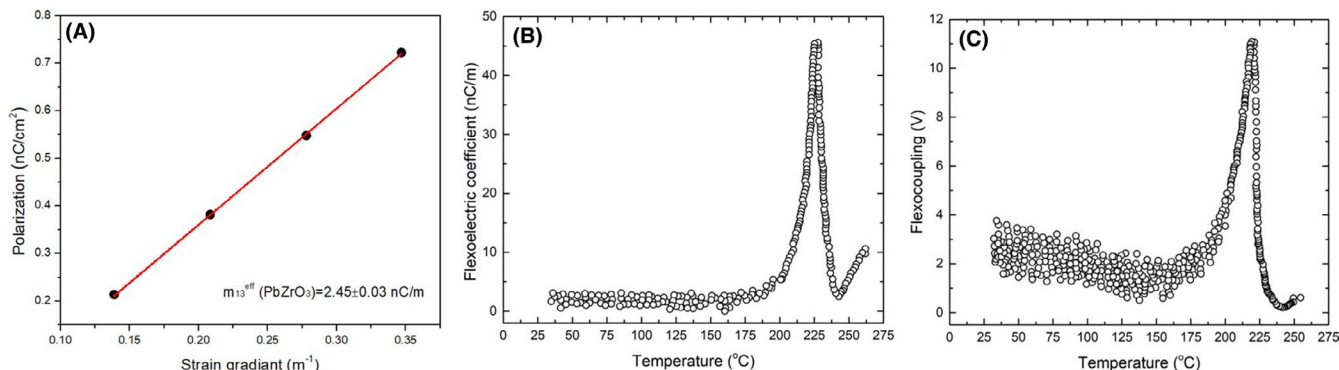
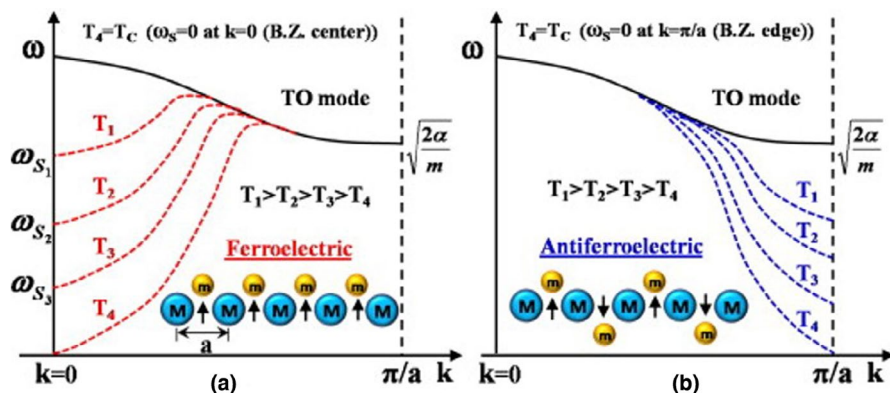


FIGURE 10 (A) Flexoelectric coefficient at RT, (B,C) flexoelectric coefficients, flexocoupling as a function of temperature in PbZrO_3 (replotted from Ref. [64]) [Color figure can be viewed at wileyonlinelibrary.com]

situations, for example, one in which the critical wave vector, $k = \pi/na$ with $n = 2$, leads to polarization sequences with two up and two down, somewhat akin to the PbZrO_3 case where along $\langle 110 \rangle_c$, there are two up and down polar displacements; these are simplified and shown in Figure 9B. In addition to the temperature dependence of the soft mode freezing, hydrostatic pressure can also impact the condensation process.

In the cases where n is not an integer, the soft mode may condense at irrational positions in the Brillouin Zone. This induces incommensurate (INC) phase transitions, in which the superlattice structures and frozen-in vibration modulations have wavelengths that may be extremely large and have symmetries that cannot be classified under the constraints of the three-dimensional basis and symmetry operations with the 230 space groups. The superlattices are also not at rational positions that correspond to simple multiplicities of the PE unit cell. The wavelength of these modulations can be temperature dependent and can converge with lower temperatures toward a rational multiplicity for the superlattice. The temperature evolution from the INC to the commensurate phase is often pinned by defects; if these defects are not limited, the critical temperature from INC to Commensurate is the lock-in transition. The INC structures are often associated with competing phase transitions, and therefore it is natural to see a close correlation with INC with FE and AFE phase

being close in energy, and/or through coupled soft modes within the Brillouin Zone.⁶⁰

Flexoelectricity is the induction of a polarization that is possible in all insulating materials when subjected to an inhomogeneous strain or stress, that is, a strain or stress gradient.^{61–63} Most of the historical discussion around electromechanical behavior was linked to electrostriction, and in the case of non-centrosymmetric materials, piezoelectricity. But in some cases, particularly when the relative permittivity is large, flexoelectricity must be considered when there are strong gradients within a material. This is particularly true in the case of AFEs, as they have high local polarization gradients both at the domain level where there is a large strain mismatch at complex domain configurations and large polarization gradients on the lattice level with antipolar ordering. In both ferroelectrics and AFEs which pair local polar order with low or zero net polarization, and a high permittivity, flexoelectric contributions are large, and not obscured by piezoelectricity. Hence, flexoelectricity is discussed in this AFE review. Vales-Castro et al. have experimentally determined the flexoelectric coefficients in both PbZrO_3 and AgNbO_3 , as shown in Figure 10).⁶⁴ In that work, it was pointed out that the flexoelectricity and flexocoupling coefficients show a sharp peak at the AFE phase transition. While these coefficients are not as high as in materials such as $\text{Ba}_{1-x}\text{Sr}_x\text{TiO}_3$, most AFE lack the nanopolar regions (as in

Ba_{1-x}Sr_xTiO₃) that significantly increase the reported flexoelectric coefficients.^{65,66}

Tagantsev et al. point to the possibility that flexoelectric coupling is essential to the development of AFE behavior in PbZrO₃.⁶⁷ In their work, the gradient terms in Landau–Ginzburg–Devonshire phenomenology (the same terms that determine the domain wall energies in FE and/or the modulations that are inherent to the INC phase) coupled with high dynamic flexoelectric coefficients are shown to influence the phase transition. The result is that a FE-like lattice instability is interrupted by incommensurate modulations as described by Axe et al.⁶⁸ Specifically, the dynamic flexoelectric effect that underpins the coupling between the acoustic and transverse optic modes drives a phonon frequency softening at the Brillouin zone center. An Umklapp interaction then leads to bypass of the incommensurate state and produces the locked-in polar order of PbZrO₃. Within the soft mode theory, these large flexoelectric couplings between the optical branch push the acoustic branch to zero frequency at a certain point with $q = 0$ in the Brillouin zone, leading to a soft mode condensation at an irrational point in the Brillouin Zone, and this then leads to the INC antipolar modulations. This model is also consistent with the work of Borisevich et al. on Sm-doped BiFeO₃ AFE.⁶⁹ It is clear, though, that additional experimental and modeling work in this area would benefit the field, and would help test the universality of the role of flexoelectricity in AFE materials.

3.9 | Size effects in AFEs

As with many ferroic phase transitions, the material properties can change with either the dimensions or size of the coherent crystal; moreover, the relative stability of the various phases can also change.^{70–74} There are two major types of size effects, namely intrinsic and extrinsic. Intrinsic size effects are related to changes that are associated with the nature of the phase transition, including the transition temperature, diffuseness of the transitions, and magnitudes of the anomalous properties related to the phase transition. Eliseev et al. have considered phenomenological calculation for AFEs and predicted the loss of double hysteresis loops with thin-film thickness.⁷⁵ An alternative prediction was made using first-principles calculation by Mani et al., where a size-driven phase transition from AFE (PbZrO₃) to a FE phase in nanoscale epitaxial thin films under short circuit conditions. These predictions at this time have not been experimentally verified, as sufficiently thin films to test this prediction have not been produced to sufficient quality, and free of strain effects.⁷⁶

There are also extrinsic properties in the size or field-induced FE phase that are impacted by the ferroic domains and their contributions to properties. Material properties,

such as permittivity and the piezoelectric coefficients, are affected by the movement of the domain walls.^{77,78} In the case of AFEs, there are no major extrinsic contributions associated with mobile domain boundaries, and hence the dielectric losses are often lower in the case of AFE. This assumes that under an electric field, the movement of a domain wall separating two AFE variants, there is no net polarizability as a consequence of the antipolar alignment limits such contributions. Only polarizability and extrinsic properties contributions are possible with a transition to a nucleating FE phase. Further discussions on the nature of the structure of AFE domain walls are discussed below. Also, in the case of FE, the need for continuity of the polarization in the absence of incomplete screening can drive the size effect. However, the AFE phase can be perturbed by symmetry breaking at the surface. The surface energy can significantly contribute to the structural phase transition at nanoscale and drive the phase transition temperature lower; this also increases the diffuseness of the transition anomalies and the structural distortion strain relative to prototype and the magnitude of the permittivity maxima. These trends are experimentally shown for the AFE PbZrO₃ by Chattopadhyay et al.⁷⁹ The extrinsic size effects that are often found in the case of the FE may well be important, but at this time there is a lack of reported evidence with the high field size effects when the field drives the AFE to the FE phase. One would hypothesize that there should be extrinsic size effects under such conditions.

4 | ANTIFERROELECTRIC PHENOMENOLOGICAL THEORETICAL PERSPECTIVES

The very first theoretical model to describe an AFE phase transition was proposed by Kittel, who employed a two sublattice model with each sublattice having its independent spontaneous polarization \vec{P}_a and \vec{P}_b .¹⁸ In such a two-sublattice model, the different FE states of a crystal are distinguished by the relative values of \vec{P}_a and \vec{P}_b (Table 1). For example, $\vec{P}_a = -\vec{P}_b \neq 0$ corresponds to the AFE state.

TABLE 1 Distinguishing different polar states based on a two sublattice description of polarization (\vec{P}_a and \vec{P}_b) and ferroelectric and antiferroelectric order parameters (\vec{p} , \vec{q})

Phases	Sublattice polarization	Order parameters
Paraelectric phase	$\vec{P}_a = \vec{P}_b = 0$	$\vec{p} = 0, \vec{q} = 0$
Ferroelectric phase	$\vec{P}_a = \vec{P}_b \neq 0$	$\vec{p} \neq 0, \vec{q} = 0$
Ferrielectric phase	$\vec{P}_a \neq \vec{P}_b \neq 0$	$\vec{p} \neq 0, \vec{q} \neq 0$
Antiferroelectric phase	$\vec{P}_a = -\vec{P}_b \neq 0$	$\vec{p} = 0, \vec{q} \neq 0$

Kittel discussed the possibility of both second and first-order AFE phase transitions and their characteristics by writing down a Landau potential as a function of the sublattice polarization \vec{P}_a and \vec{P}_b . Such a sublattice model is a mixed microscopic description of polarization at the unit cell scale and a continuum description of the thermodynamics.

Cross and Okada formulated a consistent continuum phenomenological description of AFE phase transitions by introducing an AFE vector order parameter (\vec{q}) in addition to the FE vector order parameter (\vec{p}), which can be related to the two-sublattice spontaneous polarizations, that is, $\vec{p} = (\vec{P}_a + \vec{P}_b)/2$ and $\vec{q} = (\vec{P}_a - \vec{P}_b)/2$.^{80,81} Such a formulation has been applied by Haun et al. to study the antiferroelectricity in bulk PbZrO₃ and Eliseev et al. in AFE films.^{75,82,83} A similar model was presented by Balashova and Tagantsev by coupling a structural and FE order parameter to describe the FE to AFE phase transition and corresponding dielectric responses under applied electric fields.⁸⁴

It should be emphasized that it is entirely possible there might exist AFE phases in which there are more than two sublattices that have finite spontaneous polarization values. Furthermore, the polarizations associated with the sublattices of AFE phase are usually different from those of the FE phase within the same crystal in the absence of an applied electric field, that is, the AFE state and the corresponding FE states may not be simply related by flipping the polarization on one of the two sublattices. For example, in the Sm-doped BFO system, the spontaneous polarization is oriented along the [111] direction for the FE state, whereas it is along [110] for the AFE state.⁶⁹ Xue and Chen recently extended the phenomenological theory for antiferroelectricity by defining two independent FE and AFE order parameters, which allow the FE polarization directions to be entirely different from the AFE state.⁸⁵ Using the unpolarized and unstressed state at the same temperature as the reference, the general free energy density of a crystal g can be expressed as

$$g(p_i, q_i, E_i, \sigma_{ij}) = a_{ij}p_i p_j + a_{ijkl}p_i p_j p_k p_l + a_{ijklmn}p_i p_j p_k p_l p_m p_n \\ + b_{ij}q_i q_j + b_{ijkl}q_i q_j q_k q_l + b_{ijklmn}q_i q_j q_k q_l q_m q_n \\ + t_{ijkl}p_i p_j q_k q_l - E_i p_i - \frac{\epsilon_b}{2} E^2 \\ - \frac{1}{2} s_{ijkl} \sigma_{ij} \sigma_{kl} - Q_{ijkl} p_i p_j \sigma_{kl} - \Lambda_{ijkl} q_i q_j \sigma_{kl},$$

where the Einstein summation convention is adopted. In the above equation, p_i and q_i represent the i th components of FE and AFE order parameters, respectively; a_{ij} , a_{ijkl} , and a_{ijklmn} are the second and higher order FE dielectric stiffnesses with their non-zero components determined by the crystalline symmetry of the reference crystal; b_{ij} , b_{ijkl} , and b_{ijklmn} are the AFE dielectric stiffnesses with their non-zero components determined by symmetry; t_{ijkl} are coupling coefficients between the FE and AFE order parameters; s_{ijkl} is the mechanical compliance tensor; σ_{ij} is stress; and Q_{ijkl} and Λ_{ijkl} are FE and AFE electrostrictive

coefficients, respectively. The free energy density is written as a sixth order to allow the possibility of either a second-order or a first-order phase transition, depending on the values of the coefficients. Typically, all the free energy coefficients are assumed to be independent of temperature except the second-order stiffness coefficients a_{ij} and b_{ij} , which are assumed to be linearly dependent on temperature. Here only the coupling term between p_i and q_i is included for simplicity. With a given set of coefficients, the stability regions of different states can be obtained by minimizing the free energy with respect to p_i and q_i under a given stress or strain and electric field, and temperature–strain–electric-field phase diagrams can be constructed.

5 | CRYSTAL STRUCTURES AND CRYSTALLOGRAPHY OF AFES

This section will cover some of the important crystal structures that host antiferroelectricity.

5.1 | Perovskite structure and AFE

The ABO₃ perovskite structure has a B-cation site that is octahedrally coordinated and an A-site cation site that is 12-fold coordinated. The prototype cubic perovskite structure is shown in Figure 11A.⁸⁶ Various cooperative displacements of cations develop through the phase transition and can lead to lower symmetry phases: polar or non-polar. There are many different perovskite compounds that have an AFE phase; these include PbZrO₃ (PZ), PbHfO₃ (PH), (Na_{0.5}Bi_{0.5})TiO₃ (NBT), Pb(Yb_{0.5}Nb_{0.5})O₃ (PYN), Pb(Lu_{0.5}Nb_{0.5})O₃ (PLN), Pb(Co_{0.5}W_{0.5})O₃ (PCW), Pb(Mg_{0.5}W_{0.5})O₃ (PMW), and Pb(In_{0.5}Nb_{0.5})O₃ (PIN).^{87–110} Also, there are many solid solutions between each of these compounds and other solid solutions with AgNbO₃, NaNbO₃, and doped BiFeO₃; these will be discussed in more detail later.

Some of the details of the nature of the AFE state and the structures of many AFE are controversial, and in recent times, first-principle calculations have added a clearer understanding of the energetics of the phases and structures. Many AFEs within the perovskite structures are complex, and this is related to associated octahedral tilt transitions, impurities, and non-stoichiometric perturbations. As described earlier, through a lattice dynamics investigation, Tagantsev et al. point out that incommensurate phase transitions are an important factor influencing the AFE state. The phase transition of PbZrO₃ is $T_c \sim 505$ K. PbZrO₃ has an orthorhombic structure (Pbam) on cooling from the PE phase. Figure 11B,C show the basic AFE structure of PbZrO₃.

In the case of the PbHfO₃, there is a different phase sequence; on cooling below the cubic phase, at 493 K, the structure is tetragonal, but with the $c/a < 1$; from $441 < T$

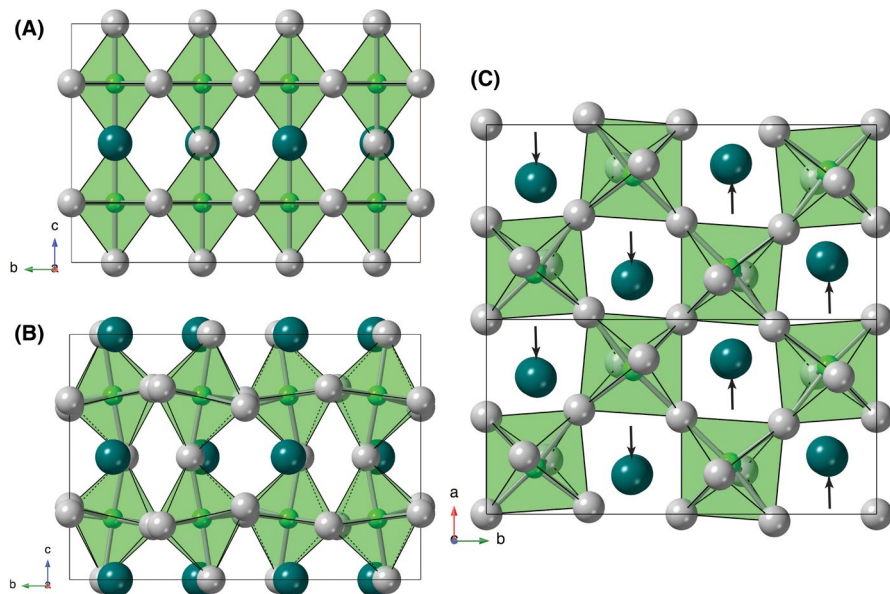


FIGURE 11 Crystallography of PbZrO_3 , after Corker et al.⁸⁶ Pb are the large dark green colored atoms, Zr is light green, and O is grey. The ZrO_6 octahedra are shown. (A) View of the prototype cubic structure along the a axis of an orthorhombic cell (to facilitate the comparison to the antiferroelectric phase). View of the antiferroelectric polymorph viewed along (B) the a axis and (C) the c axis. The arrows in (C) show the orientation of the local polarization due to Pb displacements; it is clear that the polarization cancels at a unit cell level. [Color figure can be viewed at wileyonlinelibrary.com]

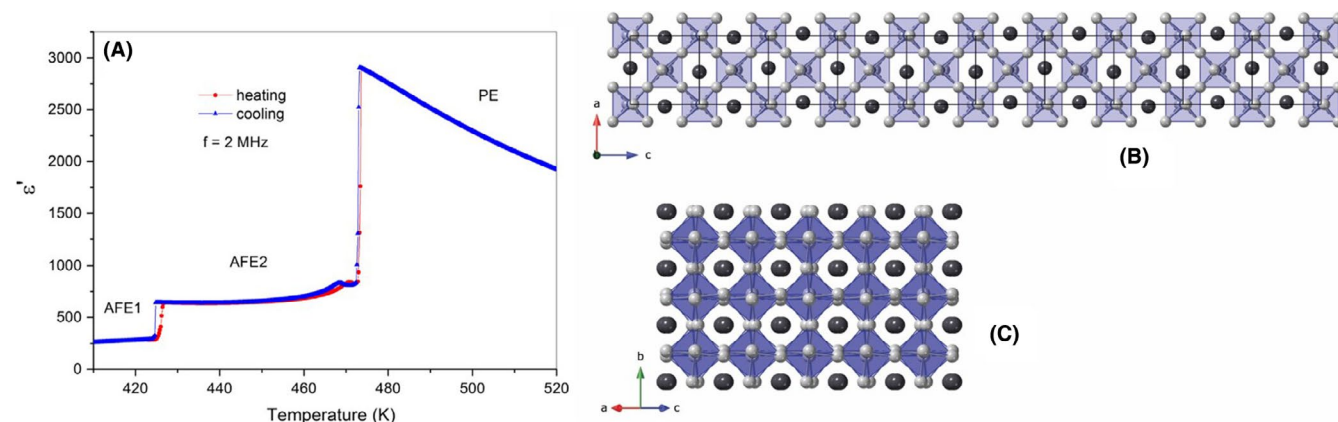


FIGURE 12 (A) Phase transition sequence in PbHfO_3 (reproduced by permission from Ref. [96]). (B,C) Representation of the incommensurate modulations in the structure of PbHfO_3 , after Bosak et al.¹¹² (B) The Pb atoms (shown as dark circles) are modulated predominantly in the $[110]$ of the cubic prototype group. (C) the structure also has an octahedral tilt [Color figure can be viewed at wileyonlinelibrary.com]

(K) < 493, a lower temperature orthorhombic AFE phase is isomorphic with PbZrO_3 .¹¹¹ Figure 12A shows the dielectric-temperature data and Figure 12B incommensurate modulation for PbHfO_3 .⁹⁷ It was recently reported that this system also has an INC structural transition (Figure 12B,C).¹¹²

Niobate perovskites such as NaNbO_3 and AgNbO_3 have multiple octahedral tilt transitions. Near room temperature, there is an AFE phase that has the orthorhombic space group Pbcm , with the antipolar distortions coming from the Nb–O bonds. In the case of NaNbO_3 , there are two phases that are very close in energy; these are the so-called P and Q phases that are antipolar Pbma and polar phase $\text{P2}_1\text{ma}$, as shown in Figure 13.¹¹³ This manifests itself in co-existence of both these phases in the NaNbO_3 , and these can limit the observation of the double hysteresis loops.^{114–116} However, as will be discussed below, strategic solid solutions can stabilize the AFE phase over the FE phase.^{117,118}

AFE also occurs in double perovskites, $\text{Pb}(\text{B}'_{0.5}\text{B}''_{0.5})\text{O}_3$, that have two cations which can experience ordered occupancy on the B site. This produces a unit cell with a $2a_0 \times 2a_0 \times 2a_0$ cell (relative to the prototype cubic cell), with a superlattice structure associated with the F-centered ordering of the respective B'-cations. At low temperatures, $\text{Pb}(\text{Lu}_{0.5}\text{Nb}_{0.5})\text{O}_3$, $\text{Pb}(\text{Yb}_{0.5}\text{Nb}_{0.5})\text{O}_3$, $\text{Pb}(\text{Lu}_{0.5}\text{Ta}_{0.5})\text{O}_3$, $\text{Pb}(\text{Yb}_{0.5}\text{Ta}_{0.5})\text{O}_3$, $\text{Pb}(\text{Co}_{0.5}\text{W}_{0.5})\text{O}_3$, $\text{Pb}(\text{Mg}_{0.5}\text{W}_{0.5})\text{O}_3$, and $\text{Pb}(\text{In}_{0.5}\text{Nb}_{0.5})\text{O}_3$ have been found to be AFE. The electrostatic energy and strain difference between the B' and B'' cations induce long-range order at the high temperatures of crystal growth and/or conventional sintering.

In $\text{Pb}(\text{In}_{0.5}\text{Nb}_{0.5})\text{O}_3$, an order-disorder transformation for the In and Nb ions can be controlled with appropriate thermal annealing and/or quenching. B-site order with intermediate length scales yields relaxor FE response, whereas the ordered state is AFE.^{109,110,119–121} Figure 14A contrasts the dielectric

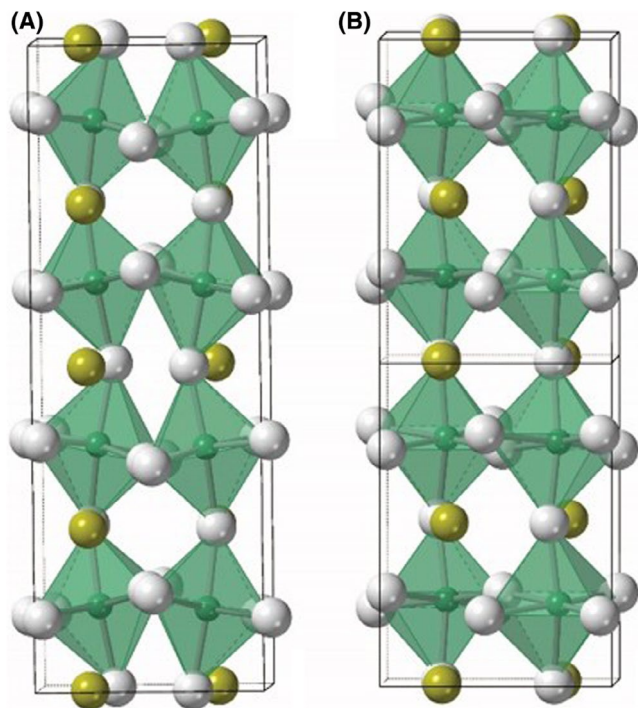


FIGURE 13 Crystal structures of NaNbO₃, after Johnston et al.¹¹³ (A) antipolar P phase, (B) polar Q phase. with Na⁺ gold, Nb⁺⁵ green, O⁻² white [Color figure can be viewed at wileyonlinelibrary.com]

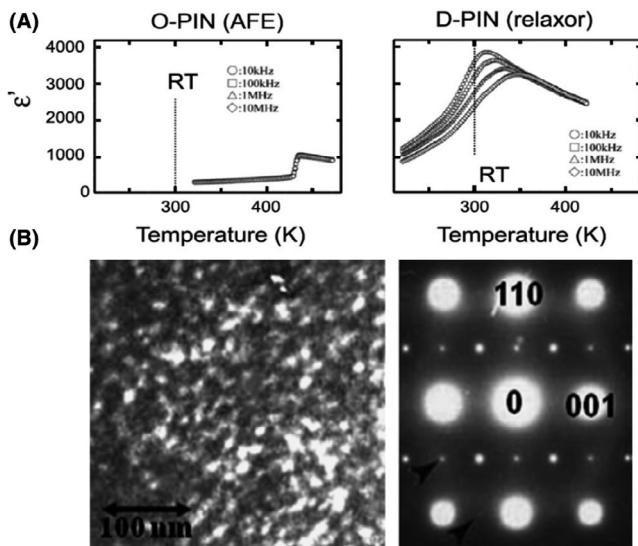


FIGURE 14 (A) Dielectric permittivity in the double perovskite Pb(In_{0.5}Nb_{0.5})O₃ with relaxor and AFE order (reproduced by permission from Ref. [121]). (B) Transmission electron microscopy images of Pb(In_{0.5}Nb_{0.5})O₃ with nanopolar ordering in the disordered materials as imaged through a dark-field image of a ½{110} superlattice, the [011] zone axis pattern shows the ½{hh0} dipole superlattice and the ½{hhh} B-site chemical ordering superlattice reflections (reproduced by permission from Ref. [122])

permittivity versus temperature for intermediate and long-range B-site ordered Pb(In_{0.5}Nb_{0.5})O₃; Figure 14B shows the dark-field imaging of the ½{hh0} superlattice reflections.¹²²

There are extensive studies in (Na_{0.5}Bi_{0.5})TiO₃ and its solid solutions, due to its potential interest as a lead-free piezoelectric, building from the initial work of Takenaka et al. The double hysteresis at higher temperatures in [(Na_{0.5}Bi_{0.5})_{1-x}Ba_x]TiO₃ solid solutions has variously been described as an AFE response or an ergodic relaxor behavior. Tan et al. combined the two models and proposed a “relaxor AFE” concept characterized by nano-antipolar regions.¹²³ However, with careful high resolution transmission electron microscopy (HRTEM) and Rietveld neutron powder analysis structural analysis, it is shown that there are inequivalent cation displacements that are coupled with the octahedral tilts. In fact, at temperatures between 593 to 813 K, the Na/Bi and Ti cations are displaced in opposite directions along the [001] axes, and these are coupled to an in-phase a⁰a⁺c⁺ octahedral tilt.^{123,124} The displacements are not equal and opposite, and therefore the material is not strictly an AFE. So, as pointed out above, even indications such as superlattices and double hysteresis loops are not necessarily definitive proof of an AFE.

5.1.1 | Crystal chemistry, solid solutions, and AFE stability in perovskites

The most extensive crystal chemical investigations of AFE have been in the perovskite crystal structure. Great insight into the trends of perovskites and their solid solutions have been guided by the Goldschmidt tolerance factor (*t*). It is based on a simple idea of the assumption of ionic packing in the perovskite ABX₃ compounds, The Goldschmidt tolerance factor is a dimensionless quantity that considers the geometric packing, where $t = (R_A + R_X) / \sqrt{2}(R_B + R_X)$, and where R_A, R_B, and R_X are the ionic radii of A, B, and X (for the appropriate coordinations). An extremely useful ionic radii base is supplied in the classic work of Shannon and Prewitt.¹²⁵ When *t* = 1, the geometry is consistent with an ideal cubic perovskite; as the *t* factor differs from 1, the perovskite structure distorts (often through tilt or FE distortions). At large deviations, the crystal structures change to structures such as ilmenite, FeTiO₃, *t* ~0.71, and hexagonal perovskite, *t* ~1.06. Goldschmidt, Megaw, Evans, Galasso, Fesenko, Isupov, and Navrotsky all noted the useful thermodynamic property trends correlating with tolerance factor, *t*, such as heat of formation, and antistortive versus ferrodistorptive phase stability trends within the perovskites.^{1,126-131} Later, others identified that many different electric property trends in perovskites correlate with the tolerance factor, including the temperature dependence of the permittivity in microwave dielectrics, morphotropic phase boundary temperatures, and of interest here, the stability of AFE over FE phases.^{132,133}

There are several examples of the use of the tolerance factor to stabilize an AFE phase in a perovskite, as detailed below. AFE in perovskites requires $t < 0.97$ ¹¹⁷:

$(Bi, Re)FeO_3$

Re is a rare-earth cation substitution in the end member $BiFeO_3$ is an extremely high-temperature FE material, with a T_c of $\sim 820^\circ\text{C}$ and a large distortion due to the large displacement of its cations relative to ideal positions (~ 0.66 Å for Bi and 0.26 Å for Fe at $\sim 100^\circ\text{C}$).¹³⁴ Given the high-temperature stability of FE phase, it is not intuitive that it can be transitioned into an AFE material. It does, however, have a tilt transition, and it also has a low tolerance factor, $t \sim 0.96$. The group of Takeuchi first reported the double loop in $(Bi_{1-x}Sm_x)FeO_3$ thin film beyond the MPB while attributed such AFE-type behavior to a low symmetry pseudo-orthorhombic phase.¹³⁵ Later, assisted by the electron-diffraction pattern, they revised that argument too, the $PbZrO_3$ -like symmetry is responsible for the AFE ordering, which was then reproduced in Gd- and Dy-doped BFO as well.^{136,137} Corresponding to different doping amount/tolerance factor, the PE symmetry is Pnma, the AFE phase is Pbam (isostructural with $PbZrO_3$), and at lower temperature, a FE R3c phase appears. Figure 15A shows the phase fields as a function of temperature and composition in rare-earth-doped $BiFeO_3$.¹³⁷

Reaney and co-workers investigated in detail the crystal chemistry of $(1-x)BiFeO_3 - xREFeO_3$.¹³⁸⁻¹⁴⁰ The $PbZrO_3$ (Pbam, $a^0b^-b^-$) structured AFE phase was stable for a certain

range of RE doping, below which an R3c ($a^-a^-a^-$) dominates and above which compounds adopted the classic orthoferite (Pnma) structure with an $a^-a^-c^+$ tilt system.¹⁴¹ Although the structural refinement in $(1-x)BiFeO_3 - xREFeO_3$ $0.13 < x < 0.22$ using XRD data is conducted with the same symmetry (Pbam, $\sqrt{2}a, 2\sqrt{2}a, 2a$) as the $PbZrO_3$ structure, electron diffraction reveals extra, weak $\frac{1}{4}\{h00\}$ superstructure reflections which suggest Pnma symmetry with a $\sqrt{2}a, 2\sqrt{2}a, 4a$ cell.¹³⁸

The phase transition from PE to FE/AFE is associated with a large volume change driven by an expansion along the b -axis. As a result, phase transitions in Nd-doped $BiFeO_3$ can be readily followed by DSC and dilatometry as well as in conventional permittivity temperature plots, Figure 15B.¹⁴²

The driving force for the formation of an AFE phase in RE-doped $BiFeO_3$ can be rationalized by comparing this system to the $PbZrO_3$ - $PbTiO_3$ phase diagram. In the PZT phase diagram, as the PZ end member is approached, the tolerance factor and average ionic polarizability decrease in an R3c/R3m phase field. Doping $BiFeO_3$ with Nd also decreases the tolerance factor and polarizability, leading to similar structural instabilities.^{139,140}

However, there are subtle differences in behavior between the onset of antiferroelectricity in the PZT phase diagram and that of Nd-doped $BiFeO_3$. In PZT, at room temperature, the amplitude of octahedral rotations increases in the R3c phase field as Zr concentration increases but then decreases to zero (R3m) as the PZ phase field is

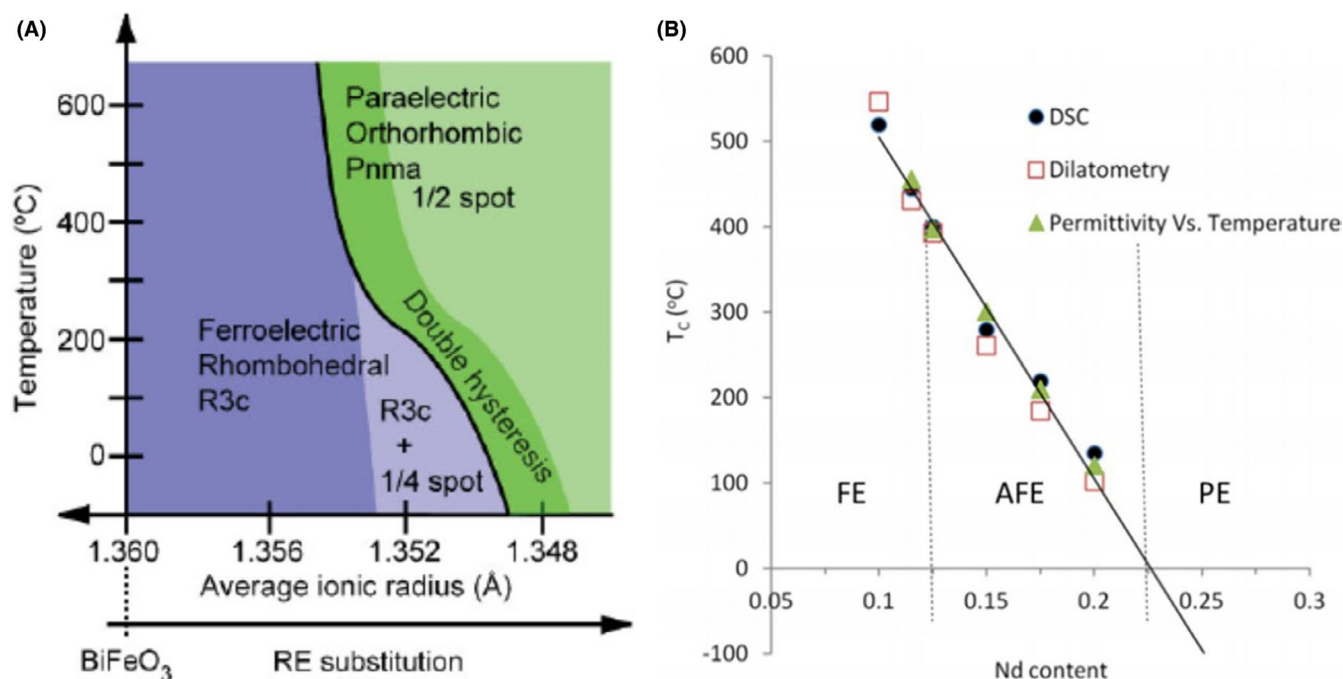


FIGURE 15 Effect of rare-earth doping on the crystallography of $BiFeO_3$. (A) The phase fields in RE-doped $BiFeO_3$ (reproduced by permission from Ref. [137]). (B) T_c vs. Nd content obtained from differential scanning calorimetry (DSC), dilatometry, and dielectric measurements. The phase boundaries are shown (reproduced by permission from Ref. [142]) [Color figure can be viewed at wileyonlinelibrary.com]

approached. This anomalous tilt behavior is not reproduced in the Nd-doped BiFeO₃ and suggests complex coupling between the Pb displacements and the octahedral rotations which force a gradual composition transformation, $a^-a^-a^-$ to $a^0a^0a^0$ to $a^0b^-b^-$ rather than the abrupt change in RE-doped BiFeO₃ from $a^-a^-a^-$ to $a^0b^-b^-$.^{138–140} Electron-diffraction patterns from compositions in between the $a^-a^-a^-$ and $a^0b^-b^-$ phase fields in PZT also exhibit superstructure reflections consistent with a cell doubling rather than quadrupling. The cell doubling was confirmed by Woodward et al.¹⁴³ these reflections violate the Weiss zone law in $\langle 110 \rangle$ zone axes for in phase tilting and, therefore, are more likely associated with cation rather than anion displacements. However, XRD studies of this region of the phase diagram have not, to date, unambiguously identified an intermediate structure of this nature.

One of the main problems associated with BiFeO₃ has been to control the electrical conductivity, generally considered to be p-type as a result of Bi-loss compensated by the oxidation of Fe³⁺ to Fe⁴⁺.¹⁴⁴ In principle, the substitution of a donor dopant such as Ti⁴⁺ on the B site should, therefore, significantly decrease conductivity. Kalantari et al. doped AFE-RE-doped BiFeO₃ with TiO₂ in an attempt to decrease the conductivity and establish whether a double AFE P-E loop could be obtained.¹⁴⁵ Although they were successful in decreasing conductivity by several orders of magnitude, only a linear dielectric P-E loop could be obtained, suggesting that AFE-FE switching in RE-doped BiFeO₃ may only be achieved at fields far greater than in PbZrO₃. However, Ti doping yielded unexpected phenomena within the matrix arising from an unusual ionic compensation mechanism such that $Ti_{Fe}^{\bullet} \equiv 1/3V_{Nd}'''$. As a result of this ionic compensation mechanism, Nd₂O₃ was expelled from solid solution at high temperature in the form of coherent nanorods a few unit cells wide.^{146,147} A number of other unusual planar defects were observed, some of which force a local FE rather than a AFE configuration.¹⁴⁸

NaNbO₃

The earliest experimental results on AFE in NaNbO₃ were reported by Nicholson and Cross.²² It proved to be very challenging to reproduce the results, most likely due to differences in impurity contents of the samples which led to small changes in the relative stability of AFE and FE phases. The structure of NaNbO₃ was also challenging to unravel; there is now a consensus that NaNbO₃ has two low-temperature phases of almost identical energetics, namely the **P** (AFE) and **Q** (FE) phases.¹¹⁵ Experimental studies are prone to uncertainty, as material impurities and/or non-stoichiometry can affect the relative stability of these two phases. Density functional theory (DFT) investigations verified the iso-energetics between the **P** and **Q** phases.¹⁴⁹ As NaNbO₃ had a tolerance factor t of $t \sim 0.967$, Guo et al. examined a wide

variety of solid solutions that would lower this tolerance factor, and in doing so, favor the **P** phase.¹¹⁸ Among the compositions that were experimentally determined to be AFE were $x\text{CaZrO}_3 - (1-x)\text{NaNbO}_3$ and $x\text{BiScO}_3 - (1-x)\text{NaNbO}_3$.^{117,150} TEM analysis of the domain configurations associated with the coexistence of **P** and **Q** phases confirmed that on lowering the tolerance factor, the **Q** phase systematically disappears, and a single **P** phase can be stabilized. Although not fully understood, INC phases also are involved as an intermediate in the electric-field-driven phase transitioning from AFE to FE.¹⁵¹ In NaNbO₃ stabilized with doping, the incommensurate phase in the **P** phase region can be inferred from the polarization current density and differential dielectric permittivity anomalies; it provides the bridge structure during the electric field-induced polarization reversal and AFE-to-FE transition in NaNbO₃ solid solutions.^{152,153}

AgNbO₃

The crystal structure of AgNbO₃ undergoes a series of polymorphic phase transformations as a function of temperature, from a high-temperature cubic prototype perovskite structure to progressively more complex tilt patterns, through two AFE orthorhombic phases, and finally to a FE phase. Octahedral tilt transitions are driven, in this material, by the fact that the Ag⁺ is too small for the 12-coordinated A-site; as a result, it displaces from the center of its coordination polyhedron, driving coupled puckering of the octahedral framework. The magnitude of the tilt angles and the phase transition temperatures can be modulated by applied strains.^{113,154–156}

In the AFE phases, tilting of the NbO₆ octahedra favors a locally ordered antipolar arrangement of the Nb displacements. These Nb displacements occur predominantly along the [110] direction of the prototype cubic unit cell, with a finite displacement in the crystallographic “c” direction of the unit cell. This is illustrated schematically in Figure 16, where the average and a potential local structure are shown.¹⁵⁷ However, it is important to note that Figure 16B is a simplification—the cancellation may not occur in the length scale of a single unit cell (as shown) but may occur elsewhere in the structure. In either case, the AFE behavior is presumably observed because a high enough electric field can induce a more ordered phase, where a net polarization is field-induced.

The general rationale adopted for the **M** phase transitions suggested that they occur as a result of a gradual increase in the amplitude of tilting on cooling from the **O-M3** transition which drives displacement of the cations from their average positions in the **M3** phase. The displacements occur initially such that they do not break the Pbcm symmetry (**M3-M2**), but finally a FE phase occurs (**M2-M1**) in which there are inequivalent cation antipolar displacements within the quadrupled tilted framework (Figure 17). This mechanism explains why the Curie maxima are so broad, since the cation

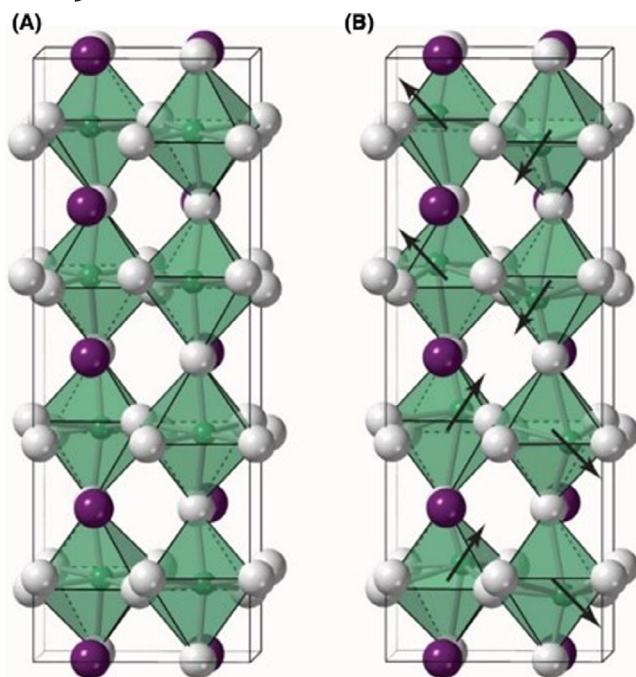


FIGURE 16 AgNbO_3 crystal structure at room temperature, after Levin et al.¹⁵⁷ (A) Shows the average structure, illustrating quadrupling along the c lattice parameter due to a complex tilt structure. In the so-called M phases, the Nb atoms displace in the octahedron over short length scales. (B) A schematic of one possible displacement pattern that would account for the observation of antiferroelectric hysteresis loops; the local polarization is shown with arrows. However, it is important to note that the best structure refinements available suggest that the displacements do not correlate over long length scales, and indeed may not appear in the same unit cell [Color figure can be viewed at wileyonlinelibrary.com]

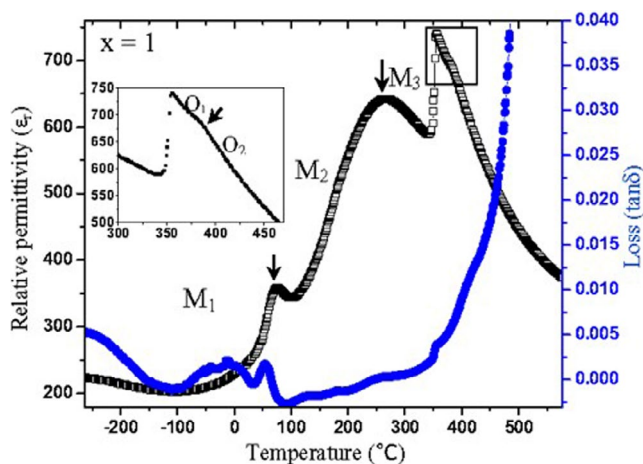


FIGURE 17 Relative permittivity (open circles) and loss tangent (filled circles) for AgNbO_3 showing some of the multiple phase transitions (reproduced by permission from Ref. [159]) [Color figure can be viewed at wileyonlinelibrary.com]

displacements which contribute to permittivity are coupled to the amplitude of octahedral rotation. It should be noted that the FE and AFE phases all refine well with $Pbcm$

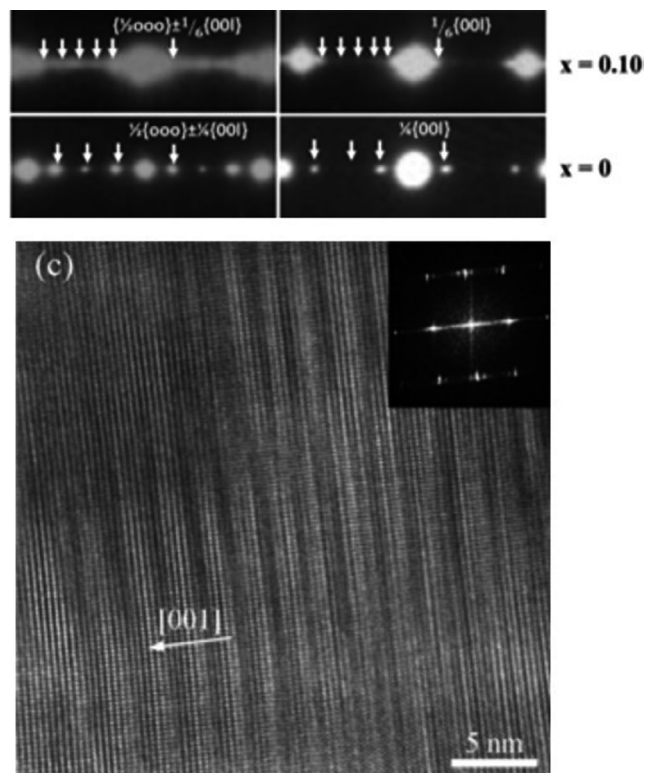


FIGURE 18 Systematic rows in $\langle 310 \rangle$ electron diffraction showing the formation of the $6\times$ supercell for 10% Li-doped AgNbO_3 and high-resolution image obtained parallel with $\langle 110 \rangle$ zone axis. Inset is the associated Fourier transform further illustrating the $1/6(001)$ spacing (reproduced by permission from Ref. [160])

symmetry, and it is only the appearance of weak polarization in the $M1$ phase that suggest that it is non-centrosymmetric ($Pmc2_1$).^{155–159}

Khan et al. studied the effect of Li doping on AgNbO_3 and observed a transformation from a $4\times$ to a $6\times$ cell in electron diffraction patterns at $\sim 10\%$ Li (Figure 18),¹⁶⁰ which was accompanied by a dramatic change in the Raman spectra. Rietveld refinement was not undertaken by these authors but the formation of a $6\times$ cell is analogous to the transitions observed in NaNbO_3 .

5.1.2 | Other AFE solid solutions

A typical phase diagram of the solid solution formed between an AFE end member and a FE end-member is the $(1-x)\text{PbZrO}_3 - x\text{PbTiO}_3$. The phase boundary between the AFE ($Pbam$) and FE ($R3c$) is at 95/5. Dopants such as La, Ca, Sn, Nb, etc. drive the material to a more diffuse phase transition. The resulting AFE structures are often INC and/or frustrated, inducing relaxor-like behavior.^{161–167} Figure 19 shows examples of phase boundary with La doping batched according to ionic compensation in the form $\text{Pb}_{1-3x/2}\text{La}_x(\text{Zr}_{1-y}\text{Ti}_y)\text{O}_3$.¹⁶⁸ Many of the AFE-FE materials within the perovskites

with PbTiO_3 have Morphotropic Phase Boundaries associated with enhanced piezoelectric properties; PYN-PT has noteworthy piezoelectric properties at its MPB. The AFE-FE MPB can be tuned or even created by applying an electric field and/or pressure, as shown in Figure 20.¹⁶⁸

6 | OTHER POSSIBLE CRYSTALLOGRAPHIC FAMILIES WITH ANTIFERROELECTRIC BEHAVIOR

6.1 | H-bonded ADP AFE

After the discovery of AFE in perovskites, the H-bonded KH_2PO_4 (KDP) family that had been found to host ferroelectricity was shown to have chemistries that host AFE, such as with ammonium di-hydrogen phosphate $(\text{NH}_4)\text{H}_2\text{PO}_4$ (ADP). The PO_4 tetrahedra are hydrogen bonded to other parts of the structure, and order-disorder in the position of the H-ion influences the dipoles within the tetrahedra. In the high-temperature phase, the H position is statistically averaged between the two oxygens in respective minima with no spatial repeating of the occupancies of those minima. In the case of FE such as KDP below T_c , there is a cooperative occupancy, and the PO_4 dipole moments are aligned in chains. The hydrogen bonds do not directly contribute to the spontaneous polarization, but the ordering of the H atoms acts as a trigger to the phase transition. In the case of ADP, the rotation of the $(\text{NH}_4)^+$ complexes drive adjacent chains with

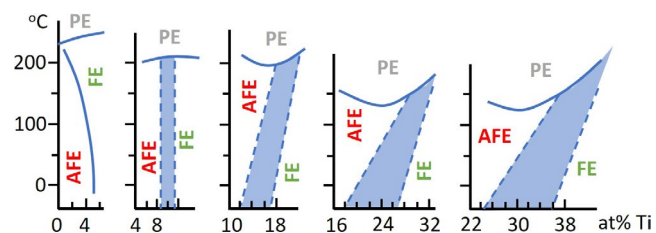
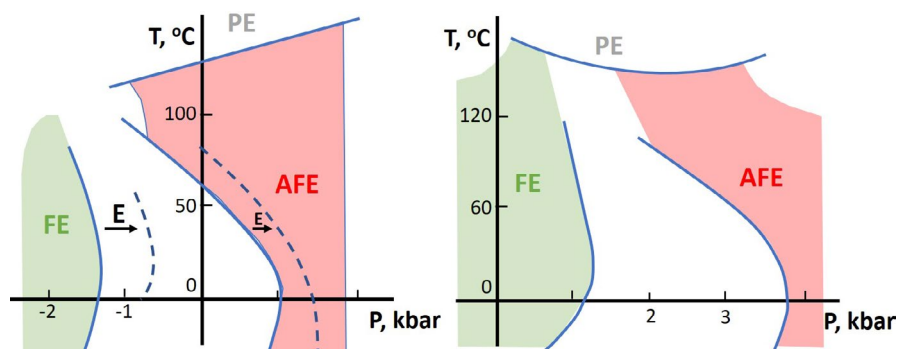


FIGURE 19 Phase boundaries as a function of Ti content in PZT doped with 0%–8% La (left to right) (replotted from Ref. [168]) [Color figure can be viewed at wileyonlinelibrary.com]

FIGURE 20 Pressure-temperature phase diagram for PLZT solid solution with 6% La, and Zr/Ti of 80/20 (left) and 65/35 (right), the E field applied is 500 V cm^{-1} (replotted from Ref. [168]) [Color figure can be viewed at wileyonlinelibrary.com]



antiparallel dipole alignments to form an AFE phase. Figure 21 show a comparison between the PE and AFE phases of ADP and the FE KDP.^{24,169–171}

Solid solutions have also been explored with ADP (AFE) as an end-member and FE compounds such as KDP and RDP, $\text{RbH}_2(\text{PO})_4$. In these order-disorder solid solutions, FE and AFE order compete, resulting, at intermediate compositions, in relaxor-like behavior typical of dipolar glasses.¹⁷² This arises because the solid solution induces frustration that limits the long-range ordering. The ordering is, therefore, short range and highly disordered, giving rise to glassy behavior and highly dispersive dielectric responses. In regions near the end members there are FE and AFE phase fields, and there is a systematic decrease of the phase transition temperature in solid solution with other end members. The region between these phase boundaries is characterized by a random local freezing-out of the dipoles owing to the frustration of the parallel and antipolar ordering (Figure 22).^{173–175}

6.2 | M-type hexaferrite structure and AFE

The M-type hexaferrites are based on the chemical formula $\text{MFe}_{12}\text{O}_{19}$ ($\text{M} = \text{Ba}, \text{Sr}$ or Pb); these are important ferrimagnetic oxides with high values of magneto-crystalline anisotropy and saturation magnetization. Recently, the M-type hexaferrites, such as $\text{PbFe}_{12}\text{O}_{19}$ and $\text{SrFe}_{12}\text{O}_{19}$, were reported to have large FE polarization and large magnetic properties coexisting at room temperature.^{176,177} $\text{La}_{0.2}\text{Sr}_{0.7}\text{Fe}_{12}\text{O}_{19}$ has been postulated to have an AFE phase. There are some anomalies in the loops that bear future exploration, such as the polarization saturation that is physically difficult to explain. Nonetheless, this is an interesting result, given the magnitude of the polarization reported. More work needs to be done on this family of materials to fully verify the potential AFE phase.

6.3 | HfO_2 - ZrO_2 thin films

There is double hysteresis observed in the new HfO_2 - ZrO_2 thin film systems, especially for the ZrO_2 rich

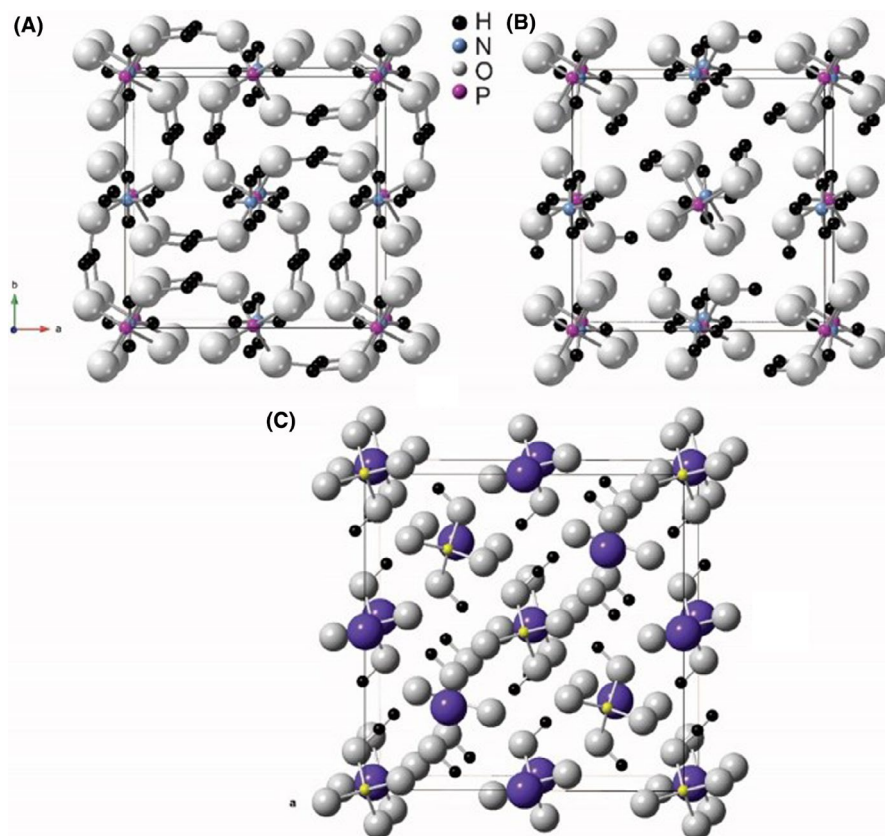


FIGURE 21 Crystal structures of $\text{NH}_4\text{H}_2\text{PO}_4$, after Fukami et al.¹⁷¹ in the (A) paraelectric phase at 152 K and (B) the antiferroelectric phase at 143 K. (C) Ferroelectric phase of $\text{K}_2\text{H}_2\text{PO}_4$ (K is the large dark sphere) [Color figure can be viewed at wileyonlinelibrary.com]

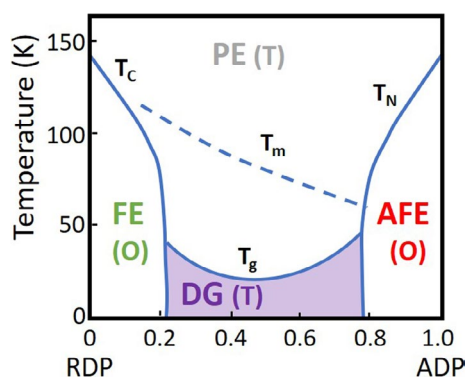


FIGURE 22 Show the binary solid solution between the FE KDP and the AFE ADP, the nature of the polarization changes to a dipolar glass in the central compositions (replotted from Ref. [172]) [Color figure can be viewed at wileyonlinelibrary.com]

compositions.¹⁷⁸ At this time there are no additional experiments to point to a true AFE behavior, as opposed to an aging or domain pinning effect. However, a detailed DFT calculation has shown that there are optical phonon instabilities in the cubic phase at the Brillouin zone edges, and these also are coupled to a zone center mode.¹⁷⁹ So it is quite possible that there is either an AFE structure or INC structure in these new systems, but the field awaits the important structure details in this interesting FE binary system.

6.4 | Alkali earth sulfoaluminate structure and AFE

Calcium sulfoaluminate is of interest for cements, as well as its luminescent properties. The structure is built up of $[\text{AlO}_2]_{12}^-$ anionic framework, and the spaces between are filled by M^{2+} cations and X^{2-} anions. The $[\text{AlO}_2]_{12}^-$ framework of corner-shared AlO_4 tetrahedra can undergo a variety of distortion modes. Recently the $(\text{Ca}_{1-x}\text{Sr}_x)_8[\text{AlO}_2]_{12}(\text{SO}_4)_2$ with $x = 0.8-1.00$ has dielectric properties that has been proposed to be due to AFE and relaxor dielectric properties. The basic crystal structure is shown in Figure 23.¹⁸⁰ The high-temperature phase is $\text{Im}\bar{3}\text{m}$. On cooling, the material undergoes a series of transitions from $\text{Im}\bar{3}\text{m} \rightarrow \bar{\text{I}}\bar{4}3\text{m} \rightarrow \text{P}\bar{4}\text{c}2$. At lower temperatures, an AFE phase is speculated to occur for $x > 0.95$; for higher Ca-doping, the $\text{P}\bar{4}\text{c}2$ phase field is lost. In this case, the transition is believed to be to a low-temperature relaxor AFE, from the cubic $\bar{\text{I}}\bar{4}3\text{m}$. Further work is required to fully confirm these materials to be members of the AFE family.

6.5 | Ruddlesden–Popper structures

Recently a new Ruddlesden–Popper compound, $\text{Sr}_3\text{Zr}_2\text{O}_7$, was reported as having a first-order FE to PE phase

FIGURE 23 (A) Temperature-dependent dielectric constant in $(\text{Ca}_{1-x}\text{Sr}_x)_8[\text{AlO}_2]_{12}(\text{SO}_4)_2$. (B) Phase diagram of $(\text{Ca}_{1-x}\text{Sr}_x)_8[\text{AlO}_2]_{12}(\text{SO}_4)_2$ (reproduced by permission from Ref. [180]) [Color figure can be viewed at wileyonlinelibrary.com]

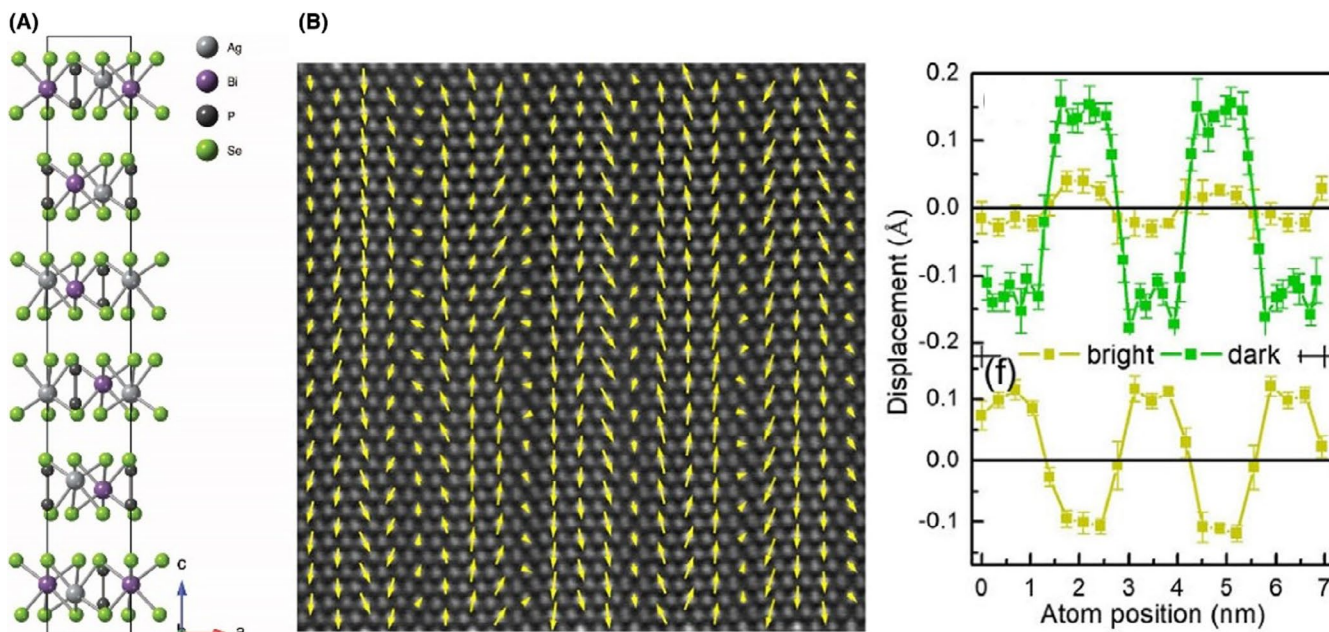
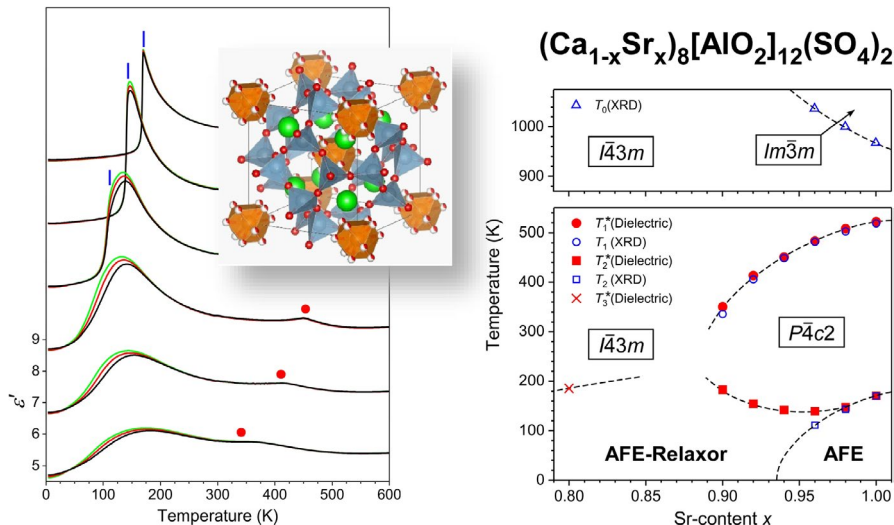


FIGURE 24 (A) Crystal structure of $\text{CuBiP}_2\text{Se}_6$ at room temperature, after Gave et al. The positions of the Ag and the Bi show an antiferroelectric-like arrangement.¹⁸³ (B) ADF-STEM mapping of the dipoles in $\beta\text{-In}_2\text{Se}_3$ and the measured atomic displacements (reproduced by permission from Ref. [185]) [Color figure can be viewed at wileyonlinelibrary.com]

transition.¹⁸¹ The tilt transitions drive this system to a room temperature FE. There is an unusual sequence of coupled and uncoupled octahedral rotation and tilt transitions making this a hybrid improper FE. Density Functional Theory (DFT) calculations and structural analysis successfully explain the phase transitions. In addition to the FE and tilt transitions, it is noteworthy that there is an antipolar Pnab high-temperature phase that is classed as a hybrid improper AFE. At this time, the DFT calculations are not experimentally verified, but they point to a broader concept of tilt and soft mode instabilities, especially in materials with small chemical driving forces for polar modes.

6.6 | 2-D antiferroelectrics

Two-dimensional materials have emerged as a new family of optoelectronic materials. Depending upon the number of layers and the composition, a wide variety of properties from superconductors, metals, semiconductors, and insulators have been reported.¹⁸² More recently, there have been a limited number of reports that 2-D materials such as $\text{AgBiP}_2\text{Se}_6$, CuInP_2S_6 , and $\text{CuBiP}_2\text{Se}_6$ can have FE, ferroelectric, or AFE phases.^{183,184} As shown in Figure 24A, in $\text{AgBiP}_2\text{Se}_6$, the chalcogenide framework has octahedral voids filled by Ag (Bi) and P-P pairs. The bulk crystals are

made from stacks of these layers. It is apparent that the Ag^+ and Bi^{3+} positions show AFE-like ordering. Recently, Xu et al. mapped out the in-plane antiparallel dipole arrangement with the modulation wavelength of $8d_{1\bar{1}00}$ in the single-layer $\beta\text{-In}_2\text{Se}_3$ (Figure 24B). The domain boundary is observed at both nano- and micron-scale.¹⁸⁵ Unfortunately, perhaps due to the relatively low bandgap of the compounds, clear AFE double hysteresis loops have not been reported. Van der Waals interactions bond the adjacent layers, and the weakness of the Van der Waal bonds allows for the material to be exfoliated into 2-D layers. A detailed DFT investigation points to the balance of ionic and Van der Waal interactions that can control the FE and/or the AFE ordering of these materials.¹⁸²

6.7 | Antiferroelectric liquid crystals

Liquid crystals are between two states of matter, that is, liquids and solid crystalline phases. Meyer (1975) discovered FEs in a tilted chiral smectic C^* (SmC^*) liquid crystalline phase.¹⁸⁶ These materials had very fast electrooptic switching, as shown by Clark and Lagerwall (1980),¹⁸⁷ that at that time was highly appealing for computer monitors. This, in turn, applied a technological pull to explore more chemistries that could form tilted SmC^* materials. SmC^* chiral molecules

naturally are non-centrosymmetric. In the tilted chiral form, molecules are arranged with an orientational order in smectic layers, and in each layer, there can be a dipole-dipole ordering that overrides the thermal disordering of the PE phase.¹⁸⁸ The low-temperature phase then has several cooperative forms ranging from parallel or antiparallel dipoles. So, this not only led to the discovery of liquid crystal FE, but also to ferroelectric, incommensurate, and AFEs. The AFE SmC_A^* phase was discovered by Chandani (1989).¹⁸⁹ Figure 25 shows the spontaneous polarization pointing upward and downward in alternative layers in SmC_A^* phase and the double loop measured from 4'-Octyloxy-biphenyl-4-carboxylic acid 4-(1-methyl-heptyloxycarbonyl)-phenyl ester (MHPOBC).¹⁹⁰ There are several AFE variants classified into four major groups; alternative layers with antipolar orthogonal ordering SmA_p , tilted polar case that can be synclinal or anticlinal leaning, and combinations of the tilting and leaning alternatives, sometimes called double tilted or general tilted.

7 | HIERARCHICAL DOMAIN STRUCTURES AND SWITCHING IN ANTIFERROELECTRIC MATERIALS

For either order-disorder or displacive PE-AFE phase transitions, there is a crystallographic symmetry change. In general, if the high temperature or PE point group symmetry is called G , then the symmetry of the lower temperature phase, F , is a subgroup of G . In this case, the number of domain states can be determined from the ratio of the order of point group G , divided by the order of point group, F .^{191,192} In the case of antidistortive phase transitions, because of the superlattice structure, the translational symmetry, and the space group need to be considered. The number of formula units per unit cell in both the PE and AFE phases are Z_G and Z_{AFE} . So, for the case of AFE, the number of domain states is then given by:¹⁹¹

$$q = \frac{|G| Z_G}{|F| Z_{\text{AFE}}}$$

When there are more than two domain states in the absence of external fields (such a magnetic, electric, and stress), and these domains can be moved by external fields, either singularly or in combination, the material is ferroic.

The domains that then develop in the crystals and crystallites form complex configurations, with domain walls that separate the domains. The domain state is a consequence of energy minimization, in which the energy cost of the domain walls is balanced by the energy gain associated with the spontaneous strain elastic energy and/or the electrostatic energy that corresponds to the polarization divergence has to be minimized. There are different

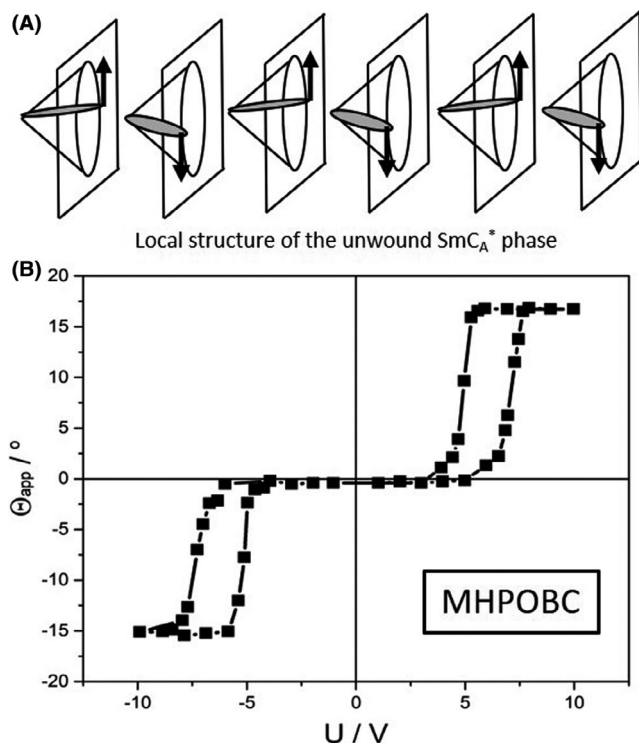


FIGURE 25 (A) Schematic illustration of the structure of an antiferroelectric smectic liquid crystal (without the helical superstructure); (B) corresponding double hysteresis loop (replotted from Ref. [190])

types of domain walls that can be found in AFE and related materials.^{193–195}

7.1 | Ferroelastic domain walls

Ferroelastic domain pairs meet at domain walls which exhibit mechanical compatibility—this limits the orientation of the habit planes to ensure that domain walls are stress-free; these are sometimes called permissible walls. The mathematical description for these types of ferroelastic walls can be found in classic papers by Fousek and Janovec,¹⁹⁶ and Sapriel.¹⁹⁷ Those papers classify the strain and symmetry restrictions for the twinning of the domains. In orthorhombic crystals, the permissible walls are {001} for 90° domain walls; {110} for 60° domain walls; {112} for 120° domain walls. The presence of multiple walls in one grain can result in rather complex domain morphologies. In incommensurate AFE, the overall domain morphology always looks like a “checkerboard”.¹⁹⁸ It should be noted that the aforementioned are the walls conforming to the symmetry restrictions. In real AFEs, Zig-Zag walls are allowed,¹⁹⁹ and indeed are sometimes necessary, due to two reasons. First, the minimum elastic/electrostatic energy can be satisfied not only by the “permissible walls” in AFE where an individual domain has essentially no net polarization. For instance, in Figure 26, there is a {110} wall that separates two 90° domains is quite common in pure PbZrO₃.²⁰⁰ Second, an antiphase boundary will break the “head-to-tail” configuration on the domain wall, locally. Under such circumstances, the Zig-Zag wall, namely the insertion of {110} sections to a {001} wall, is necessary to compensate for the dipolar mismatch.²⁰⁰

On cooling from the PE-AFE, the transformation for NaNbO₃ and PbZrO₃ would be from m3m-*mmm*; on application of an electric field large enough to induce switching, the AFE domains switch to FE (mm²). The basic switching

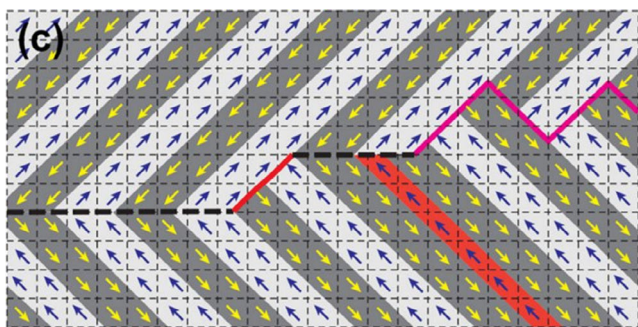


FIGURE 26 Schematic drawing of a real domain wall in PbZrO₃ adjacent to an APB (red stripe). The black dashed line is a normal {001} wall, whereas the highlighted ones are the {110} sections (reproduced by permission from Ref. [200]) [Color figure can be viewed at wileyonlinelibrary.com]

was through two domain configurations in the FE states, with charged 60° and neutral walls. The Zig-Zag walls, under this circumstance, can also minimize the divergence in the polarization. Transmission electron microscopy is a very powerful tool to quantify the domain orientations, and diffraction contrast methods in bright field and dark can be used to determine the walls and the orientational relations between each domain as modeled by Amenickx and co-workers.^{201–203} Also, electron holography and differential phase imaging allows for the atomic strain and polarizations to be determined.^{204–209}

7.2 | Antiphase boundaries

Antiphase boundaries are linked to cases where the unit cell of the ferroic phase contains multiple unit cells of the prototype phase, as is the case with antidistortive phase transitions, such as antiparallel dipole alignment in an AFE, or octahedral tilt transitions. Antiphase boundaries appear when two domains come together and the boundary that separates then has an out of sequence ordering. These types of boundaries are also non-ferroelastic as there are no strain differences between adjacent regions. An example is an APB in PbHfO₃ is shown in Figure 27.²¹⁰ It can be clearly seen that the APB disrupts the local periodicity. Consequently, the APB region can display finite polarization. The order parameters in the two domains separated by APB differ by a phase shift of π .²¹¹ Thus, antiphase boundaries in AFE can also be called polar translational boundaries. Under diffraction contrast in TEM, they appear as straight lines. Combined with the ferroelastic walls, most AFE grains display a hierarchical domain structure. It should be noted that antiphase boundaries with different translational vectors exhibit different polar states,²¹² Figure 27B just illustrates one of the simplest cases. Also, compositional and mechanical tuning seem to favor the formation of certain types of antiphase boundaries.²¹³

7.3 | Incommensurate modulation

In order to increase the dielectric energy storage density, one current trend in AFE research is to increase the breakdown strength and E_F . This contrasts with actuator applications, in which E_F and hysteresis are both intentionally reduced. Reductions in E_F can be achieved, for example, in PbZrO₃ doped with Ti, as the Ti stabilizes FE over AFE ordering. Unfortunately, the doping range is rather narrow (AFE/FE MPB at PZT95/5). To broaden the range of achievable properties, co-doping is often utilized, with La on the A site (PLZT) and Sn or Nb on the B-site (PNZST). It is speculated that the reduced E_F in these materials has its origin in

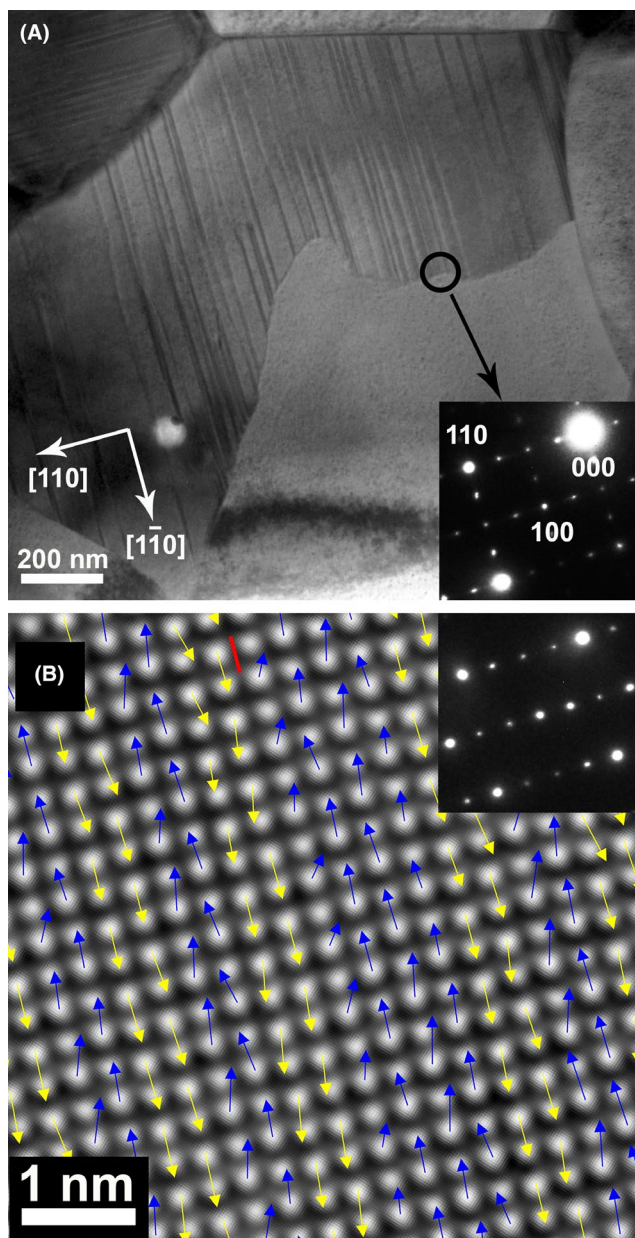


FIGURE 27 (A) Hierarchical domain structure in PbHfO_3 ; (B) HRSTEM mapping of an APB from the upper ferroelastic domain. The blue and yellow arrows correspond to the local polarization—an alternating pattern of two up/two down is observed on either side of the APB. The region between the dashed red lines is the APB in which the polarization periodicity is interrupted. (reproduced by permission from Ref. [210]) [Color figure can be viewed at wileyonlinelibrary.com]

incommensurate (INC) modulation. The room-temperature ternary phase diagram and the composition-temperature phase diagram for PNZST are shown in Figure 28,^{214,215} from which two important features of INC can be assessed. First, INC PbZrO_3 is pseudo-tetragonal, as opposed to orthorhombic. Second, the temperature at which the FE phase forms is below that for AFE if incommensurate, but above it for commensurate AFE (e.g., pure or Ba-doped PbZrO_3). Such a change in the phase sequence has a great impact on pyroelectric/ECEs. The multicell cubic phase was proposed

because a strong deviation from Curie–Weiss behavior is observed above T_{max} , which resembles relaxor FE.²¹⁶ Selected area electron diffraction also proves that the $1/x\{110\}$ superlattice spots persist to the higher temperatures.

As described earlier, INC AFE deviates from the commensurate AFE in that the modulation wavelength (periodicity) is no longer $4d_{110}$ (in PbZrO_3 -based materials) but becomes irregular and can vary with temperature and composition. As can be seen from Figure 28B, in PNZST, the INC phase occurs at an intermediate Ti concentration, suggesting that it might be essentially a bridging state from AFE to FE, where the interactions favoring the two structures are competing. Indeed, the modulation wavelength increases with Ti addition, as manifested by the superlattice spot approaching the fundamental spots.²¹⁵ Similarly, upon cooling, the wavelength should keep decreasing until the incommensurate-commensurate phase transition occurs at the lock-in temperature. But the INC wavelength is always temperature independent before being “locked-in”.²¹⁷

For displacive-type incommensurate modulations, the perturbation can occur not only in the phase (periodicity), but also in the amplitude. So, it raises the question, do the dipoles in INC AFE still follow the stringently antiparallel arrangement? In PLZT, MacLaren discovered that the dipoles are not equal in magnitude but form a sinusoid (Figure 29).²¹⁸ Chen confirmed the sinusoidal dipole wave in PNZST, but also observed that the atomic displacements have components along two orthogonal $\langle 110 \rangle$ directions.²¹⁹ More strikingly, they showed that polarization may not be fully compensated in INC AFE. This result is qualitatively consistent with Tan's HRTEM characterization in the same composition, which revealed the unbalanced cation displacements in the context of hierarchical domain structures.²²⁰ Very recently, Fu et al. also verified the “FE-like” dipole arrangement in PLZT using annular bright-field scanning transmission electron microscopy (STEM).²²¹

7.4 | Domain switching

Domain switching and phase switching in AFE materials requires nucleation of the FE phase within the AFE, with subsequent domain wall movement. The nucleation process will be heterogeneous, and therefore defects and AFE boundaries aid the nucleation of the FE phase, and after the nucleation the phase will grow at the expense of the AFE ordering in the AFE domain. Defects such as dislocations have a strain gradient that can favor FE nucleation in an AFE; also, antiphase boundaries in a commensurate phase or the domain boundaries in an incommensurate phase can have sequences of dipoles that are locally parallel over a small distance that would also enhance the probability of a stable FE nuclei. There are a great number of details that have not been completely resolved with the switching in a double hysteresis loop. These processes may also involve INC

FIGURE 28 (A) Ternary phase diagram in PNZST (reproduced by permission from Ref. [214]); (B) Phase diagram of $\text{Pb}_{0.99}\text{Nb}_{0.02}(\text{Zr}_{0.5}\text{Sn}_{0.45})_{1-y}\text{Ti}_y\text{O}_3$ (reproduced by permission from Ref. [215])

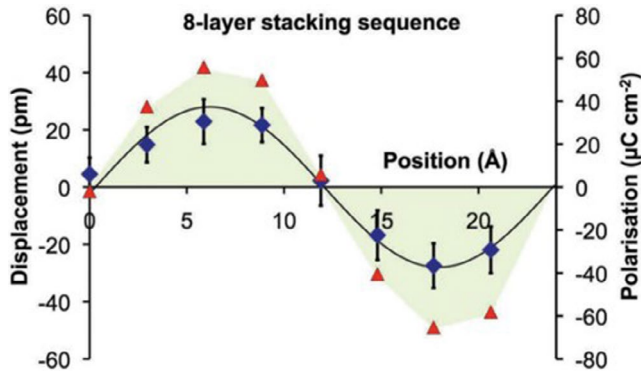
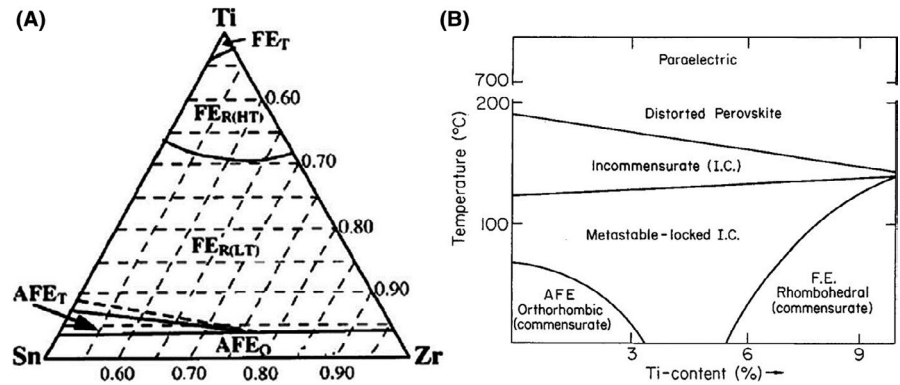


FIGURE 29 Atomic displacements and calculated polarization as a function of position in incommensurate PLZT (reproduced by permission from Ref. [218]) [Color figure can be viewed at wileyonlinelibrary.com]

intermediate phases, and large local strain gradients as the volume changes occur between the AFE and FE unit cells. The major hindrance to studying these issues is that the AFE to FE phase transition is very rapid at E_F , such that the nucleation process or any intermediate stage is difficult to catch. Generally, successful in situ studies rely on non-uniform stimuli. For instance, in-situ biasing TEM using the E field applied through a sharp indenter has enabled studies of the nucleation and the domain wall motion in FE thin films.²²² Recently, e-beam illumination, instead of an electric field, has been utilized to trigger the AFE to FE transition in a PbZrO_3 crystal.²²³ An intermediate FE phase with cycloidal polarization order was demonstrated to exist transiently during the AFE—FE transformation. In addition, the FE/AFE phase boundary or the interphase interface are of particular interest for clear observations of the dynamics, on both global and local scale.^{224,225}

8 | ANTIFERROELECTRIC APPLICATIONS

8.1 | Pulse power capacitors

AFEs have, since the 1960s, been a part of the defense industry and are used for nuclear weapon triggers for fission,

operating in a single-shot use. These must be processed with extremely high levels of accuracy and control in terms of the electrical and mechanical performance.²²⁶ The compositions of choice are based on the PZT 95/5 AFE. Pulse power is now becoming important in a number of other applications in defense, mining, renewable energy, and medical industries. Some include mine detection, testing platforms for lightning and electromagnetic pulse simulators, electromagnetic launchers, mineral and oil exploration, blasting operations at mines and quarries, and neutron generator power systems. All these power supplies necessitate high-energy density to permit miniaturization and are designed to undergo complete depolarization from a poled FE state to the AFE under an explosively triggered compressive shockwave. Specifically, the shock pressure compression can release the bound electric charges of poled FE ceramics within a short period of time (~microseconds), thereby generating a sharp current/voltage pulse with megawatts of electrical power.²²⁷ This charge then is supplied on the output terminals in the form of a high-energy electrical pulse; the basic device structure is shown in Figure 30.^{228,229} Traditionally, the focus on these AFE materials has been around PZT 95/5,⁴⁵ more recently lead-free alternatives have been reported based on $\text{AgNbO}_3\text{-KNbO}_3$ 94/6 solid solutions. Figure 31 shows the discharge characteristics for a lead-free AFE material.²³⁰ The energy densities in the lead-free systems are greater than the PZT ceramics. However, no efforts have been made to commercialize, such AFE, at this time. With such preliminary property observations as all these compositions are of interest to develop new classes of electromagnetic pulse weaponry that can disrupt or destroy communications, guidance systems, and weapons. These not only need to consider the high-energy densities but also high yield performance that will depend on many processing details including high levels of chemical homogeneity, stoichiometric, and microstructural control.

8.2 | AFE multilayer ceramic capacitors

Multilayer ceramic capacitors (MLCC) are fabricated by tape-casting and screening printing metal electrodes; these

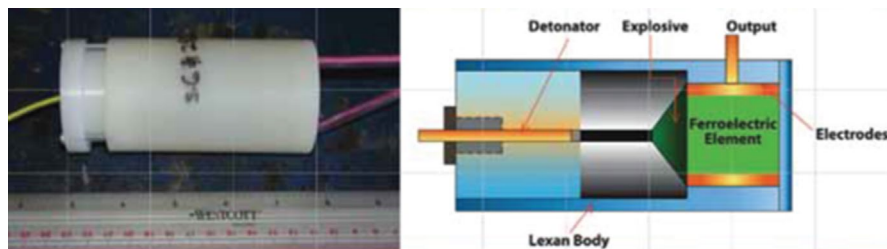


FIGURE 30 Example of an antiferroelectric capacitor for a detonator, along with a schematic²²⁹ [Color figure can be viewed at wileyonlinelibrary.com]

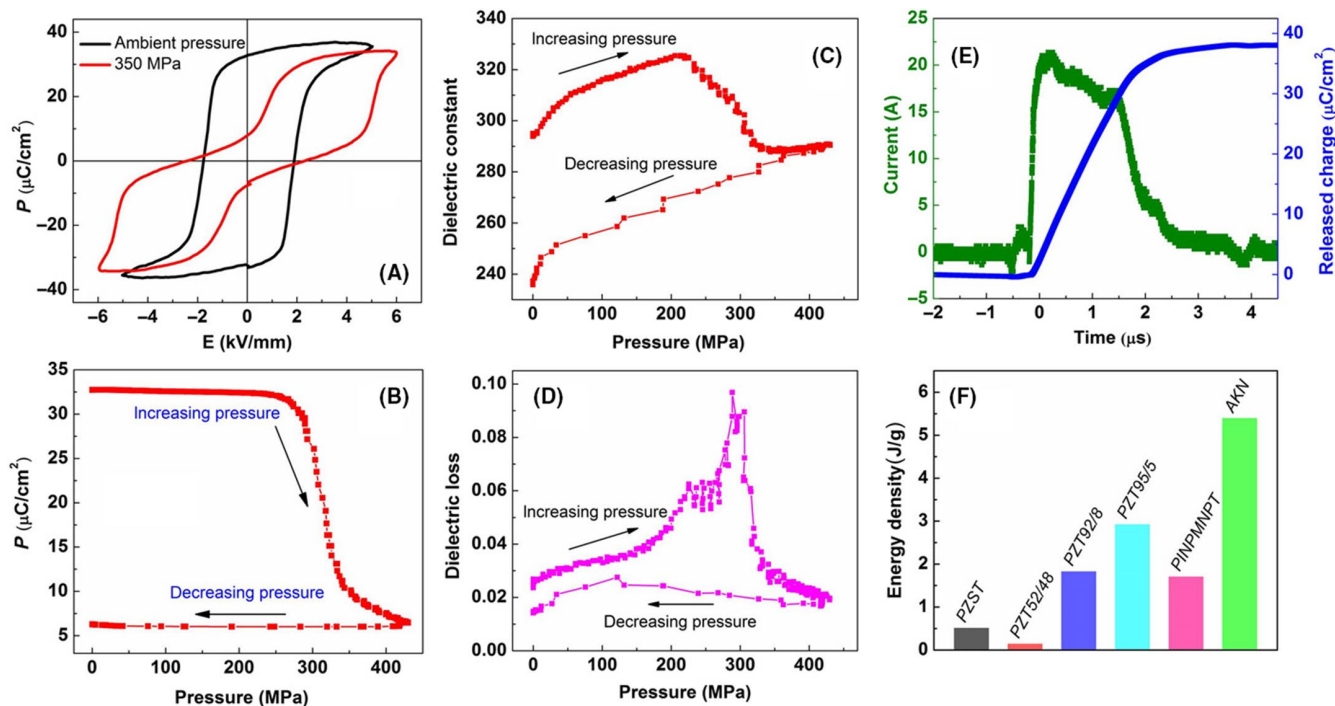


FIGURE 31 Explosive energy conversion performance in $(\text{Ag}, \text{Na})\text{NbO}_3$ (reproduced by permission from Ref. [230]). [Color figure can be viewed at wileyonlinelibrary.com]

dielectric layers and printed electrodes are laminated and stacked. The ability to form and control the dimensions of these layers requires the mixing of organic dispersants, binders, and solvents with the powders to form the slurries for the tape casting and pastes for the electrodes. After stacking, individual capacitors are cut out, and the organics are removed via a de-binding process. After this, the components are co-sintered into dense multilayers. Subsequently, a termination step interconnects the interdigitated electrodes on each side of the component to form parallel interconnections between the dielectric layers. A more detailed introduction to MLCCs can be found in several reviews.^{231,232} The basic structure of an MLCC device is shown schematically in Figure 32. The most widely used dielectrics are based on compositionally modified FE BaTiO_3 ; the second most important MLCC dielectric is a linear dielectric based on CaZrO_3 . However, there are a small number of AFE materials being considered owing to their high-voltage high-permittivity performance. The electrodes can be based on precious metal chemistries, such as Pt, Pd, Ag-Pd, and Ag; these can all be sintered in

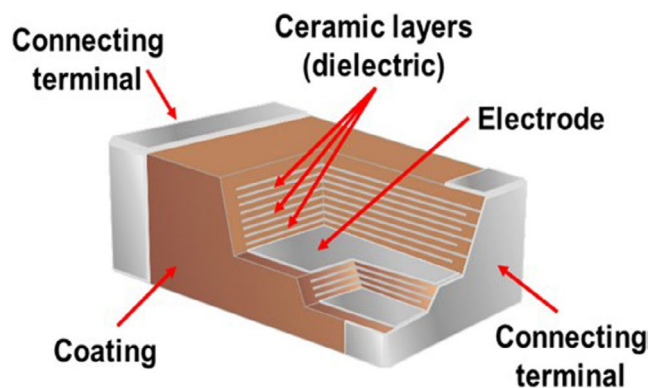


FIGURE 32 Cross section of a multilayer ceramic capacitor [Color figure can be viewed at wileyonlinelibrary.com]

air atmospheres, but with the exception of Ag, the electrodes in this family are expensive. Base metal or valve metal electrodes, such as Ni and Cu, mandate more complicated processing in order to avoid either oxidation of the metals or

reduction of the dielectric materials. Controlling the partial pressures of oxygen to balance the redox reactions is important, among many other detailed considerations. However, there is a substantial advantage in cost savings.

The capacitance of the devices is given by the following equation:

$$C = An\epsilon_r\epsilon_0/t,$$

where A is the effective overlap area, n is the number of interconnected layers, ϵ_r is the relative permittivity, ϵ_0 is the permittivity of free space, and t is the dielectric layer thickness.

Capacitor dielectrics are designed to co-optimize many physical properties, but the most important of these are the capacitance values, dielectric loss, resistance, operating voltage range, operational temperature range, and the physical dimensions (or case size) of the device. At high voltages, FE dielectrics have a decreasing permittivity, and linear dielectrics have a low permittivity, but AFEs have permittivity that increases with increasing voltage. Figure 33 shows the different field behavior of these different types of dielectric material: (a) Linear, (b) FE, and (c) AFE with respect to polarization and electric field E and the dielectric permittivity versus E .

The recoverable electrostatic energy density W_E is given by the shaded areas in Figure 33; it is apparent that AFEs have relatively high-energy density. To facilitate charging and discharging of the AFE, a base material, such as PZT 95/5, is modified with additives, such as La and Ca, to minimize the hysteresis and suppress large volume changes that would create high field losses and induce microcracking. So often, the structure is INC for the best performing AFE compositions.^{233–243} Chen et al. have shown that the dynamic

switching of the AFE double hysteresis loops of a given AFE follows a scaling law with the energy density having dependence on variables such as the amplitude of applied field and its frequency.^{244,245}

Temperature stable AgNbO_3 -based ceramics are usually fabricated by doping with Ta on the B site, which decreases the temperature of the **M** phase transitions.¹⁵⁹ A heterogeneous distribution of Ta and Nb within the ceramic can then be utilized to suppress the temperature dependence of permittivity.²⁴⁶ $\text{Ag}(\text{Nb}, \text{Ta})\text{O}_3$ is, therefore, one of the highest permittivity, temperature stable ceramics and offers unique properties amongst dielectric ceramics between COG and X7R designations.²⁴⁷

Recently there has been a resurgence of interest in AgNbO_3 as a high-energy density capacitor material.^{248,249} The recoverable energy density (W_{rec}) is optimized in AgNbO_3 through dopant strategies that delay the onset of the field-induced transition to higher values of E and which also facilitate a slimmer field induced region of the P-E hysteresis loop, as shown in Figure 34. Optimized compositions are typically RE doped on the A site, which gives rise to V'_{Ag} and are Ta doped on the B site. $W_{\text{rec}} \sim 6.5 \text{ J cm}^{-3}$ has been achieved with conversion efficiencies around 70%.²⁵⁰ For AgNbO_3 , the opening of the P-E hysteresis loop is not concomitant with a change in crystal class as observed in PbZrO_3 . Rather, the field-induced phase retains the same crystal class and quadrupling as the AFE phase but exhibits inequivalent antiparallel displacements of the cations and thus conforms to a field-induced ferrielectric phase.

In addition, lead-free AFE dielectrics have been made with the NaNbO_3 - NaTaO_3 systems. In this case, there is an interesting core shell microstructural development with the core being AFE, and the shell being INC; this limits the voltage saturation and provides high-temperature dielectric

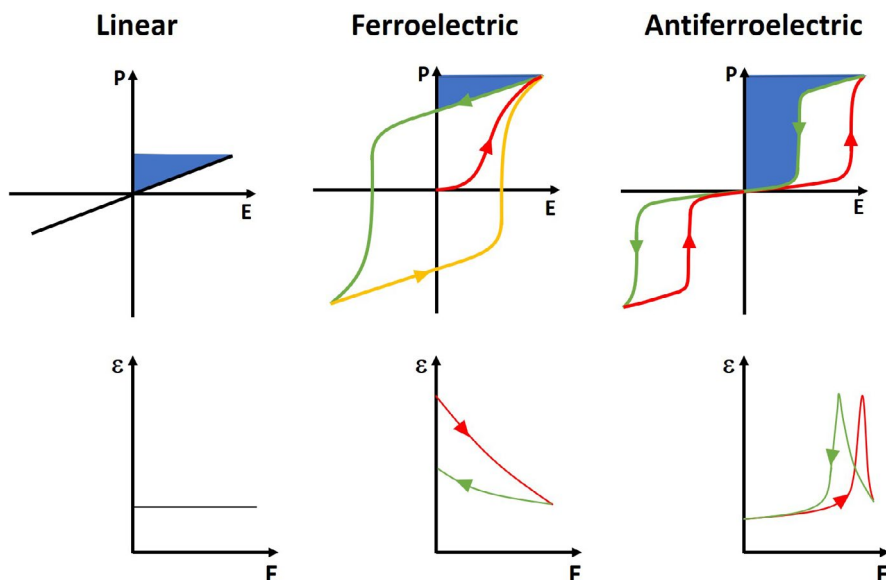


FIGURE 33 Schematics of polarization and permittivity as a function of DC bias field for linear dielectrics, ferroelectrics, and antiferroelectrics. The blue shaded areas correspond to the recoverable energy density [Color figure can be viewed at wileyonlinelibrary.com]

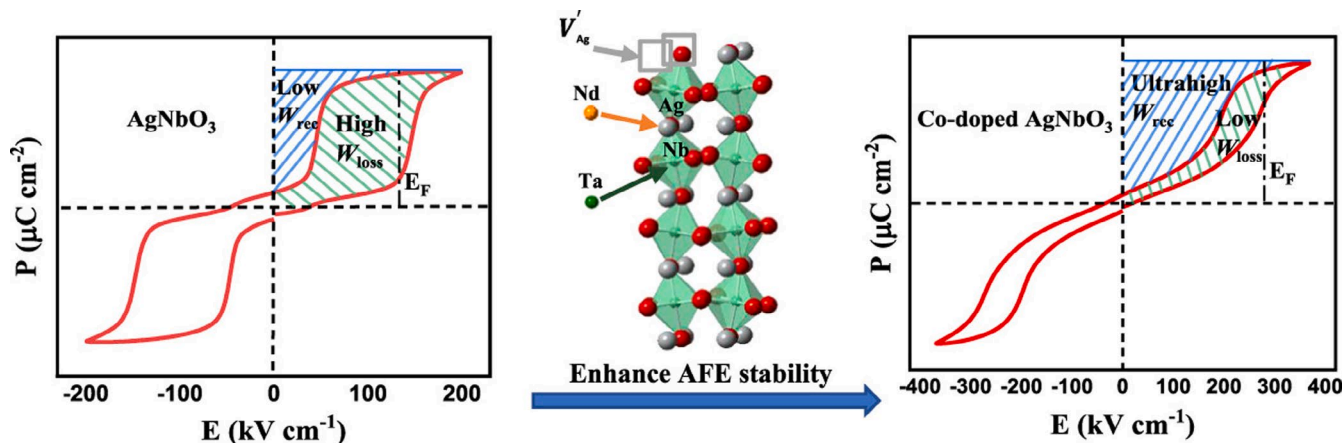


FIGURE 34 Schematic illustrating how the energy density is optimized in a RE, Ta-doped AgNbO_3 (reproduced by permission from Ref. [250]) [Color figure can be viewed at wileyonlinelibrary.com]

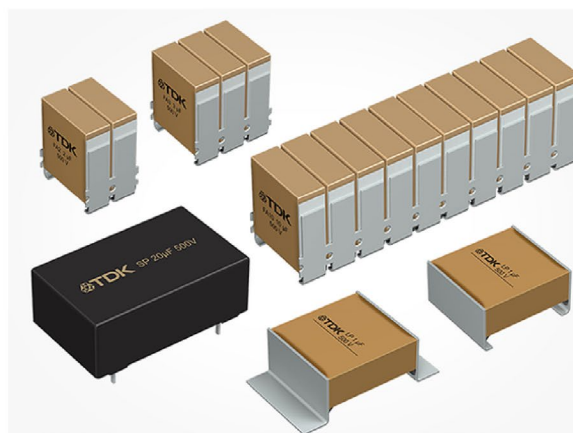
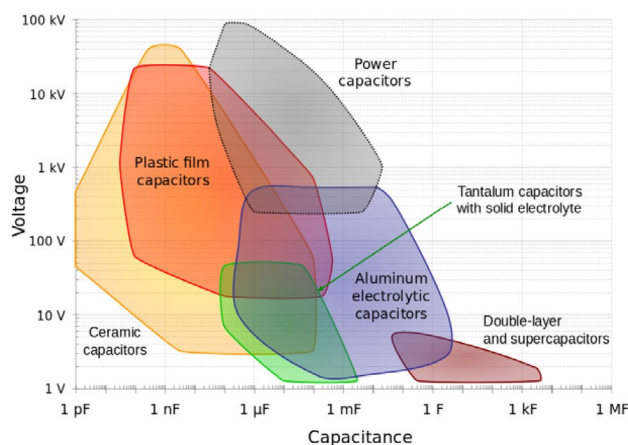


FIGURE 35 (Left) Comparison of antiferroelectric-based capacitors with other technologies. (Right) picture of a commercial AFE capacitor from TDK (reproduced by permission from Ref. [252] and Courtesy of TDK) [Color figure can be viewed at wileyonlinelibrary.com]

materials. At this time, there has been no commercialization of the lead-free AFE's.²⁵¹

Some of the specific applications for AFE MLCC's include:

8.2.1 | DC link capacitors for power electronics

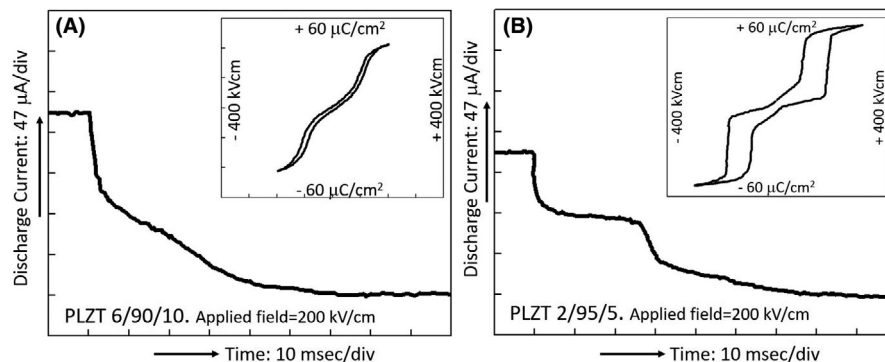
Power electronic circuits require capacitors with high capacitance and high current density, low losses, high operating temperatures, and low equivalent series resistance and inductances to maximize operating frequencies. TDK Corporation has introduced a high-performance MLCC made of AFE PLZT with copper electrodes called Ceralink™ that operates between -55°C and 150°C , at high voltages ~ 500 to 1000 volts, and ~ 10 μF , with high reliability.²⁵² These capacitors have several property advantages over the film capacitors that are the traditional choices, including operating temperature range and suppression of overshoot associated with fast switching of

power semiconductor devices. A comparison between various candidates is shown in Figure 35. As with all MLCC technologies, the reliability design is also a critical aspect of a successful product.

8.2.2 | Defibrillator capacitors

The defibrillator capacitors do not mandate the large high-field repetition rates at high frequencies that DC-link capacitors are designed to withstand. These capacitors have far fewer cycles, and therefore the compositional design can be tailored to body temperature, and with the discharge pulse enabling the most effective stimulation of the cardiac muscle. The field-induced phase transition can, therefore, be less diffuse. As a result, the nonlinearity can be used to control the discharge current time with some constant current plateaus. Figure 36 shows the discharge current and the corresponding hysteresis in PLZT 2/95/5 and 6/90/10.^{253–257}

FIGURE 36 Discharge current versus time in (A) PLZT 2/95/5, (B) PLZT 6/90/10. Insets show the corresponding PE loops (replotted from Ref. [256])



8.2.3 | Thin-film AFE-embedded power capacitors

Although at this time of writing there is no commercialization of AFE thin films, there has been extensive research investigation of thin-film AFE capacitors. The energy densities of AFE are extremely high, reported to be between 20 to 80 J cm^{-3} , as the breakdown strength is typically controlled by thermal breakdown. However, in the scientific literature, unfortunately the reviewing process does not always consider the charge–discharge cycling, and in some cases, the large instantaneous energy density storage values are not necessarily realistic for practical application. However, the most reasonable energy densities $\sim 30 \text{ J cm}^{-3}$ are still intriguing and high.^{258–263} Such AFEs are of interest as power plane decoupling capacitors. This application was identified and considered for high-frequency Multi-Chip-Module packages with embedded thin film capacitors having square hysteresis loops such as can be obtained with compositions like (Sn, Nb) doped PZT. Such AFEs can effectively supply an aerial capacitance $32 \text{ } \mu\text{F cm}^{-2}$, as shown in Figure 37.²⁵⁹

8.3 | Antiferroelectric capacitor memory cell

Recently, Intel was granted a patent (2018) that considers the advantage of using an AFE as a capacitor cell for embedded memory.²⁶⁴ An advantage of such a memory cell is the increased charge density, that may potentially scale better than in the FE equivalents. This may be of interest in neuromorphic computing platforms as the higher charge densities also allows for better distinguishing between the different logic states.²⁶⁵

8.4 | AFE actuator applications

The large volume change associated with AFE/FE phase switching prompts interest in the use of such materials for high strain actuators. For example, PLZT has a tetragonal symmetry that switches to the rhombohedral FE, of which

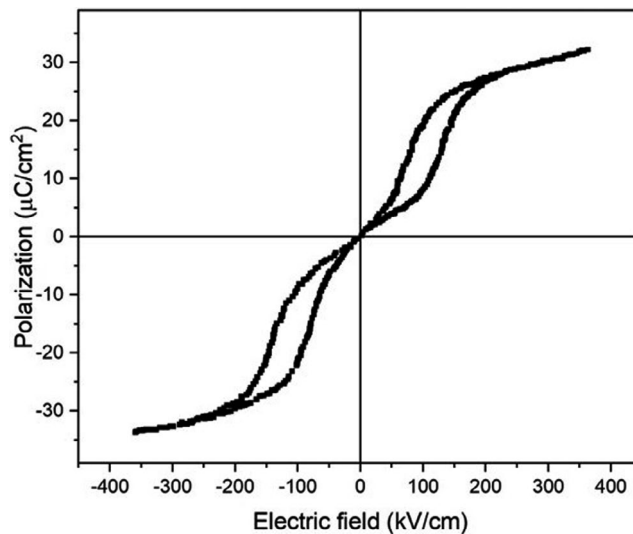


FIGURE 37 P-E hysteresis loop for $(\text{Pb}_{0.97}\text{La}_{0.02})(\text{Zr}_{0.6}\text{Ti}_{0.10}\text{Sn}_{0.30})\text{O}_3$ (replotted from Ref. [259])

the strain-electric field hysteresis is shown for the volume, longitudinal, and transverse switching in Figure 38. The series of phase transition and domain reorientation steps accounts for both the decoupling of the strain and polarization in the longitudinal case, and the coupling in the transverse case.^{7,266–268} As stated in the previous section, the E field endows texturing of the AFE domains.⁴⁸ Lu et al. provided further insights into these processes with a detailed in situ neutron diffraction study. They determined that the field switching of the AFE-FE phase transition is not fully reversible, and the induced strain fields are elliptical and drive preferred orientations of the domain states.²⁶⁹

8.5 | Microwave dielectric materials

AFE materials have been considered for high permittivity microwave frequency dielectrics. Lanagan and Wersing et al. looked at undoped and doped PZ, respectively.^{270,271} The rationale for these was that the $\tan\delta$ would be low, as there is no extrinsic domain contributions, and hence no relaxations in the GHz regime. Unfortunately, the persistence of FE phases and

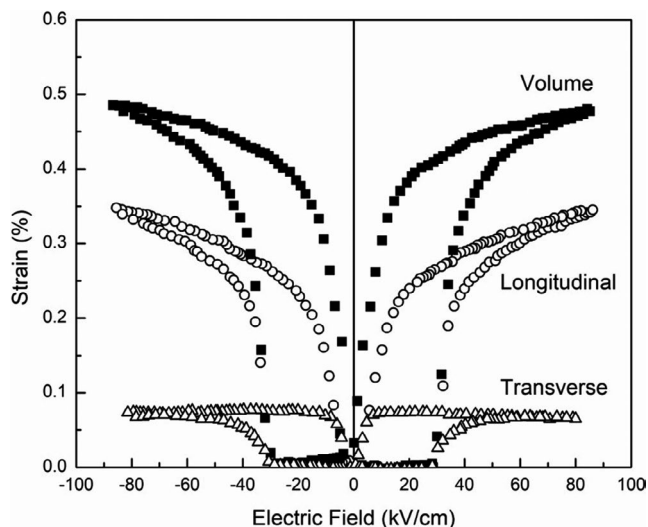


FIGURE 38 Longitudinal/transverse/volume strain as a function of E field (replotted from Ref. [7])

defects often contributed to unacceptable loss levels. Wersing utilized acceptor doping to reduce the extrinsic defect losses, but incomplete reproducibility owing to non-stoichiometric defects was problematic. However, AgNbO_3 in sintered composites with AgTaO_3 has produced temperature stable NPO (Negative-Zero-Positive) high-frequency dielectrics.²⁷² These have high permittivity relative to other microwave dielectrics with equivalent temperature stability.²⁷³ The properties of these AN-AT composite ceramics are compatible with several microwave electronic components, for example, bandpass filters, high-capacity NPO multilayer capacitors, and would lead to the significant miniaturization of these devices. For the case of bandpass filters, an eight-times volume reduction could be expected, allowing ceramic filters with the size of surface acoustic wave (SAW) filters, but with superior improved power handling and low dielectric losses across a wider temperature range. Figure 39 is an image of a commercialized bandpass filter with major advantages in miniaturization relative to a $k = 90$ high-frequency dielectric.²⁴⁶

9 | NEW OPPORTUNITIES FOR FUTURE DIRECTIONS FOR AFE

For a subgroup of dielectric materials that was discovered over 70 years ago, there is still much to be learned from AFE-based materials. AFE are still under-researched relative to their FE counterparts. Also, in terms of compositions and crystal structures, there are few AFE materials relative to FE materials. It is hoped that this review aids the future exploration of new AFE materials. Thinking and predicting the future is always a risky endeavor, but here, some vision on trends that AFE research could provide over the next 10 years or so is discussed. Three pathways

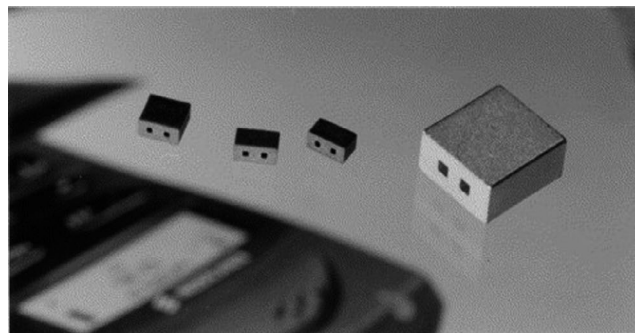


FIGURE 39 Bandpass filters (1.8 and 0.9 GHz) produced from the ANT-ANT composite ceramics and a commercial 1.8 GHz bandpass filter based on $\text{Ba}_{6-x}\text{Nd}_{8+2/3x}\text{Ti}_{18}\text{O}_{54}$ with the permittivity ~ 90 (for the size comparison) (Reproduced by permission from Ref. [246])

are predicted to impact these research areas: materials discovery, scientific needs, and applied science with foreseeable application opportunities.

9.1 | Materials discovery

A fertile new area to discover AFEs is in the families of molecular crystals, organic-inorganic hybrid perovskites, and 2-D materials. Computational discovery of such new materials must use well constrained physics-based algorithms, best practices from identification, and interfacing with high-throughput synthesis methods. There have been recent reports of new FE materials in structures such as plastic/ionic crystals tetramethylammonium tetrachloroferrate(III) and tetramethylammonium bromotrichloroferrate(III).²⁷⁴ These materials have cubic crystal structures in the PE, and therefore this permits many FE domains that can be poled for high-performing piezoelectric and pyroelectric properties. At this time, there is no report of an AFE phase, but this family has only just been discovered. There are similar opportunities in the organic-inorganic hybrid perovskites. However, the discovery of these materials for highly efficient solar cells pushed further exploration of this structure, and strong FE properties have also been reported. After those initial reports of FE, there are now emerging announcements of AFE properties.²⁷⁵⁻²⁷⁷ For instance, in the (3-pyrrolinium) CdBr_3 hybrid perovskite, there is a PE-AFE-FE sequence of transitions, as can be observed in Figure 40.²⁷⁸

These organic and inorganic-organic hybrids have enormous potential, and the discovery process would benefit from data mining and machine learning algorithms, to narrow the focus of the synthetic chemists. In addition to the chemical selection for promising FE and AFEs, the hydroscopic nature of these materials also needs to be considered for long-term success.

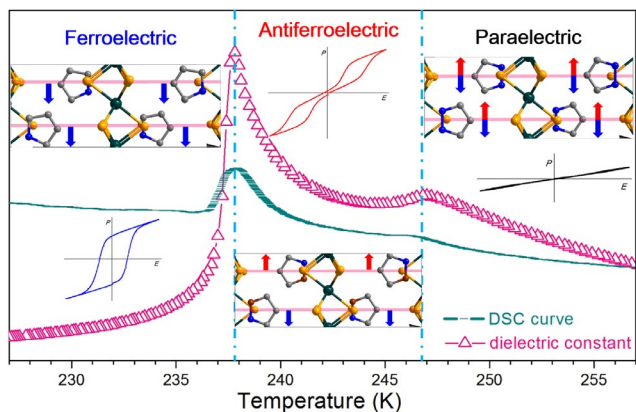


FIGURE 40 PE-AFE-FE phase transitions in (3-pyrrolinium) CdBr_3 hybrid perovskite [Color figure can be viewed at wileyonlinelibrary.com]

9.2 | Future scientific directions

There has been major progress in the scientific understanding of AFE through detailed crystallographic investigations, microscopy at the atomic level, understanding the relative energetics of the FE and AFE phases in compounds through detailed DFT calculations, and applying broad compositional studies to discover new AFEs. There are still many compositions and solid solutions that need thorough study to see if the understanding holds across more systems. There are also new crystal systems emerging with AFE that have been discussed in this review that need much broader investigation, particularly as some of them have extremely interesting coupled properties, such as the M-hexaferrites. There are still many questions regarding the details of the AFE-FE switching, regarding nucleation and growth of the FE phase in the forward switching and conversely the AFE nucleation at fields on back switching. In several systems, there is also an INC phase that develops with doping and/or as intermediate states in the AFE-FE switching process. The coupling of the electromechanical process at the local scale is also not understood. As pointed out in this review, the role of flexoelectricity may be fundamental to the properties and structures that underpin AFEs. The field requires higher levels of investigation, both experimentally and with theoretical approaches. The dynamics of the PE-AFE and AFE-FE phase transitions also need more detailed analysis in model single crystal systems, to understand the interplay of soft-mode coupling with various external boundary conditions: temperature, field, and mechanical stresses. The role of defect chemistry, its impact on high field behavior, and the impact of doping on the domain switching characteristics is also expected to be critical. The separation of dielectric loss mechanisms across broad frequency ranges, from infra-red, terahertz, and microwave is required. Likewise, the determination of

lattice modes, soft modes, domain dynamics, and conduction contributions to AFE behavior is necessary.

9.3 | Future AFE materials engineering and application pulls

Relative to FE materials, applications have been limited for AFEs. However, the recent introduction of the mass-produced DC-link capacitor will reduce future uncertainties in business decisions around such materials. With many of the high-performing AFEs being related to lead-based perovskites, there are still concerns over toxicity. So, the discovery of lead-free alternatives with high performance would be of great interest to the industry to avoid future issues under the Restriction of Hazardous Substances (RoHS) legislation. Two important industrial application pulls are power electronics and 5G (and beyond), and in both these cases, electronic components that can withstand high temperatures and high charge–discharge rates, while maintaining low losses and stable temperature operations, need to be developed. AFE can provide opportunities in these domains. The AFE can also offer opportunities for MEMS structures, owing to the large electromechanical responses that can be achieved. The electrically induced strain effect of the AFE thin film produced under an electric field and its application in cantilever MEMS drive enables a large displacement, fast response, and low energy consumption, which can significantly improve the performance of MEMS. AFE capacitive memories will also have opportunities in future computation and have already gained interest in neuromorphic computing owing to large polarizations and size effects that are less sensitive than in some FE cases. Molecular inorganic–organic AFE may offer large electrocaloric responses that could be integrated into flexible electronics to provide solid-state actively cooled power electronic packages, and/or on larger scales for food–drug refrigeration and building air cooling. All these areas desperately need new technologies, and they are of such a scale that the solutions must be sustainable. Even with present FE-based materials that are driven through a Carnot cycle, a coefficient of performance (COP) of six has been achieved in prototypes for electrocaloric refrigeration; this exceeds that of sublimation refrigeration technology, with COP ~ 4 .²⁷⁹ So, from a global technology and environmental perspective, AFE are an important dielectric material that deserves broader exploration and studies.

ACKNOWLEDGMENTS

The authors gratefully acknowledge support from the National Science Foundation I/UCRC, Center for Dielectrics and Piezoelectrics, under Grant Nos. IIP-1841453 and 1841466.

ORCID

Clive A. Randall  <https://orcid.org/0000-0002-5478-2699>

Susan Trolier-McKinstry  <https://orcid.org/0000-0002-7267-9281>

[org/0000-0002-7267-9281](https://orcid.org/0000-0002-7267-9281)

REFERENCES

- Isupov VA. Ferroelectric and antiferroelectric perovskites $\text{Pb}(\text{B}'_{0.5}\text{B}''_{0.5})\text{O}_3$. *Ferroelectric*. 2003;289:131–95.
- Smolenskii GA, Bokov VA, Isupov VA, Kraini NN, Pasynkov PE, Sokolov VI. *Ferroelectrics and related materials*. New York: Gordon and Breach; 1984.
- Rabe KM. Antiferroelectricity in oxides: a reexamination. In: Ogale S, Venkatesham V, editors. *Functional metal oxides*. Hoboken, NJ: Wiley; 2013. p. 221–44.
- Tan X, Ma C, Fredrick J, Beckman S, Webber K. The antiferroelectric \leftrightarrow ferroelectric phase transition in lead-containing and lead-free perovskite ceramics. *J Am Ceram Soc*. 2011;94:4091–107.
- Mitsui T. *Ferroelectrics and antiferroelectrics*. In: Warlimont H, Martienssen W, editors. *Springer handbook of materials data*. Cham, Switzerland: Springer; 2018. p. 901–34.
- Tolédano P, Guennou M. Theory of antiferroelectric phase transitions. *Phys Rev B*. 2016;94:014107.
- Park SE, Pan MJ, Markowski K, Yoshikawa S, Cross LE. Electric field induced phase transition of antiferroelectric lead lanthanum zirconate titanate stannate ceramics. *J Appl Phys*. 1997;82:1798–803.
- Valasek J. Piezo-electric and allied phenomena in Rochelle salt. *Phys Rev*. 1921;17(4):475.
- Néel L. Théorie du paramagnétisme constant; application au manganèse. *C R Hebd Seances Acad Sci*. 1936;203:304–6.
- Thurnaurer H, Deaderick J. U.S. patent no. 2,429,588 (21 October 1947, filed 1941).
- Wainer E, Solomon AE. Titanium Alloy Manufacturing Co. report no. 8 (September 1942) and no. 9 (January 1943).
- Ogawa T, Waku S. (discovered 1944); Ogawa T. On polymorphic changes in BaTiO_3 . *J Phys Soc Jap*. 1946;1:32–34.
- Wul BM, Goldman JB. Dielectric constant of titanites of metals of the second group. *Dokl Acad Nauk SSSR*. 1945;46:154–157.
- Randall CA, Newnham RE, Cross LE. *History of the first ferroelectric oxide, BaTiO_3* . University Park, PA: Materials Research Institute: The Pennsylvania State University; 2004.
- Shirane G, Sawaguchi E, Takagi Y. Dielectric properties of lead zirconate. *Phys Rev*. 1951;84:476.
- Shirane G. Ferroelectricity and antiferroelectricity in ceramic PbZrO_3 containing Ba or Sr. *Phys Rev*. 1952;86:219.
- Sawaguchi E, Maniwa H, Hoshino S. Antiferroelectric structure of lead zirconate. *Phys Rev*. 1951;83:1078.
- Kittel C. Theory of antiferroelectric crystals. *Phys Rev*. 1951;82:729.
- Shirane G, Pepinsky R. Phase transitions in antiferroelectric PbHfO_3 . *Phys Rev*. 1953;91:812.
- Shirane G, Newnham R, Pepinsky R. Dielectric properties and phase transitions of NaNbO_3 and $(\text{Na}, \text{K})\text{NbO}_3$. *Phys Rev*. 1954;96:581.
- Wood EA. Polymorphism in potassium niobate, sodium niobate, and other ABO_3 compounds. *Acta Crystallogr*. 1951;4:353–62.
- Cross LE, Nicholson BJ. The optical and electrical properties of single crystals of sodium niobate. *Lond Edinb Dubl Phil Mag J Sci*. 1955;46:453–66.
- Cross LE. A thermodynamic treatment of ferroelectricity and antiferroelectricity in pseudo-cubic dielectrics. *Philos Mag*. 1956;1:76–92.
- Keeling RO, Pepinsky R. An X-ray diffraction study of the transition in $\text{NH}_4\text{H}_2\text{PO}_4$ at 148 K. *Z Krist-Cryst Mater*. 1954;106:236–65.
- Cochran W. Crystal stability and the theory of ferroelectricity. *Phys Rev Lett*. 1959;3:412.
- Venkataraman G. Soft modes and structural phase transitions. *Bull Mater Sci*. 1979;1:129–70.
- Jaffe B, Cook WR, Jaffe H. *Piezoelectric ceramics*. London and New York: Academic Press; 1971.
- Samara GA. Pressure and temperature dependence of the dielectric properties and phase transitions of the ferroelectric perovskites: PbTiO_3 and BaTiO_3 . *Ferroelectrics*. 1971;2:277–89.
- Samara GA. Vanishing of the ferroelectric and antiferroelectric states in KH_2PO_2 -type crystals at high pressure. *Phys Rev Lett*. 1971;27:103.
- Liu Y, Yang X, He C, Li X, Wang Z, Xiao Y, et al. Domain and antiferroelectric properties of $\text{Pb}(\text{Lu}_{1/2}\text{Nb}_{1/2})\text{O}_3$ single crystals and their superlattice structure. *RSC Adv*. 2017;7:3704–12.
- Young SE, Zhang JY, Hong W, Tan X. Mechanical self-confinement to enhance energy storage density of antiferroelectric capacitors. *J Appl Phys*. 2013;113:054101.
- Fesenko OE, Kolesova RV, Sindeyev YG. The structural phase transitions in lead zirconate in super-high electric fields. *Ferroelectrics*. 1978;20:177–8.
- Ishchuk VM. Peculiarities of ferro–antiferroelectric phase transitions: 4. Intermediate states in ferro- and antiferroelectrics. *Ferroelectrics*. 1998;209:569–88.
- Ishchuk VM, Sobolev VL. Investigation of two-phase nucleation in paraelectric phase of ferroelectrics with ferroelectric–antiferroelectric–paraelectric triple point. *J Appl Phys*. 2002;92:2086–93.
- Tan X, Frederick J, Ma C, Rödel J. Can an electric field induce an antiferroelectric phase out of a ferroelectric phase? *Phys Rev Lett*. 2010;105:255702.
- Lambeck PV, Jonker GH. The nature of domain stabilization in ferroelectric perovskites. *J Phys Chem Solids*. 1986;47:453–61.
- Robels U, Arlt G. Domain wall clamping in ferroelectrics by orientation of defects. *J Appl Phys*. 1993;73:3454–60.
- Carl K, Hardtl KH. Electrical after-effects in $\text{Pb}(\text{Ti}, \text{Zr})\text{O}_3$ ceramics. *Ferroelectrics*. 1977;17:473–86.
- Feng Z, Or SW. Aging-induced, defect-mediated double ferroelectric hysteresis loops and large recoverable electrostrains in Mn-doped orthorhombic KNbO_3 -based ceramics. *J Alloys Compd*. 2009;480:L29–L32.
- Feng Z, Ren X. Aging effect and large recoverable electrostrain in Mn-doped KNbO_3 -based ferroelectrics. *Appl Phys Lett*. 2007;91:032904.
- Hao X, Zhai J, Kong LB, Xu Z. A comprehensive review on the progress of lead zirconate-based antiferroelectric materials. *Prog Mater Sci*. 2014;63:1–57.
- Randall CA, Barber DJ, Groves P, Whatmore RW. TEM study of the disorder-order perovskite $\text{Pb}(\text{In}_{1/2}\text{Nb}_{1/2})\text{O}_3$. *J Mater Sci*. 1988;23:3678–82.
- Sawaguchi E. Ferroelectricity versus antiferroelectricity in the solid solutions of PbZrO_3 and PbTiO_3 . *J Phys Soc Jpn*. 1953;8:615–29.
- Kay HF, Vousden P. Symmetry changes in barium titanate at low temperatures and their relation to its ferroelectric properties. *Lond Edinb Dubl Phil Mag J Sci*. 1949;40:1019–40.

45. Avdeev M, Jorgensen JD, Short S, Samara GA, Venturini EL, Yang P, et al. Pressure-induced ferroelectric to antiferroelectric phase transition in $\text{Pb}_{0.99}(\text{Zr}_{0.95}\text{Ti}_{0.05})_{0.98}\text{Nb}_{0.02}\text{O}_3$. *Phys Rev B*. 2006;73:064105.
46. Tan X, Frederick J, Ma C, Aulbach E, Marsilius M, Hong W, et al. Electric-field-induced antiferroelectric to ferroelectric phase transition in mechanically confined $\text{Pb}_{0.99}\text{Nb}_{0.02}[(\text{Zr}_{0.57}\text{Sn}_{0.43})_{0.94}\text{Ti}_{0.06}]_{0.98}\text{O}_3$. *Phys Rev B*. 2010;81:014103.
47. Cao H, Evans AG. Nonlinear deformation of ferroelectric ceramics. *J Am Ceram Soc*. 1993;76:890–6.
48. Liu H, Fan L, Sun S, Lin K, Ren Y, Tan X, et al. Electric-field-induced structure and domain texture evolution in PbZrO_3 -based antiferroelectric by in-situ high-energy synchrotron X-ray diffraction. *Acta Mater*. 2020;184:41–9.
49. Novak N, Weyland F, Patel S, Guo H, Tan X, Rodel J, et al. Interplay of conventional with inverse electrocaloric response in $(\text{Pb}, \text{Nb})(\text{Zr}, \text{Sn}, \text{Ti})\text{O}_3$ antiferroelectric materials. *Phys Rev B*. 2018;97:094113.
50. Tachibana M, Kolodiaznyh T, Takayama-Muromachi E. Thermal conductivity of perovskite ferroelectrics. *Appl Phys Lett*. 2008;93:092902.
51. Scott JF. Electrocaloric materials. *Annu Rev Mater Res*. 2011;41:229–40.
52. Takeuchi I, Sandeman K. Solid-state cooling with caloric materials. *Phys Today*. 2015;68:48–54.
53. Geng W, Liu Y, Meng X, Bellaiche L, Scott JF, Dkhil B, et al. Giant negative electrocaloric effect in antiferroelectric La-doped $\text{Pb}(\text{ZrTi})\text{O}_3$ thin films near room temperature. *Adv Mater*. 2015;27:3165–9.
54. Grünebohm A, Ma YB, Marathe M, Xu BY, Able K, Kalcher C, et al. Origins of the inverse electrocaloric effect. *Energy Technol*. 2018;6:1491–511.
55. Kimmel AV, Gindele OT, Duffy DM, Cohen RE. Giant electrocaloric effect at the antiferroelectric-to-ferroelectric phase boundary in $\text{Pb}(\text{Zr}_x\text{Ti}_{1-x})\text{O}_3$. *Appl Phys Lett*. 2019;115:023902.
56. Blinc R. The soft mode concept and the history of ferroelectricity. *Ferroelectrics*. 1987;74:301–3.
57. Fleury PA. The effects of soft modes on the structure and properties of materials. *Annu Rev Mater Sci*. 1976;6:157–80.
58. Blinc R. *Soft modes in ferroelectrics and antiferroelectrics*. New York: Elsevier North-Holland; 1974.
59. Lee S, Troller-McKinstry S, Randall CA. Ferroelectric-thermoelectricity and Mott transition of ferroelectric oxides with high electronic conductivity. *J Eur Ceram Soc*. 2012;32:3971–88.
60. Bussmann-Holder A, Ko JH, Majchrowski A, Górny M, Roleder K. Precursor dynamics, incipient ferroelectricity and huge anharmonicity in antiferroelectric lead zirconate PbZrO_3 . *J Phys Condens Matter*. 2013;25:212202.
61. Cross LE. Flexoelectric effects: charge separation in insulating solids subjected to elastic strain gradients. *J Mater Sci*. 2006;41:53–63.
62. Tagantsev AK. Piezoelectricity and flexoelectricity in crystalline dielectrics. *Phys Rev B*. 1986;34:5883.
63. Wang B, Gu Y, Zhang S, Chen LQ. Flexoelectricity in solids: progress, challenges, and perspectives. *Prog Mater Sci*. 2019;106:100570.
64. Vales-Castro P, Roleder K, Zhao L, Li JF, Kajewski D, Catalan G. Flexoelectricity in antiferroelectrics. *Appl Phys Lett*. 2016;113:132903.
65. Ma W, Cross LE. Flexoelectric polarization of barium strontium titanate in the paraelectric state. *Appl Phys Lett*. 2002;81:3440–2.
66. Garten LM, Trolrier-McKinstry S. Enhanced flexoelectricity through residual ferroelectricity in barium strontium titanate. *J Appl Phys*. 2015;117:094102.
67. Tagantsev AK, Vaideeswaran K, Vakhrushev SB, Filimonov AV, Burkovsky RG, Shaganov A, et al. The origin of antiferroelectricity in PbZrO_3 . *Nat Commun*. 2013;4:1–8.
68. Axe JD, Harada J, Shirane G. Anomalous acoustic dispersion in centrosymmetric crystals with soft optic phonons. *Phys Rev B*. 1970;1:1227.
69. Borisevich AY, Eliseev EA, Morozovska AN, Cheng CJ, Lin JY, Chu YH, et al. Atomic-scale evolution of modulated phases at the ferroelectric–antiferroelectric morphotropic phase boundary controlled by flexoelectric interaction. *Nat Commun*. 2012;3:1–8.
70. Scott JF. Phase transitions in ferroelectric thin films. *Phase Transit*. 1991;30:107–10.
71. Kretschmer R, Binder K. Surface effects on phase transitions in ferroelectrics and dipolar magnets. *Phys Rev B*. 1979;20:1065.
72. Wang CL, Smith SRP. Landau theory of the size-driven phase transition in ferroelectrics. *J Phys Condens Matter*. 1995;7:7163.
73. Garvie RC. The occurrence of metastable tetragonal zirconia as a crystallite size effect. *J Phys Chem*. 1965;69:1238–43.
74. Buscaglia V, Randall CA. Size and scaling effects in barium titanate. An overview. *J Eur Ceram Soc*. 2020;40:3744–58.
75. Eliseev EA, Glinchuk MD, Morozovska AN. Antiferroelectric thin films phase diagrams. *Phase Transit*. 2007;80:47–54.
76. Mani BK, Chang CM, Lisenkov S, Ponomareva I. Critical thickness for antiferroelectricity in PbZrO_3 . *Phys Rev Lett*. 2015;115:097601.
77. Randall CA, Kim N, Kucera JP, Cao W, Shrout T. Intrinsic and extrinsic size effects in fine-grained morphotropic-phase-boundary lead zirconate titanate ceramics. *J Am Ceram Soc*. 1998;1:677–88.
78. Ihlefeld JF, Harris DT, Keech R, Jones JL, Maria JP, Trolrier-McKinstry S. Scaling effects in perovskite ferroelectrics: fundamental limits and process-structure-property relations. *J Am Ceram Soc*. 2016;99:2537–57.
79. Chattopadhyay S, Ayyub P, Palkar VR, Gurjar AV, Wankar RM, Multani M. Finite-size effects in antiferroelectric nanoparticles. *J Phys Condens Matter*. 1997;9:8135.
80. Cross LE. Antiferroelectric-ferroelectric switching in a simple “Kittel” antiferroelectric. *J Phys Soc Jpn*. 1967;23:77–82.
81. Okada K. Phenomenological theory of antiferroelectric transition. i. second-order transition. *J Phys Soc Jpn*. 1969;27:420–8.
82. Haun MJ, Harvin TJ, Lanagan MT, Zhuang ZQ, Jang SJ, Cross LE. Thermodynamic theory of PbZrO_3 . *J Appl Phys* 1989;65:3173–80.
83. Eliseev EA, Glinchuk MD. Size-induced appearance of ferroelectricity in thin antiferroelectric films. *Phys B Condens Matter*. 2007;400:106–13.
84. Balashova EV, Tagantsev AK. Polarization response of crystals with structural and ferroelectric instabilities. *Phys Rev B*. 1993;48:9979.
85. Xue F, Liang L, Gu Y, Takeuchi I, Kalinin SV, Chen LQ. Composition- and pressure-induced ferroelectric to antiferroelectric phase transitions in Sm-doped BiFeO_3 system. *Appl Phys Lett*. 2015;106:012903.
86. Corker DL, Glazer AM, Whatmore RW, Stallard A, Fauth F. A re-investigation of the crystal structure of the perovskite PbZrO_3 by X-ray and neutron diffraction. *Acta Crystallogr B*. 1997;53:135–42.

87. Whatmore RW, Glazer AM. Structural phase transitions in lead zirconate. *J Phys C Solid State Phys.* 1979;12:1505.
88. Roleder K, Kugel GE, Handerek J, Fontana MD, Carabatos C, Hafid M, et al. The 1st evidence of 2 phase-transitions in PbZrO_3 crystals derived from simultaneous Raman and dielectric measurements. *Ferroelectrics.* 1988;80:809–12.
89. Fujishita H, Hoshino S. A study of structural phase transitions in antiferroelectric PbZrO_3 by neutron diffraction. *J Phys Soc Jpn.* 1984;53:226–34.
90. Tanaka M, Saito M, Tsuzuki K. Determinations of space group and oxygen coordinates in the antiferroelectric phase of lead zirconate by conventional and convergent-beam electron diffraction. *J Phys Soc Jpn.* 1982;51:2635–40.
91. Zhang N, Pasciak M, Glazer AM, Hlinka J, Gutmann M, Sparkes HA, et al. A neutron diffuse scattering study of PbZrO_3 and Zr-rich $\text{PbZr}_{1-x}\text{Ti}_x\text{O}_3$. *J Appl Crystallogr.* 2015;48:1637–44.
92. Teslic S, Egami T. Atomic structure of PbZrO_3 determined by pulsed neutron diffraction. *Acta Crystallogr B.* 1998;54:750–65.
93. Dernier PD, Remeika JP. Synthesis and symmetry transformation in the perovskite compounds PbHfO_3 and CdHfO_3 . *Mater Res Bull.* 1975;10:187–92.
94. Leont'ev NG, Kolesova RV, Eremkin VV, Fesenko OE, Smotrakov VG. Space group of high-temperature orthorhombic phase of lead hafnate. *Sov Phys Crystallogr.* 1984;29:395–7.
95. Fujishita H, Ishikawa Y, Ogawaguchi A, Kato K, Nishibori E, Takata M, et al. A study of structures and order parameters in antiferroelectric PbHfO_3 by synchrotron radiation. *J Phys Soc Jpn.* 2005;74:2743–7.
96. Kupriyanov MF, Petrovich EV, Dutova EV, Kabirov YV. Sequence of phase transitions in PbHfO_3 . *Crystallogr Rep.* 2012;57:205–7.
97. Mączka M, Kim TH, Gagor A, Jankowska-Sumara I, Majchrowski A, Kojima S. Brillouin scattering, DSC, dielectric and X-ray diffraction studies of phase transitions in antiferroelectric PbHfO_3 : Sn. *J Alloys Compd.* 2015;622:935–41.
98. Sakata K, Masuda Y. Ferroelectric and antiferroelectric properties of $(\text{Na}_{0.5}\text{Bi}_{0.5})\text{TiO}_3$ - SrTiO_3 solid solution ceramics. *Ferroelectrics.* 1974;7:347–9.
99. Kupriyanov MF, Fesenko EG. Preparation and study of compounds of type $\text{Pb}_2\text{B}_1\text{B}_2\text{O}_6$. *Sov Phys Crystallogr.* 1965;10:189.
100. Bokov AA, Shonov VY, Rayevsky IP, Gagarina ES, Kupriyanov MF. Compositional ordering and phase transitions in $\text{Pb}(\text{Yb}_{0.5}\text{Nb}_{0.5})\text{O}_3$. *J Phys Condens Matter.* 1993;5:5491.
101. Isupov VA, Krainik NN. New antiferroelectrics having perovskite-type structure containing rare-earth ions in octahedral lattice sites. *Sov Phys Solid State.* 1965;6:2975.
102. Sternberg A, Shebanovs L, Antonova M, Livinsh M, Yamashita YJ, Shorubalko I, et al. New high piezoelectric coupling PLuNT binary system ceramics. *Nanostruct Mater.* 1999;12:645–8.
103. Liu Y, Li X, Wang Z, He C, Li T, Ai L, et al. A new $(1-x)\text{Pb}(\text{Lu}_{1/2}\text{Nb}_{1/2})\text{O}_3$ - $x\text{PbTiO}_3$ binary ferroelectric crystal system with high Curie temperature. *Cryst Eng Comm.* 2013;15:1643–50.
104. Isupov VA, Belous LP. Phase transition in antiferroelectric $\text{PbCo}_{0.5}\text{W}_{0.5}\text{O}_3$ and $\text{PbCo}_{0.5}\text{W}_{0.5}\text{O}_3$ - PbTiO_3 solid solutions. *Sov Phys Crystallogr.* 1971;16:129.
105. Baldinozzi G, Sciau PH, Pinot M, Grebille D. Crystal structure of the antiferroelectric perovskite Pb_2MgWO_6 . *Acta Crystallogr B.* 1995;51:668–73.
106. Randall CA, Markgraf SA, Bhalla AS, Baba-Kishi K. Incommensurate structures in highly ordered complex perovskites $\text{Pb}(\text{Co}_{1/2}\text{W}_{1/2})\text{O}_3$ and $\text{Pb}(\text{Sc}_{1/2}\text{Ta}_{1/2})\text{O}_3$. *Phys Rev B.* 1989;40:413.
107. Zaslavskii AI, Bryzhina MF. An X-ray structural investigation of the antiferroelectric Pb_2MgWO_6 and the system of solid solutions Pb_2MgWO_6 - PbTiO_3 . *Sov Phys Crystallogr.* 1963;7:577–83.
108. Kania A, Rowinski E. Dielectric properties for differently quenched $\text{PbIn}_{0.5}\text{Nb}_{0.5}\text{O}_3$ crystals. *Ferroelectrics.* 1991;124:265–70.
109. Groves P. Structural phase transitions and long-range order in ferroelectric perovskite lead indium niobate. *J Phys C Solid State Phys.* 1986;19:111.
110. Bokov AA, Raevskii IP, Smotrakov VG. Composition, ferroelectric and antiferroelectric ordering in $\text{Pb}_2\text{InNbO}_6$ crystals. *Sov Phys Solid State.* 1984;26:2824–8.
111. Roleder K, Maglione M, Fontana MD, Jankowska-Sumara I, Kugel GE, Dec J. Dielectric spectroscopy of the antiferroelectric PbHfO_3 . *Ferroelectrics.* 2000;238:139–46.
112. Bosak A, Svitlyk V, Arakcheeva A, Burkovsky R, Diadkin V, Roleder K, et al. Incommensurate crystal structure of PbHfO_3 . *Acta Crystallogr B.* 2020;76:7–12.
113. Johnston KE, Tang CC, Parker JE, Knight KS, Lightfoot P, Ashbrook SE. The polar phase of NaNbO_3 : a combined study by powder diffraction, solid-state NMR, and first-principles calculations. *J Am Chem Soc.* 2010;132:8732–46.
114. Lefkowitz I, Łukaszewicz K, Megaw HD. The high-temperature phases of sodium niobate and the nature of transitions in pseudosymmetric structures. *Acta Crystallogr.* 1966;20:670–83.
115. Mishra SK, Choudhury N, Chaplot SL, Krishna PSR, Mittal R. Competing antiferroelectric and ferroelectric interactions in NaNbO_3 : Neutron diffraction and theoretical studies. *Phys Rev B.* 2007;76:024110.
116. Xu Y, Hong W, Feng Y, Tan X. Antiferroelectricity induced by electric field in NaNbO_3 -based lead-free ceramics. *Appl Phys Lett.* 2014;104:052903.
117. Shimizu H, Guo H, Reyes-Lillo SE, Mizuno Y, Rabe KM, Randall CA. Lead-free antiferroelectric: $x\text{CaZrO}_3$ - $(1-x)\text{NaNbO}_3$ system ($0 \leq x \leq 0.10$). *Dalton Trans.* 2015;44:10763–72.
118. Guo H, Shimizu H, Mizuno Y, Randall CA. Strategy for stabilization of the antiferroelectric phase (Pbma) over the metastable ferroelectric phase (P2₁ma) to establish double loop hysteresis in lead-free $(1-x)\text{NaNbO}_3$ - $x\text{SrZrO}_3$ solid solution. *J Appl Phys.* 2015;117:214103.
119. Randall CA, Barber DJ, Groves P, Whatmore RW. TEM study of the disorder-order perovskite, $\text{Pb}(\text{In}_{1/2}\text{Nb}_{1/2})\text{O}_3$. *J Mater Sci.* 1988;23:3678–82.
120. Yoneda Y, Suzuya K, Mizuki J. Local structure of relaxor $\text{Pb}(\text{In}_{0.5}\text{Nb}_{0.5})\text{O}_3$ ferroelectrics. *J Appl Phys.* 2006;100:093521.
121. Ohwada K, Tsukada S, Fukuda T, Tsutsui S, Baron AQR, Mizuki J, et al. Effect of B-site randomness on the antiferroelectric/relaxor nature of the ground state: Diffuse and inelastic x-ray scattering study of $\text{Pb}(\text{In}_{1/2}\text{Nb}_{1/2})\text{O}_3$. *Phys Rev B.* 2018;98:054106.
122. Reaney IM, Woodward DI, Randall CA. Displacive phase transitions and intermediate structures in perovskites. *J Am Ceram Soc.* 2011;94:2242–7.
123. Ma C, Tan X, Dulkin E, Roth M. Domain structure-dielectric property relationship in lead-free $(1-x)(\text{Bi}_{1/2}\text{Na}_{1/2})\text{TiO}_3$ - $x\text{BaTiO}_3$ ceramics. *J Appl Phys.* 2010;108:104105.
124. Jones GO, Thomas PA. Investigation of the structure and phase transitions in the novel A-site substituted distorted perovskite compound $\text{Na}_{0.5}\text{Bi}_{0.5}\text{TiO}_3$. *Acta Crystallogr B.* 2002;58:168–78.
125. Shannon RD, Prewitt CT. Effective ionic radii in oxides and fluorides. *Acta Crystallogr B.* 1969;25:925–46.

126. Goldschmidt VM. Die gesetze der kristallochemie. *Sci Nat.* 1926;14:477–85.
127. Megaw HD. *Ferroelectricity in crystals.* London: Methuen & Co.; 1957.
128. Evans RC. *An introduction to crystal chemistry.* Cambridge: Cambridge University Press; 1966.
129. Galasso FS. *Structure, properties and preparation of perovskite-type compounds.* Oxford: Pergamon Press; 2013.
130. Fesenko EG. *Perovskite family and ferroelectricity.* Moscow: Atomizdat; 1972.
131. Navrotsky A. *Physics and chemistry of earth materials.* Cambridge: Cambridge University Press; 1994.
132. Reaney IM, Colla EL, Setter N. Dielectric and structural characteristics of Ba-based and Sr-based complex perovskites as a function of tolerance factor. *Jpn J Appl Phys.* 1995;33:3984–90.
133. Eitel RE, Randall CA, Shrout TR, Rehrig PW, Hackenberger W, Park SE. New high temperature morphotropic phase boundary piezoelectrics based on Bi(Me)O₃-PbTiO₃ ceramics. *Jpn J Appl Phys.* 2001;40:5999–6002.
134. Arnold DC, Knight KS, Morrison FD, Lightfoot P. Ferroelectric-paraelectric transition in BiFeO₃: crystal structure of the orthorhombic β phase. *Phys Rev Lett.* 2009;102:027602.
135. Fujino S, Murakami M, Anbusathaiah V, Lim SH, Nagarajan V, Fennie CJ, et al. Combinatorial discovery of a lead-free morphotropic phase boundary in a thin-film piezoelectric perovskite. *Appl Phys Lett.* 2008;92:202904.
136. Cheng CJ, Kan D, Lim SH, McKenzie WR, Munroe PR, Salamanca-Riba LG, et al. Structural transitions and complex domain structures across a ferroelectric-to-antiferroelectric phase boundary in epitaxial Sm-doped BiFeO₃ thin films. *Phys Rev B.* 2009;80:014109.
137. Kan D, Pálová L, Anbusathaiah V, Cheng CJ, Fujino S, Nagarajan V, et al. Universal behavior and electric-field-induced structural transition in rare-earth-substituted BiFeO₃. *Adv Funct Mater.* 2010;20:1108–15.
138. Karimi S, Reaney IM, Han Y, Pokorny J, Sterianou I. Crystal chemistry and domain structure of rare-earth doped BiFeO₃ ceramics. *J Mater Sci.* 2009;44:5102–12.
139. Karimi S, Reaney IM, Levin I, Sterianou I. Nd-doped BiFeO₃ ceramics with antipolar order. *Appl Phys Lett.* 2009;94:112903.
140. Levin I, Tucker MG, Wu H, Provenzano V, Dennis CL, Karimi S, et al. Displacive phase transitions and magnetic structures in Nd-substituted BiFeO₃. *Chem Mater.* 2011;23:2166–75.
141. Yang CH, Kan D, Takeuchi I, Nagarajan V, Seidel J. Doping BiFeO₃: approaches and enhanced functionality. *Phys Chem Chem Phys.* 2002;14:15953–62.
142. Kalantari K, Sterianou I, Sinclair DC, Bingham PA, Pokorny J, Reaney IM. Structural phase transitions in Ti-doped Bi_{1-x}Nd_xFeO₃ ceramics. *J Appl Phys.* 2012;111:064107.
143. Woodward DI, Reaney IM. Electron diffraction of tilted perovskites. *Acta Crystallogr B.* 2005;61:387–99.
144. Maso N, West AR. Electrical properties of Ca-doped BiFeO₃ ceramics: from p-type semiconduction to oxide-ion conduction. *Chem Mater.* 2012;24:2127–32.
145. Kalantari K, Sterianou I, Karimi S, Ferrarelli MC, Miao S, Sinclair DC, et al. Ti-doping to reduce conductivity in Bi_{0.85}Nd_{0.15}FeO₃ ceramics. *Adv Funct Mater.* 2011;21:3737–43.
146. MacLaren I, Wang LQ, Schaffer B, Ramasse QM, Craven AJ, Selbach SM, et al. Novel nanorod precipitate formation in neodymium and titanium codoped bismuth ferrite. *Adv Funct Mater.* 2013;23:683–9.
147. MacLaren I, Wang LQ, Morris O, Craven AJ, Stamps RL, Schaffer B, et al. Local stabilisation of polar order at charged antiphase boundaries in antiferroelectric (Bi_{0.85}Nd_{0.15})(Ti_{0.1}Fe_{0.9})O₃. *APL Mater.* 2013;1:021102.
148. Salih JM, Wang LQ, Ramasse QM, Jones L, Barthel J, Reaney IM, et al. Maghemite-like regions at the crossing of two antiphase boundaries in doped BiFeO₃. *Mater Sci Technol.* 2016;32:242–7.
149. Johnston KE, Griffin JM, Walton RI, Dawson DM, Lightfoot P, Ashbrook SE. ⁹³Nb NMR and DFT investigation of the polymorphs of NaNbO₃. *Phys Chem Chem Phys.* 2011;13:7565–76.
150. Gao L, Guo H, Zhang S, Randall CA. Stabilized antiferroelectricity in xBiScO₃-(1-x)NaNbO₃ lead-free ceramics with established double hysteresis loops. *Appl Phys Lett.* 2018;112:092905.
151. Guo H, Shimizu H, Randall CA. Direct evidence of an incommensurate phase in NaNbO₃ and its implication in NaNbO₃-based lead-free antiferroelectrics. *Appl Phys Lett.* 2015;107:112904.
152. Raevski IP, Prosandeev SA. A new, lead free, family of perovskites with a diffuse phase transition: NaNbO₃-based solid solutions. *J Phys Chem Solids.* 2002;63:1939–50.
153. Shakhovoy RA, Raevskaya SI, Shakhovaya LA, Suzdalev DV, Raevski IP, Yuzyuk YI, et al. Ferroelectric Q and antiferroelectric P phases' coexistence and local phase transitions in oxygen-deficient NaNbO₃ single crystal: micro-Raman, dielectric and dilatometric studies. *J Raman Spectrosc.* 2012;43:1141–5.
154. Gao J, Zhao L, Liu Q, Wang X, Zhang S, Li JF. Antiferroelectric-ferroelectric phase transition in lead-free AgNbO₃ ceramics for energy storage applications. *J Am Ceram Soc.* 2018;101:5443–50.
155. Kania A, Roleder K, Kugel GE, Fontana MD. Raman scattering, central peak and phase transitions in AgNbO₃. *J Phys C.* 1986;19:9.
156. Sciau PH, Kania A, Dkhil B, Suard E, Ratuszna A. Structural investigation of AgNbO₃ phases using x-ray and neutron diffraction. *J Phys Condens Matter.* 2004;16:2795.
157. Levin I, Krayzman V, Woicik JC, Karapetrova J, Proffen T, Tucker MG, et al. Structural changes underlying the diffuse dielectric response in AgNbO₃. *Phys Rev B.* 2009;79:104113.
158. Yashima M, Matsuyama S, Sano R, Itoh M, Tsuda K, Fu D. Structure of ferroelectric silver niobate AgNbO₃. *Chem Mater.* 2011;23:1643–5.
159. Khan HU, Alam K, Mateenullah M, Blaschke HBS. Synthesis and characterization of solid solution Ag(Nb_xTa_{1-x})O₃ (x= 0, 0.25, 0.5, 0.75, 1.0). *J Eur Ceram Soc.* 2015;35:2775–89.
160. Khan HU, Sterianou I, Miao S, Pokorny J, Reaney IM. The effect of Li-substitution on the M-phases of AgNbO₃. *J Appl Phys.* 2012;111:024107.
161. Yang P, Payne DA. Thermal stability of field-forced and field-assisted antiferroelectric-ferroelectric phase transformations in Pb(Zr, Sn, Ti)O₃. *J Appl Phys.* 1992;71:1361–7.
162. Pathak A, Prakash C, Chatterjee R. Shape memory effect in PZST system at exact morphotropic phase boundary. *Phys B Condens Matter.* 2009;404:3457–61.
163. Shebanov L, Kusnetsov M, Sternberg A. Electric field-induced antiferroelectric-to-ferroelectric phase transition in lead zirconate titanate stannate ceramics modified with lanthanum. *J Appl Phys.* 1994;76:4301–4.
164. Ishchuk V, Kuzenko D, Sobolev V. Piezoelectric and functional properties of materials with coexisting ferroelectric and antiferroelectric phases. *AIMS Mater Sci.* 2018;5:711.

165. Xu Z, Feng Y, Zheng S, Jin A, Wang F, Yao X. Phase transition and dielectric properties of La-doped Pb(Zr, Sn, Ti)O₃ antiferroelectric ceramics under hydrostatic pressure and temperature. *J Appl Phys.* 2002;92:2663–7.
166. Pan WY, Dam CQ, Zhang QM, Cross LE. Large displacement transducers based on electric field forced phase transitions in the tetragonal (Pb_{0.97}La_{0.02})(Ti, Zr, Sn)O₃ family of ceramics. *J Appl Phys.* 1989;66:6014–23.
167. Dai X, Viehland D. Effects of lanthanum modification on the antiferroelectric-ferroelectric stability of high zirconium-content lead zirconate titanate. *J Appl Phys.* 1994;76:3701–9.
168. Ishchuk VM, Sobolev VL. Coexisting ferroelectric and antiferroelectric phases in dipole ordered substances. Material properties and possible applications. arXiv preprint arXiv:1801.03397; 2018.
169. Mason WP. The elastic, piezoelectric, and dielectric constants of potassium dihydrogen phosphate and ammonium dihydrogen phosphate. *Phys Rev.* 1946;69:173.
170. Boiko AA, Golovnin VA. Thermal expansion of ADP and DADP in region of antiferroelectric phase transition. *Sov Phys Crystallogr.* 1970;15:153.
171. Fukami T, Akahoshi S, Hukuda K, Yagi T. Refinement of the crystal structure of NH₄H₂PO₄ above and below antiferroelectric phase transition temperature. *J Phys Soc Jpn.* 1987;56:2223–4.
172. Iida S, Terauchi H. Dipole-glass phase in random mixture of ferroelectric and antiferroelectric: Rb_{1-x}(NH₄)_xH₂PO₄. *J Phys Soc Jpn.* 1983;52:4044–7.
173. Ono Y, Hikita T, Ikeda T. Phase transitions in mixed crystal system K_{1-x}(NH₄)_xH₂PO₄. *J Phys Soc Jpn.* 1987;56:577–88.
174. Gridnev SA, Korotkov LN, Shuvalov LA, Fedosyuk RM. Influence of bias field on proton glass dynamics of K_{1-x}(NH₄)_xH₂PO₄. *Ferroelectrics.* 1994;157:189–94.
175. Pirc R, Tadić B, Blinc R. Random-field smearing of the proton-glass transition. *Phys Rev B.* 1987;36:8607.
176. Tan GL, Li W. Ferroelectricity and ferromagnetism of M-type lead hexaferrite. *J Am Ceram Soc.* 2015;98:1812–7.
177. Huang Y, Tan G. Antiferroelectric and magnetodielectric coupling response of La_{0.2}Sr_{0.7}Fe₁₂O₁₉ ceramics. arXiv preprint arXiv:1803.00731; 2018.
178. Muller J, Böske TS, Schröder U, Mueller S, Bräuhäus D, Böttger U, et al. Ferroelectricity in simple binary ZrO₂ and HfO₂. *Nano Lett.* 2012;12:4318–23.
179. Reyes-Lillo SE, Garrity KF, Rabe KM. Antiferroelectricity in thin-film ZrO₂ from first principles. *Phys Rev B.* 2014;90:140103.
180. Wakamatsu T, Kawamura G, Abe T, Nakahira Y, Kawaguchi S, Moriyoshi C, et al. Antiferroelectric to antiferroelectric-relaxor phase transition in calcium strontium sulfoaluminate. *Inorg Chem.* 2019;58:15410–6.
181. Yoshida S, Fujita K, Akamatsu H, Hernandez O, Gupta AS, Brown FG, et al. Ferroelectric Sr₃Zr₂O₇: competition between hybrid improper ferroelectric and antiferroelectric mechanisms. *Adv Funct Mater.* 2018;28:1801856.
182. Reimers JR, Tawfik SA, Ford MJ. van der Waals forces control ferroelectric–antiferroelectric ordering in CuInP₂S₆ and CuBiP₂Se₆ laminar materials. *Chem Sci.* 2018;9:7620–7.
183. Gave MA, Bilc D, Mahanti SD, Breshears JD, Kanatzidis MG. On the lamellar compounds CuBiP₂Se₆, AgBiP₂Se₆ and AgBiP₂S₆. Antiferroelectric phase transitions due to cooperative Cu⁺ and Bi³⁺ ion motion. *Inorg Chem.* 2005;44:5293–303.
184. Belianinov A, He Q, Dziaugys A, Maksymovych P, Eliseev E, Borisevich A, et al. CuInP₂S₆ room temperature layered ferroelectric. *Nano Lett.* 2015;15:3808–14.
185. Xu C, Chen Y, Cai X, Meingast A, Guo X, Wang F, et al. Two-dimensional antiferroelectricity in nanostripe-ordered In₂Se₃. *Phys Rev Lett.* 2020;125:047601.
186. Meyer RB, Liebert L, Strzeleski L, Keller P. Ferroelectric liquid crystals. *J Phys Lett.* 1975;36:69–71.
187. Clark NA, Lagerwall ST. Submicrosecond bistable electro-optic switching in liquid crystals. *Appl Phys Lett.* 1980;36:899–901.
188. Lagerwall ST. Ferroelectric and antiferroelectric liquid crystals. *Ferroelectrics.* 2004;301:15–45.
189. Chandani ADL, Gorecka E, Ouchi Y, Takezoe H, Fukuda A. Responsible for the tristable switching in MHPOBC. *Jpn J Appl Phys.* 1989;28:1265–8.
190. Dierking I. Chiral liquid crystals: structures, phases, effects. *Symmetry.* 2014;6:444–72.
191. Tagantsev AK, Cross LE, Fousek J. Domains in ferroic crystals and thin films. New York: Springer; 2010.
192. Müller U. Symmetry relationships between crystal structures: applications of crystallographic group theory in crystal chemistry. Oxford: Oxford University Press; 2013.
193. Salje EK. Phase transitions in ferroelectric and co-elastic crystals. Cambridge: Cambridge University Press; 1990.
194. Liu YY, Li JY. Energetic analysis of ferroelectric domain patterns by equivalent inclusion method. *J Mater Sci.* 2009;44:5214–24.
195. Zheludev IS. Domain structure of ferroelectrics and antiferroelectrics. Physics of crystalline dielectrics. Boston: Springer; 1971.
196. Jan F, Janovec V. The orientation of domain walls in twinned ferroelectric crystals. *J Appl Phys.* 1969;40:135–42.
197. Sapriel J. Domain-wall orientations in ferroelastics. *Phys Rev B.* 1975;12:5128.
198. He H, Tan X. Electric-field-induced transformation of incommensurate modulations in antiferroelectric Pb_{0.99}Nb_{0.02}[(Zr_{1-x}Sn_x)_{1-y}Ti_y]_{0.98}O₃. *Phys Rev B.* 2005;72:024102.
199. Choo WK, Park KH, Lee JY, Hoon L, Lee HJ, Ryu H. TEM domain structure and dielectric properties of antiferroelectric PbYb_{1/2}Nb_{1/2}O₃. *J Korean Phys Soc.* 1998;32:S715–S718.
200. Ma T, Fan Z, Zhou L, Tan X. Atomically resolved domain boundary structure in lead zirconate-based antiferroelectrics. *Appl Phys Lett.* 2019;115:122902.
201. Snykers M, Serneels R, Delavignette P, Gevers R, Van Landuyt J, Amelinckx S. Diffraction contrast between inversion domains and at inversion domain boundaries. *Phys Status Solidi A.* 1977;41:51–63.
202. Van Heurck C, Van Tendeloo G, Ghose S, Amelinckx S. Paraelectric-antiferroelectric phase transition in titanite, CaTiSiO₅. *Phys Chem Miner.* 1991;17:604–10.
203. Van Landuyt J, Gevers R, Amelinckx S. Fringe patterns at anti-phase boundaries with $\alpha = \pi$ observed in the electron microscope. *Phys Status Solidi B.* 1964;7:519–46.
204. Zhang X, Hashimoto T, Joy DC. Electron holographic study of ferroelectric domain walls. *Appl Phys Lett.* 1992;60:784–6.
205. McCartney MR, Smith DJ. Electron holography: phase imaging with nanometer resolution. *Annu Rev Mater Res.* 2007;37:729–67.
206. Cao W, Randall CA. Theory on the fringe patterns in the study of ferroelectric domain walls using electron holography. *Solid State Commun.* 1993;86:435–9.

207. Shibata N, Findley SD, Kohno Y, Sawada H, Kondo Y, Ikuhara Y. Differential phase-contrast microscopy at atomic resolution. *Nat. Phys.* 2012;8:611–5.
208. Szwarcman D, Lubk A, Linck M, Vogel K, Lereah Y, Lichte H, et al. Ferroelectric effects in individual BaTiO₃ nanocrystals investigated by electron holography. *Phys Rev B.* 2012;85:134112.
209. LeBeau JM, D'Alfonso AJ, Wright NJ, Allen LJ, Stemmer S. Determining ferroelectric polarity at the nanoscale. *Appl Phys Lett.* 2011;98:052904.
210. Fan Z, Ma T, Wei J, Yang T, Zhou L, Tan X. TEM investigation of the domain structure in PbHfO₃ and PbZrO₃ antiferroelectric perovskites. *J Mater Sci.* 2020;55:4953–61.
211. Wei XK, Tagantsev AK, Kvasov A, Roleder K, Jia CL, Setter N. Ferroelectric translational antiphase boundaries in nonpolar materials. *Nat Commun.* 2014;5:1–8.
212. Wei XK, Jia CL, Roleder K, Setter N. Polarity of translation boundaries in antiferroelectric PbZrO₃. *Mater Res Bull.* 2015;62:101–5.
213. Wei XK, Vaideeswaran K, Sandu CS, Jia CL, Setter N. Preferential creation of polar translational boundaries by interface engineering in antiferroelectric PbZrO₃ thin films. *Adv Mater Interfaces.* 2015;2:1500349.
214. Pan W, Zhang Q, Bhalla A, Cross LE. Field-forced antiferroelectric-to-ferroelectric switching in modified lead zirconate titanate ceramics. *J Am Ceram Soc.* 1989;72:571–8.
215. Viehland D, Forst D, Xu Z, Li JF. Incommensurately modulated polar structures in antiferroelectric Sn-modified lead zirconate titanate: the modulated structure and its influences on electrically induced polarizations and strains. *J Am Ceram Soc.* 1995;78:2101–12.
216. Viehland D, Forst D, Li JF. Compositional heterogeneity and the origins of the multicell cubic state in Sn-doped lead zirconate titanate ceramics. *J Appl Phys.* 1994;75:4137–43.
217. Viehland D, Dai XH, Li JF, Xu Z. Effects of quenched disorder on La-modified lead zirconate titanate: long-and short-range ordered structurally incommensurate phases, and glassy polar clusters. *J Appl Phys.* 1998;84:458–71.
218. MacLaren I, Villaurrutia R, Schaffer B, Houben L, Peláiz-Barranco A. Atomic-scale imaging and quantification of electrical polarisation in incommensurate antiferroelectric lanthanum-doped lead zirconate titanate. *Adv Funct Mater.* 2012;22:261–6.
219. Liu H, Zhou Z, Qiu Y, Gao B, Sun S, Lin K, et al. An intriguing intermediate state as a bridge between antiferroelectric and ferroelectric perovskites. *Mater Horiz.* 2020;7:1912–8.
220. Ma T, Fan Z, Xu B, Kim TH, Lu P, Ballaiche L, et al. Uncompensated polarization in incommensurate modulations of perovskite antiferroelectrics. *Phys Rev Lett.* 2019;123:217602.
221. Fu Z, Chen X, Li Z, Hu T, Zhang L, Lu P, et al. Unveiling the ferroelectric nature of PbZrO₃-based antiferroelectric materials. *Nat Commun.* 2020;11:1–8.
222. Gao P, Nelson CT, Jokisaari JR, Baek SH, Bark CW, Zhang Y, et al. Revealing the role of defects in ferroelectric switching with atomic resolution. *Nat Commun.* 2011;2:1–6.
223. Wei XK, Jia CL, Du HC, Roleder K, Mayer J, Dunin-Borkowski RE. An unconventional transient phase with cycloidal order of polarization in energy-storage antiferroelectric PbZrO₃. *Adv Mater.* 2020;32:1907208.
224. Liao Z, Xue F, Sun W, Song D, Zhang Q, Li JF, et al. Reversible phase transition induced large piezoelectric response in Sm-doped BiFeO₃ with a composition near the morphotropic phase boundary. *Phys Rev B.* 2017;95:214101.
225. Fan Z, Xue F, Tutuncu G, Chen LQ, Tan X. Interaction dynamics between ferroelectric and antiferroelectric domains in a PbZrO₃-based ceramic. *Phys Rev Appl.* 2019;11:064050.
226. Altgilber LL, Baird J, Freeman BL, Lynch CS, Shkuratov SI. Explosive pulsed-power. London: Imperial College Press; 2011.
227. Gao Z, Peng W, Chen B, Redfern SAT, Wang K, Chu B, et al. Giant power output in lead-free ferroelectrics by shock-induced phase transition. *Phys Rev Mater.* 2019;3:035401.
228. Altgilber LL. Explosive pulsed power: an enabling technology. *Acta Phys Pol A.* 2009;115:1040–3.
229. https://www.smdc.army.mil/Portals/38/Documents/Publications/Fact_Sheets/Archived_Fact_Sheets/FEG.pdf
230. Liu Z, Lu T, Xue F, Nie H, Withers R, Studer A, et al. Lead-free (Ag, K)NbO₃ materials for high-performance explosive energy conversion. *Sci. Adv.* 2020;6:eaba0367.
231. Kishi H, Mizuno Y, Chazono H. Base-metal electrode-multilayer ceramic capacitors: past, present and future perspectives. *Jpn J Appl Phys.* 2003;42(1):1.
232. Hong K, Lee TH, Suh JM, Yoon SH, Jang HW. Perspectives and challenges in multilayer ceramic capacitors for next generation electronics. *J Mater Chem C.* 2019;7:9782–802.
233. Love GR. Energy storage in ceramic dielectrics. *J Am Ceram Soc.* 1990;73:323–8.
234. Gachigi K. Electrical Energy storage in antiferroelectric-ferroelectric phase switching, chemically modified lead zirconate ceramics. PhD dissertation, Pennsylvania State University; 1997.
235. Wang H, Liu Y, Yang T, Zhang S. Ultrahigh energy-storage density in antiferroelectric ceramics with field-induced multiphase transitions. *Adv Funct Mater.* 2019;29:1807321.
236. Zhao L, Gao J, Liu Q, Zhang S, Li JF. Silver niobate lead-free antiferroelectric ceramics: enhancing energy storage density by B-site doping. *ACS Appl Mater Interfaces.* 2018;10:819–26.
237. Yang X, Zhuo F, Wang Z, Lv L, Liu Y, He C, et al. Enhanced energy storage density of lead lutetium niobate crystals by electric field-induced secondary phase transition via Na/La co-doping. *ACS Appl Mater Interfaces.* 2020;12:28239.
238. Xu Y, Guo Y, Liu Q, Yin Y, Bai J, Lin L, et al. Enhanced energy density in Mn-doped (1-x)AgNbO₃-xCaTiO₃ lead-free antiferroelectric ceramics. *J Alloys Compd.* 2020;821:153260.
239. Shi J, Chen X, Li X, Sun J, Sun C, Pang F, et al. Realizing ultrahigh recoverable energy density and superior charge–discharge performance in NaNbO₃-based lead-free ceramics via a local random field strategy. *J Mater Chem C.* 2020;8:3784–94.
240. Xu R, Zhu Q, Xu Z, Feng Y, Wei X. PLZST antiferroelectric ceramics with promising energy storage and discharge performance for high power applications. *J Am Ceram Soc.* 2020;103:1831–8.
241. Ye J, Wang G, Zhou M, Liu N, Chen X, Li S, et al. Excellent comprehensive energy storage properties of novel lead-free NaNbO₃-based ceramics for dielectric capacitor applications. *J Mater Chem C.* 2019;7:5639–45.
242. Chauhan A, Patel S, Vaish R, Bowen CR. Anti-ferroelectric ceramics for high energy density capacitors. *Materials.* 2015;8:8009–31.
243. Zhang H, Chen X, Cao F, Wang G, Dong X, Hu Z, et al. Charge–discharge properties of an antiferroelectric ceramics capacitor under different electric fields. *J Am Ceram Soc.* 2010;93:4015–7.
244. Chen X, Cao F, Zhang H, Yu G, Wang G, Dong X, et al. Dynamic hysteresis and scaling behavior of energy density in Pb_{0.99}Nb_{0.02}[(Zr_{0.60}Sn_{0.40})_{0.95}Ti_{0.05}]O₃ antiferroelectric bulk ceramics. *J Am Ceram Soc.* 2012;95:1163–6.

245. Kim YH, Kim JJ. Scaling behavior of an antiferroelectric hysteresis loop. *Phys Rev B*. 1997;55:R11933.
246. Valant M, Suvorov D, Hoffman C. Ag(Nb, Ta)O₃-based ceramics with suppressed temperature dependence of permittivity. *J Eur Ceram Soc*. 2001;21:2647–51.
247. Valant M, Axelsson AK, Alford N. Review of Ag(Nb, Ta)O₃ as a functional material. *J Eur Ceram Soc*. 2007;27:2549–60.
248. Zhao L, Liu Q, Gao J, Zhang S, Li JF. Lead-free antiferroelectric silver niobate tantalate with high energy storage performance. *Adv Mater*. 2017;29:1701824.
249. Luo N, Han K, Cabral MJ, Liao X, Zhang S, Liao C, et al. Constructing phase boundary in AgNbO₃ antiferroelectrics: pathway simultaneously achieving high energy density and efficiency. *Nat Commun*. 2020;11(1):1–10.
250. Lu Z, Bao W, Wang G, Sun SK, Li L, Li J, et al. Mechanism of enhanced energy storage in AgNbO₃-based lead-free antiferroelectrics. *Nano Energy*. 2020;79:105423.
251. Kobayashi K, Ryu M, Doshida Y, Mizuno Y, Randall CA. Novel high-temperature antiferroelectric-based dielectric NaNbO₃–NaTaO₃ solid solutions processed in low oxygen partial pressures. *J Am Ceram Soc*. 2013;96:531–7.
252. www.tdk-electronics.tdk.com/download/1195592/1753c455d19f9c7e635942c9cfba0318/ceralink-presentation.pdf
253. Machin JW, Brownhill J, Furness A. Design for a constant peak current defibrillator. *IEEE Trans Biomed Eng*. 1990;37:723–30.
254. Kroll MW. A minimal model of the monophasic defibrillation pulse. *Pacing Clin Electrophysiol*. 1993;16:769–77.
255. Schuder JC, Rahmoeller GA, Stoeckle H. Transthoracic ventricular defibrillation with triangular and trapezoidal waveforms. *Circ Res*. 1966;19:689–94.
256. Dougherty JP. Cardiac defibrillator with high energy storage antiferroelectric capacitor. U.S. Patent No. 5,545,184; 1996.
257. Dougherty JP, Gachigi KW, Shrout TR, Jang SJ, Randall CA, Pruna PM. Cardiac defibrillator with multi-phase ferroelectric/antiferroelectric capacitor. U.S. Patent No. 5,728,138; 1998.
258. Yamakawa K, Trolrier-McKinstry S, Dougherty JP. Reactive magnetron co-sputtered antiferroelectric lead zirconate thin films. *Appl Phys Lett*. 1995;67:2014–6.
259. Gaskey CJ, Udayakumar KR, Chen HD, Cross LE. Antiferroelectric to ferroelectric phase switching thin films in the lead zirconate stannate titanate solid solution system. In Proceedings of 9th IEEE international symposium on applications of ferroelectrics, IEEE; 1994.
260. Ahn CW, Amarsanaa G, Won SS, Chae SA, Lee DS, Kin IW. Antiferroelectric thin-film capacitors with high energy-storage densities, low energy losses, and fast discharge times. *ACS Appl Mater Interfaces*. 2015;7:26381–6.
261. Mirshekarloo MS, Yao K, Sriharan T. Large strain and high energy storage density in orthorhombic perovskite (Pb_{0.97}La_{0.02})(Zr_{1-x-y}Sn_xTi_y)O₃ antiferroelectric thin films. *Appl Phys Lett*. 2010;97:142902.
262. Hu Z, Ma B, Koritala RE, Balachandran U. Temperature-dependent energy storage properties of antiferroelectric Pb_{0.96}La_{0.04}Zr_{0.98}Ti_{0.02}O₃ thin films. *Appl Phys Lett*. 2014;104:263902.
263. Ma B, Kwon DK, Narayanan M, Balachandran U. Dielectric properties and energy storage capability of antiferroelectric Pb_{0.92}La_{0.08}Zr_{0.95}Ti_{0.05}O₃ film-on-foil capacitors. *J Mater Res*. 2009;24:2993–6.
264. Morris DH, Avci UE, Young IA. Anti-ferroelectric capacitor memory cell. U.S. Patent Application No. 15/994,227; 2019.
265. Vopson MM, Tan X. Four-state anti-ferroelectric random access memory. *IEEE Electron Device Lett*. 2016;37:1551–4.
266. Uchino K, Cross LE, Newnham RE. Electrostrictive effects in antiferroelectric perovskites. *J Appl Phys*. 1991;52:1455–9.
267. Uchino K, Oh KY. Piezoelectric anisotropy and polarization sublattice coupling in perovskite crystals. *J Am Ceram Soc*. 1991;74:1131–4.
268. Uchino K. Antiferroelectric shape memory ceramics. *Actuators*. 2016;5:11.
269. Lu T, Studer AJ, Noren L, Hu W, Yu D, McBride B, et al. Electric-field-induced AFE-FE transitions and associated strain/preferred orientation in antiferroelectric PLZST. *Sci Rep*. 2016;6:23659.
270. Lanagan MT, Kim JH, Jang SJ, Newnham RE. Microwave dielectric properties of antiferroelectric lead zirconate. *J Am Ceram Soc*. 1988;71:311–6.
271. Steele BCH. *Electronic ceramics*. New York: Elsevier Science; 1991.
272. Porokhonskyy V, Bovtun V, Kamba S, Buixaderas E, Petzelt J, Kania A, et al. Microwave dielectric properties of the Ag_{1-x}Li_xNbO₃ (x=0–0.06) ceramics. *Ferroelectrics*. 2000;238:131–8.
273. Valant M, Suvorov D. New high-permittivity AgNb_{1-x}TaxO₃ microwave ceramics: part II, dielectric characteristics. *J Am Ceram Soc*. 1999;82:88–93.
274. Harada J, Yoneyama N, Yokokura S, Takahashi Y, Miura A, Kitamura N, et al. Ferroelectricity and piezoelectricity in free-standing polycrystalline films of plastic crystals. *J Am Chem Soc*. 2018;140:346–54.
275. Wu Z, Liu X, Ji C, Li L, Wang S, Peng Y, et al. Discovery of an above-room-temperature antiferroelectric in two-dimensional hybrid perovskite. *J Am Chem Soc*. 2019;141:3812–6.
276. Šimėnas M, Balčiūnas S, Mączka M, Banys J, Tornau EE. Exploring the antipolar nature of methylammonium lead halides: a Monte Carlo and pyrocurrent study. *J Phys Chem Lett*. 2017;8:4906–11.
277. Jain P, Dalal NS, Toby BH, Kroto HW, Cheetham AK. Order-disorder antiferroelectric phase transition in a hybrid inorganic-organic framework with the perovskite architecture. *J Am Chem Soc*. 2008;130:10450–1.
278. Li P, Liao W, Tang Y, Ye H, Zhang Y, Xiong R. Unprecedented ferroelectric-antiferroelectric-paraelectric phase transitions discovered in an organic-inorganic hybrid perovskite. *J Am Chem Soc*. 2017;139:8752–7.
279. Shi J, Han D, Li Z, Yang L, Li S, Zhong Z, et al. Electrocaloric cooling materials and devices for zero-global-warming-potential, high-efficiency refrigeration. *Joule*. 2019;3:1200–25.

How to cite this article: Randall CA, Fan Z, Reaney I, Chen L-Q, Trolrier-McKinstry S. Antiferroelectrics: History, fundamentals, crystal chemistry, crystal structures, size effects, and applications. *J Am Ceram Soc*. 2021;104:3775–3810. <https://doi.org/10.1111/jace.17834>